SCIENCE MUSEUM: AN ESSENTIAL COMPONENT OF THE SCIENCE LEARNING ECOSYSTEM

N. Farbiash

Carasso Science Park, HaAtsmaut St. 79, Beersheba, Israel
E-mail: netzach.farbiash@rashi.org.il

Abstract

Recent studies highlight the complex and synergistic nature of the science learning ecosystem. Public science education is supported not by a single major resource (e.g., formal schooling), but rather by a vast array of resources that includes schools and free-choice learning experiences, both in childhood and adulthood. Moreover, new studies show that although it has long been argued that schools play the most important role in reducing social inequalities, the most significant contributors to adult science values and predispositions, are non-school experiences dealing with important policy issues.

During the last decades, science museums, as well as science centers and other informal learning institutions, play an increasing role in promoting science for students, teachers, and families at a community wide level. As science museums have an important social impact, in one form or another, three main goals can be found in most of the world's science museums:

1. closing the gap of STEM (Science, Technology, Engineering, and Math) education in the community,
2. expanding of STEM learning, invention, experimentation and innovation by providing attractive activities for youth (such as makerspace), and
3. highlighting the importance of STEM education as a critical need for 21st century careers and living.

Having that in mind, the founders of the Carasso Science Park (Beer-Sheva, Israel), organized 20 years ago an international workshop to establish a science museum in the southern region of Israel. 15 years later (July 2013), the museum was opened to the public, providing non-traditional learning environments and informal learning resources for 700,000(!) on site visitors and outreach programs participants (updated to summer 2018).

Since we understand science museums are an essential component of the science learning ecosystem, we share our experience in establishing a new science museum, in creating an outreach programs (with mobile labs), and in building a sustainable operation model, combining the state (ministry of education and others) municipalities, and the community.

1. Introduction

It is well agreed that STEM (Science, Technology, Engineering, and Mathematics) education is necessary for innovation and economic growth of any society. On the other hand, although STEM education demonstrated the capacity to build bridges across geographical, economic, political, religious and cultural barriers, it also might be a booster to increase the gap between different parts of the society. Therefore, it is necessary to enable anyone who is capable, regardless of his background, to integrate into the STEM fields, whether in academia or industry. This can be only achieved by creating equal education opportunities for all, and to train professionals for the growing needs of the modern society [1-5].

It is common to distinguish between formal education (kindergarten, school, university, etc.) and non-formal education (family, community, afternoon activities, internet, science museums, etc.) that are both parts of the science learning system. However, although science education is generally viewed in terms of classrooms and curricula, there is an increasing interest in the learning that takes place before, after, and outside of our brief exposure to science in the classroom. Attitudes and experiences that are established at an early age have a substantial later impact on our interest, skills, and success in formal science classes [6]. Moreover, new studies show that although it has long been argued that schools play the most important role in reducing social inequalities, the most significant contributors to adult science values and predispositions, are non-school experiences dealing with important policy issues [1, 2, 4].

Few years ago, Michael Bloomberg gave $50 Million to Museum of Science, Boston, highlighting the influence of informal education. Bloomberg, the three-term mayor of New York and billionaire philanthropist, has said that throughout his life he has been most influenced by his parents. The second influence mentioned, was the Museum of Science, Boston. In his 1997 memoir, “Bloomberg by Bloomberg,”

he described Saturday-morning lectures at the museum: "I sat spellbound as an instructor brought snakes, porcupines and owls for us to hold; demonstrated the basic laws of physics with hands-on experiments; and quizzed us on every museum exhibit. All the kids — including me — tried to show off by having every answer" [7].

According to the International Council of Museums (ICOM), A museum is a non-profit, permanent institution in the service of society and its development, open to the public, which acquires, conserves, researches, communicates and exhibits the tangible and intangible heritage of humanity and its environment for the purposes of education, study and enjoyment [8]. In the case of Science Museums (and centers), the Association of Science-Technology Centers (ASTC) chose to emphasis three main roles: connect people with science, provide firsthand experience, and encourage curiosity [9].

A 2013 study conducted by San Francisco's Exploratorium found that learning to ask good questions such as "What if?" or "How can?" often leads to more questions, more experiments, and better interpretations. Exploratorium's "Mind" exhibition encourages guests to test their thought processes and emotions. For example, visitors drink from a water fountain resembling a real, but unused toilet, and explore their reactions [10].

Figure 1: The author explore his reaction when drinking from a water fountain resembling a real, but unused toilet, presented at the "Brain" exhibition, Center for Life, Newcastle upon Tyne, UK.

During the last decades, science museums, as well as science centers and other informal learning institutions, play an increasing role in promoting science for students, teachers, and families at a community wide level [1]. Three main goals can be found in most of the world's science museums: closing the gap of STEM (Science, Technology, Engineering, and Math) education in the community, expanding of STEM learning, invention, experimentation and innovation by providing attractive activities for youth (such as makerspace), and highlighting the importance of STEM education as a critical need for 21st century careers and living.

It is important to point out that science museums are not aiming to replace formal STEM studies. Science museum play an important role emphasizing that STEM is for everyone. They do it by giving science a presence in the community and offer people of all ages and backgrounds the opportunity to ask questions, discuss, and explore.

Although schools are probably the first example for formal education system, in many cases they rely on science centers for significant STEM programs, hands-on curriculum, science shows and demonstrations,

and even training for teachers. Science museums encourage curiosity. Exhibits that are beautiful or surprising, or even funny, can encourage visitors to approach new phenomena and ideas. In the words of Frank Oppenheimer, founder of San Francisco's Exploratorium, "No one ever failed a museum". For some, the interests awakened by science museum experiences have turned into a passion for science, and the beginning of a lifetime devoted to teaching or research [9].

School excursions to museums can form an integral and innovative component of school practical learning in science. However, since science museums are informal learning environments, teachers have limited control over the specific ideas or experiences with which the students are engaged. Therefore, to make successful use of museums as learning resources, appropriate teaching and learning approaches and strategies, a shift from task orientation to student centered learning orientation, is needed. By allowing student learning to happen in a natural way, that is, by allowing personal interest and curiosity to drive the students' learning, not only will students be gaining more from their excursion, they will be practicing scientific investigative processes. Incorporation of the excursion into school-based investigations renders the purposes for the visit clearly apparent, and gives students a goal to achieve back at school using the information gathered at the museum [8].

The relationship between schools and science museums are well known, supported by many studies that have pointed out its benefits. On the other hand, other issues, from the selected exhibitions that are presented at the museum, the curriculum studied at school, and most of all, the different teams that are responsible to guide and teach at each institute, are still open. In order to get over some of these issues, a new model of establishing science museum was implement when the Carasso Science Park was planned.

2. Carasso Science Park – A Science Learning Ecosystem Test Case

Carasso Science Park, the newest science museum in Israel, featuring an interactive science museum, scientific garden with hands-on games and activities for all ages, laboratories, and a 3D printing FabLab. The museum offers interactive exhibitions in various fields of Science including Genetics, Communication, Microelectronics, Nuclear Energy and more. In all, hundreds of technological and scientific exhibits. Spread over 4.25 acres, visitors can enjoy the massive outdoor sculptures and playground, interactive fountain and gallery exhibits. Recently, a new international exhibition, "The Last Mammoth", opened to the public. The exhibition, introduces the period of the "Pleistocene" Ice age accrue 2.5 million years ago, exploited all over the park, introducing animal models, cave paintings, special "ice room" and a main exhibit, a real body of a small woolly mammoth found in Siberia. In the first five years of operation, about 700,000(!) visitors have visited the museum, while in the all city there are 220,000 residents.

Obviously, a modern state of the art science museum is a great place to spend some time in, and it might be the reason for large number of visitors, and in particular, students. However, besides its size, its interactive exhibits, and its location, the most important message the Carasso Science Park brings, is the joined forces that create a real sustainable STEM eco-system. The founders of the museum: Rashi Foundation, an independent private foundation dedicated to assisting the underprivileged in Israel's geographic and social periphery, particularly children, youth and young adults, Beer-Sheva municipality, Ministry of Education, and the Carasso family, together with other partners from the academy, created new conception of how science museum should be established.

Carasso Science Park is part of a unique, multi-faceted educational platform: Gustave Leven Campus, a comprehensive educational infrastructure. The campus includes 'Beit Yatziv': an educational institution featuring the Open University, hotel accommodation and dining services and a number of other educational programs. The educational team includes teachers (as a part of the collaboration with the Ministry of Education), as well as students for science and technology from Beer-Sheva academic institutes (Ben-Gurion University, SCE, etc.). Kindergarten kids, elementary and high school students arriving to the park, enjoying educational programs fit to their curriculum and level of interest. For each group, a special tour is made which includes science exhibitions, laboratory experiments, demonstrations, 3D print laboratory ("FabLab") and as has been sad – practical experience.

Most of the question the Carasso Science Park is dealing with are most likely similar to those that are been discussed in other science museums. On the other hand, since representative from the academy, ministry of education, Beer-Sheva municipality, and other relevant partners, sit together in the museum's committees, it is probably easier to have answers, and more important, it enable the museum to start with complicated projects, that requires cooperation between different institutes, with the minimal time and efforts.

The following three examples of activities that are operated by the Carasso Science Park deals with essential question: Should university be involved with kindergarten/school activities? Who trains the next

generation of educators? Do formal education should use informal education to increase number of science students?

2.1. Science Learning Ecosystem – Example 1 – Academic Course

Sami Shamoon College of Engineering (SCE), located in the city center of Beer-Sheva, has operated for several years a course for designing and manufacturing scientific toys. Students have been asked to think about the needs, to design a scientific toy, and to manufacture it. In the end of the semester, student had to present their works in front of faculty members, and sometimes also in front of external referees. The event was held at the college campus, close to the public. Few years ago I was invited to participate the event as an external referee. My first thought, beside the impression of the high level of work that was presented, was that by keeping the event inside the college campus, we loss priceless opportunity to engage science and technology with the public.

Having that in mind, the faculty members from SCE and the educational team from the Carasso Science Park, started to rethink about the course and to shape it in a way it would have greater impact, both on the student, their families, and the community. The new course was implemented without any delays, and it is still running since then.

In its revised version, students from the SCE start their semester at the science museum, and are asked to create scientific toys. This time, not just because it is a course task, but because it is a real need of the science museum. Also, the students' visit at the museum, include guided tour to understand issues of maintenance and the delivery of scientific message though games. After weeks of working in the college, museum experts visit the students at the college workshops, providing ideas and suggesting improvements. Final submission of the students' work is taking place at the Museum. Then, after presenting their products to their colleague students and professors, the scientific toys are presented to the public within the frame of an open event: Scientific Toys Fair.

This fair is a unique opportunity for students to present their outcomes to their families, friends, children, and other people from the community which can engage directly, without any boundaries with the students and their products. Students get the most authentic reactions to the toys they created, letting them know, whether they achieved what they had in mind.

2.2. Science Learning Ecosystem – Example 2 – Teachers Training

Despite evidence of quality teaching in Science, Technology, Engineering and Mathematics (STEM) subject domains and insistence on the part of many national governments on the economic value of STEM, education, recruitment and retention into STEM subject fields and occupations is said to be continually blighted by a ‘leaky pipeline’ [12]. STEM engagement activities are often seen as synonymous with informal and/or free choice educational spaces like museums and science centers [13, 14, 15] and contexts that are manifestly organized around an ‘edutainment’ logic like science shows [16] and science festivals [17]. Teachers on the other hand, are usually left to teach STEM, using a class and a white board. The contrast is even larger since future educators learn most of their studies in traditional classrooms. How can one expect educator that was trained in a traditional setting of classroom to enable his student study in a more attractive methods? The last does not mean in any form that the level should decrease. Vice versa, when students find STEM studies relevant for them, is it much easier to get into much higher level of thinking.

Together with Kaye Academic College of Education, Beer-Sheva, a new course for future educators was developed at the Carasso Science Park. During the course, that is taking place at the museum's FabLab, future educators are asked to implement advanced science education technologies, to create classroom activities. We hope that working in the new environment would enable future educators to implement more easily new technologies in their classrooms.

2.3. Science Learning Ecosystem – Example 3 – Youth Movement

In the Gustave Leven Campus, a unique teenager's project is operated. "Scientific Leadership", a youth movement program that combines science study with promoting social leadership by providing a firm basis for many young people to study Science, Physics and Astronomy. After a training process, selected students operate community activities on a weekly basis, emphasizes experiential learning and scientific experimentation. Graduates of this program receive a grant for their academic studies as a recompense for educating the next generation of the program.

The Scientific Leadership program combines all ages and spread over many communities. Hundreds of teenagers provides activates to thousands kindergarten, schools, junior high, high schools, parents, and the

community. Since the program is taking place at communities' facilities, it is relatively an unexpansive program, with a very strong impact.

3. Conclusions

Learning science is a rich, complex, ongoing process that built over a lifetime. Opportunities to learn science occur throughout the day and year, in a wide variety of settings, and through a range of experiences. Science museums are a lot more than collection of artifacts, they allow you to meet other people, discuss thoughts and opinions, and become part of the community.

Does "Advanced Technologies in Science Education" necessarily means focusing on technology? Can we see it as a conception? Maybe 'Advanced Technologies' is our set of mind? If you do not have a science museum or science center - get one! Science museum is an essential component of the science learning ecosystem.

Acknowledgements

The author wish to express his appreciation to the Nuclear Energy Commission, Government of Mongolia, for the invitation to participate at conference.

I would like to express my deepest appreciation to Prof. Suren Davaa for the warm hospitality and for his partnership.

Also, I would like to thank the IAEA TC Project. Without their support this scientific mission could not be held.

References

[1] J.H. Falk, S. Pattison S, Meier et al., The contribution of science-rich resources to public science interest, *J. Res. Sci. Teach.* 55: 422–445, 2018.
[2] M. Ballard, L. Herszenhorn, K. Levedahl et al., *Science centers and afterschool programs: Working together for all kids, dimensions*, Washington, DC: Association of Science and Technology Centers, 2016.
[3] K. Drotner, L.V. Knudsen, C.H. Mortensen, Young people's own museum views, *MMC* 32: 456-472, 2017.
[4] C.A. Price, F.R. Kares, *Researching Long-Term Impacts of an Out-Of-School Time Program, Dimensions*, Washington, DC: Association of Science and Technology Centers, 2016
[5] G. Ulvay, A.E. Ozkul, Museum education's contribution to multicultural education, *IJEP* 11: 639-652, 2017.
[6] G. W. Tressel, The role of museums in science education, *Sci. Educ.* 64: 257-260, 1980
[7] J. Barone, *Michael bloomberg gives $50 million to museum of science*, Boston, New-York Times, Oct. 19, 2016.
[8] ICOM website (https://icom.museum/en/)
[9] ASTC website (https://www.astc.org/)
[10] J. Ma, Annual Meeting of the American Educational Research Association, San Francisco, 2013
[11] J. Griffin, Learning science through practical experiences in museums, *IJSE* 20: 655-663, 1998
[12] R. Watermeyer, Public dialogue with science and development for teachers of STEM: linking public dialogue with pedagogic praxis, *JET* 44: 90-106, 2018.
[13] J.H. Falk, L.D. *Dierking, Learning From Museums: Visitor Experiences and the Making of Meaning*, Walnut Creek, CA: AltaMira Press, 2000.
[14] S. Stocklmayer, L. Rennie, J.K. Gilbert, The roles of the formal and informal sectors in the provision of effective science education, *Stud. Sci. Educ.* 46: 1-44, 2010.
[15] S. Schwan, A. Grajal, D. Lewalter, Understanding and engagement in places of science experience: Science museums, science centers, zoos, and aquariums, *Educ. Psychol.* 49: 70–85, 2014.
[16] R. Watermeyer, The presentation of science in everyday life: The science show, *CSSE* 8: 737–751, 2013.
[17] E. Jensen, N. Buckley, Why people attend science festivals: interests, motivations and self-reported benefits of public engagement with research, *Public Underst. Sci.* 23: 557–573, 2014.

SIMULATION EXPERIMENT AND QUANTUM SPECTRA OF HYDROGEN ATOM

P. Enkhtsetseg[1]*, O. Lkhagva [2], T. Ulambayar[3], N. Enkhtur[4]

[1]*School of engineering and Technology, Mongolian University of Life Science, Ulaanbaatar, Mongolia,*
[2]*School of Arts and Sciences, National University of Mongolia, Ulaanbaatar, Mongolia,*
[3]*School of Mathematics and Natural Science, Mongolian State University of Education, Ulaanbaatar, Mongolia,*
[4]*Department of Natural Sciences, Khovd University, Khovd, Mongolia*
**E-mail: enkhtsetseg@muls.edu.mn*

Abstract

The "geometry" of hydrogen atom was used to create a simulation laboratory that is to be conducted numerical experiments by students themselves with following formulation of semi quantum and spectral laws of the atom through debate around on data. The geometry was invented on the base utilizing the spectral data and Bohr semi quantum theory. It is shown ways how to be calculated simulation experiment data through applying universalities of fundamental laws of classical physics.

1. Introduction

A. Einstein in his theory of general relativity has shown that universe represents as geometry instead of storehouse in Newton physics. Now the idea is spreading extensively into various scientific fields for example in the matter structure, cell biology. The geometry is invented via mathematical modeling with employing precious experiment data of physical objects definite energy-impulse regularity and their space structure.

In sense numerical experiment exploiting geometry is accepted, at present, as real preparatory to physical experiments [1].

In previous experiments, scientists would prefer to have used digital geometry models for objects. Numerical experiments based on interaction of particles and radiation with object-geometry widely used in nuclear physics and cell biology, in particularly, geometry of DNA, neuron structure. Numerical experiments utilizing the object geometry become powerful medium for demonstrating all physical processes occurred in atomic and molecular worlds [2].

In this work, we determine how to apply universality of Newton laws for calculation physical quantities numerical experiments having geometry of H atom. The evolution of process will be fully demonstrated on computer screen and the experiment data will be displayed.

1.1. Universality of laws and scales in physics

Classical law works for different field is found to be possessing universality, the law remains unchanged under a scale transformation. But in modern physics, was appeared different scaling parameter for various branches which is assembled into more wide-ranging formulation. Particularly, it is converted into gravitational metric, representing the unification of newton gravity theory and general relativity. Light velocity in Maxwell equation is turned into more general meaning characterizing invariant of electrodynamics in Lorenz transformation. Most specific one is Planck's constant, displaying new world-quantum realm in which action function has values comparable. Then the classic mechanics became transformed into quantum mechanics. In the atomic scale, it have been reveal by measurement, that angular momentum of electron and energy of electron have quantum quantity. Peculiarity of quantum physics is that the values quantities have discrete values.

1.2. The atomic geometry

The geometry is real model of physical objects combining their space and energy-momentum structures with mathematical designing. So atom geometry contains experimental data of space structure and energy spectra. For atom the geometry involves discrete space and momentum structures and its experimental energy spectra. Thus interaction of light with H atom allows calculating ionization energy and atomic excitation. In accordance to Bohr quantum theory, atomic structure corresponds to discrete circle orbits. Performing simulation experiment students have got data, from which under teacher guide doing research debate they will be able to formulate Bohr theory fully with formulation quantum structure of atom.

2. Numerical experiment

Simulation: Let light beam falls on a hydrogen atom in its initial ground state. The light would be absorbed differently depending colors and frequencies. Simulation process results are collected with Camtasia that set of data of image and motion of physics elements information that displayed on screen. In table are shown set of numerical measurement results that include energy, frequency, wavelength and radius of an electron and lifetimes of state at different orbits [3].

Table 1: Data of experiment.

	m	n	$\lambda(nm)$	$\nu[10^{-15}Hz]$	$E[eV]$	$r[A^0]$	$v\,[10^6 m/s]$	$\tau\,[10^{-8}\,s]$
1	1	2	121.5	2.469	-3.4	2.12	1.1	0.2128
2	1	3	102.5	2.927	-1.511	4.77	0.733	0.1793
3	1	4	97.24	3.085	-0.850	8.48	0.550	0.7825
4	1	5	94.93	3.160	-0.544	13.25	0.440	0.2424

Students should do scientific analyses and conduct discussion having these data.

Analyzing-1: At first, it should be shown that energy spectra consists of discrete spectrum values of energy. Let's compute ratios of absolute values of ground state energy to excited state energies: $\frac{E_1}{E_2} = 4 = 2^2 \ldots \frac{E_1}{E_5} = 25 = 5^2$ and $\frac{E_1}{E_n} = n^2$ or $\frac{E_1}{n^2} = E_n$. The results tell us that ratios are square of integer numbers. These simple estimations lead to thought that electron in atom might be rested in states with discrete values of energy.

Analyzing-2: Discrete energy levels allow us to determine the frequency of emitted and absorbed light. To the difference of energy levels correspond definite differences of frequencies $\nu(Hz)$ of emitted light:

Table 2: Corresponding energy and frequency.

		$\Delta E[eV]$	$\nu[Hz]$
1	ΔE_{21}	10.2	$2.469Ч10^{15}$
2	ΔE_{31}	12.089	$2.927Ч10^{15}$
3	ΔE_{41}	12.75	$3.085Ч10^{15}$
4	ΔE_{51}	13.075	$3.106Ч10^{15}$

So there are following correspondence:

$$\Delta E_{21} < \Delta E_{31} < \Delta E_{41} < \Delta E_{51}, \quad \nu_{21} < \nu_{31} < \nu_{41} < \nu_{51}$$

The gap between the energy levels depends on its frequency $\Delta E \sim \nu$. Let's calculate coefficient of proportionality: $\Delta E = H \cdot \nu_{n1}$

Calculation: H Plank's constant is

$$\Delta E_{n1} = H \cdot \nu_{n1} \tag{1}$$
$$H = \frac{\Delta E_{n1}}{\nu_{n1}} \quad H = \frac{\Delta E_{n2}}{\nu_{n2}} = 6.62 \cdot 10^{-34}\, J \cdot s.$$

Analyzing-3: Let's estimate radius of circles which electron revolves around. Ratio of radius of excited state to radius of ground state one:

$$\frac{r_2}{r_1} = 4 = 2^2 \cdots \frac{r_5}{r_1} = 25 = 5^2$$

The estimations demonstrate:

$$\frac{r_n}{r_1} = n^2, \quad r_1 \cdot n^2 = r_n \tag{2}$$

Circle radiuses appeared again greater that the ground state one square of integer numbers.

Analyzing-4: Let perform simple calculation to reveal regularity velocities. The estimations show that

$$\frac{v_1}{v_2} = \frac{1}{2},\ \ldots \frac{v_1}{v} = \frac{1}{5} \quad \text{or} \quad \frac{v_1}{v_n} = n \tag{3}$$

Therefore the velocity of n is $\frac{v_1}{n} = v_n$. It manifests that in excited states velocities decreases in comparison to slow dawn integer number time.

Analyzing-5: In gravitational field derivative of the Lagrange function correspond to angular momentum which is stayed constant value in time:

$$\vec{L} = \frac{\partial L}{\partial \varphi} = m\vec{r}\vec{v} = mr^2\dot{\varphi} = mrv = const \tag{4}$$

Here $\vec{v} \perp \vec{r}$ and $v = r\dot{\varphi}$. Here it should be noted this conservation law demonstrates the geometry characterizing geometry according to universality classical laws. According to second Kepler law, angular momentum conservation law exhibits that planet radius of electron draws the same areas at the same time. Figure 1 shows that areas of curved triangles $s = v \cdot \Delta t$ drawing by radius of orbit are constant at the time Δt.

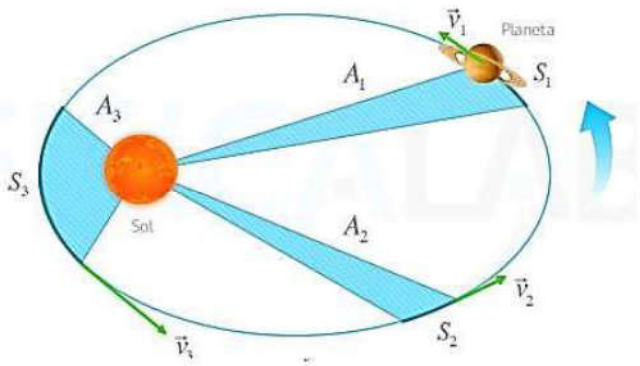

Figure 1: Kepler's law [5].

Anywhere circle is the same:

$$S = \frac{1}{2}rv \cdot \Delta t \tag{5}$$

The angular momentum $L = mrv = const$ has unit of measurement $kg \cdot \frac{m}{s} \cdot m = N \cdot m \cdot s = J \cdot s$ with unit that is the same as classical action in classical mechanics. N. Bohr has decided to make the angular momentum discrete as $L = mrv = Hn$.

$$L_n = H \cdot n \tag{6}$$

Taking discrete values of radius and velocity in various states let us calculate the H coefficient H. The estimation gives

$$H = 1.05 \cdot 10^{-34} J \cdot s = \hbar$$

This is famous Plank constant that was found at beginning of quantum physics.

Theoretical estimates.

N. Bohr estimates quantitative energy, velocity, and radius of the specimens defined by hydrogen atomic experiments [4].

$$\frac{mv_n^2}{r_n} = \frac{ke^2}{r_n^2}$$
$$mr_n v_n = nH \tag{7}$$

Here $n = 1,2,3, \ldots$

Solving these two equations one may obtain: Defines H:

$$mv_n^2 r_n = ke^2$$
$$nH = k \cdot \frac{e^2}{v}$$
$$H = k \cdot \frac{e^2}{nv} \quad \text{for } n = 1$$
$$H = 1.05 \cdot 10^{-34}\, J * s = \hbar$$
$$r_n = \frac{n\hbar^2}{km_e e^2}, \; n = 1 \quad r_1 = 0.53 \cdot 10^{-10}\, m.$$

The quantum theory of atom was developed.

3. Conclusions

We have simulated virtual laboratory for elementary physics. In this paper, only geometry of hydrogen atom has been used. Universality of classical mechanics allows performing calculation of quantities at different values of variables. These numerical data provides full conditions to conduct research analysis with following discussion discovered the semi quantum regularities. The virtual Laboratory represent new approach for teaching semi quantum physics based on modern numerical experiments.

References

[1] O. Lkhagva, P. Enkhtsetseg, T. Ulambayar et al., *3D virtual laboratory of physics*, Ulaanbaatar, Mongolia, 2017 (CD).

[2] L. Bayarchimeg, M. Batmunkh, O.V. Belov et al., Simulation of radiation damage to neural cells with Geant4-DNA, *Europ Phys. J.-WoC* 173: 05005, 2018.

[3] O. Lkhagva, T. Ulambayar, P. Enkhtsetseg, Virtual laboratory for physics teaching, *Intern. Proc. Econom. Develop. Res.* 37: 319-323, 2012.

[4] B.J. Smith, *Quantum ideas lecture course*, Chapter-3, Clarendon Laboratory, Physics Department, University of Oxford, England, 2016.

[5] Fisicalab home page: *https://www.fisicalab.com*

THE UNIVERSALITY OF THE CLASSICAL LAWS AND DESIGNING THE SIMULATION LABORATORY OF PHYSICS

P. Enkhtsetseg[1]*, O. Lkhagva[2], T. Ulambayar[3], N. Enkhtur[4]

[1]School of engineering and Technology, Mongolian University of Life Science, Ulaanbaatar, Mongolia,
[2]School of Arts and Sciences, National University of Mongolia, Ulaanbaatar, Mongolia,
[3]School of Mathematics and Natural Science, Mongolian State University of Education, Ulaanbaatar, Mongolia,
[4]Department of Natural Sciences, Khovd University, Khovd, Mongolia
*E-mail: enkhtsetseg@muls.edu.mn

Abstract

Innovative thinking is understood as a driving force for changing the universe. Instead of developing the creative potential of students, our education system implements the method of filling their memory with dry and tedious information. Using the universality principle of the fundamental laws of classical physics, in combination with the mathematical modeling we succeeded to create a virtual laboratory for elementary physics.

1. Introduction

1.1. Research, training and geometry of physics object

Currently, training is integrated with scientific logic at all levels from primary to university education. Thus, when learning, any information must be given in order to develop the students' imagination.

Humanity is liberating itself from the falsifiable understanding to consider the things like restricting itself to only visible light region, relying on quantum physic which is claiming to explain virtually everything about the universe. This idea is being used in natural science, social science and other field of technology beyond physics. This is developing basic issue to improve training method. It formulated the fundamental laws of classical physics from basic experiment data. In the general theory of relativity, Einstein discovered that universe is a "geometrical" structure, is not in motion of a star and planet in the Newton's mission.

Today, scientists have learned how to create the real geometry of any object based on experimental data on its structure with a combination of mathematical modeling and the quantum laws of its atoms and molecules.

Consequently, a numerical experiment acquires equal significance with a technical experiment and, moreover, as a rule, it is carried out before the true experiment. Such geometric structures of molecules, atoms, cells, DNA and neurons of the brain are used to effective study the quantum laws of their interaction with nuclear particles of various energies. Thus, priority branch of science radiation biology is being formed. For example, there are about 100 laboratories around the world that develop numerical experiment to research biology, DNA, neuron geometry and interactions of nuclear radiation. Numerical experiment use Geant4-DNA program. In this work, we have invented geometries describing their elementary physics' processes. The geometries were used to create a virtual three-dimensional (3D) laboratory for elementary physics. It should be noted that the universal principle and the invariance of the fundamental laws of classical physics played a decisive role in this development. The basic approach of building a 3D laboratory is essentially different from the existing virtual ones in the world. Their models usually based on drawing graphs using the formula of physics. In this paper, dependencies of physical quantities are derived from fundamental laws using real geometries. Consequently, laboratory works are to be found significance, equal to the corresponding well known classical experiments. We created about 70 practical works in which the geometry of physical objects was used.

1.2. Universality principle of fundamental laws in classical physics

Classical mechanics studies the laws of objects' motion in a force field and their interaction between themselves. It is well known that the equation of motion is derived by the principle of minimal interaction.

Kinetic energy convert to potential energy by barrier reaction of $\Phi(x,t)$ energyin F force field. When difference $L(x,\dot{x},t) = T(\dot{x},t) - \Phi(x,t)$ is minimum, the motion carry out through this trajectory. It is natural principle to save energy. This is called as Lagrangian function.

It is formulated $S(x,\dot{x}) = \int dtL(x,\dot{x},t)$ to issue motion equation.

When $\delta S(x,\dot{x}) = 0$ is variation minimum value of $S(x,\dot{x})$ function, if we use that form of Lagrangian function is: $L(x,\dot{x},t) = \frac{m}{2}\dot{x}^2\Phi(x)$.

$$m\frac{d^2x}{dt^2} = -\frac{\partial\Phi(x)}{\partial x} \tag{1}$$

Equation (1) is Newton's equation of motion. Where m is mass of body.
Newton's dynamical equation is invariant to the relative principle of Galileo. The time moment is the same everywhere. In a set of frame moving at constant velocity with respect to each other (inertial) system Newtonian equation (1) is found universally valid. This means that the mechanical motions are absolutely equivalent in all inertial systems. This indicates that the Newton's laws do not depends on space, time scale or these have the same mathematical form at any location and duration of time. It characterizes the universality principle of mechanical motions. Let write the Newton equation in the gravitational field, replacing the radius multiplied by the scaling factor α:

$$m\frac{d^2x}{dt^2} = G\frac{m\cdot M}{r^2} \xrightarrow{r'=\alpha r} \frac{d^2r}{dt^2} = \alpha^2\cdot G\frac{m\cdot M}{r'^2} \tag{2}$$

From equation (2), we see, when the radius is multiplied by a constant, the equation retains the form. It expresses the universality of Newton's equation. In short, in the gravitational and the Coulomb's fields, the Newton's equation is equivalent to anywhere in space. The scaling factor changes the value of mass, charge and stability of the bond, thereby ensuring the universality of the law.

Universality of Kepler's laws: The central field is uniform in all directions; therefore, the potential is a function only of the radius Φ (r). In this case, the motion proceeds on the orbital plane. Then Lagrangian:

$$L(r,\dot{r},\dot{\varphi},t) = \frac{m}{2}\left(\dot{r}^2 + r^2\dot{\varphi}\right) + \Phi(r) \tag{3}$$

φ, $\dot{\varphi}$ are the azimuth angle and the azimuth angular velocity.
Due to the universality of Kepler's law in a gravitational field, the derivative in the azimuth of the Lagrange function is a conserving quantity.

$$L = \frac{\partial L}{\partial\dot{\phi}} = m\vec{r}\times\vec{v} = mr^2\dot{\phi} = mrv = const \tag{4}$$

Here $\vec{v} \perp \vec{r}$ and $v = r\dot{\varphi}$.Equation (4) is the law of conservation of momentum. The gravitational field is constant over time and does not consume energy. Therefore, totalenergy of a body converses during that time.

$$E = \frac{m}{2}(\dot{r}^2 + r^2\dot{\varphi}) + \Phi(r) = \frac{m}{2}\dot{r}^2 + \frac{L^2}{2mr^2} + \Phi(r) \tag{5}$$

Here $L^2 = m^2r^4\dot{\phi}^2 L = mrv$ is angle moment. We can determine the geometry and image in accordance with the universality of the law of conservation of angular momentum. The orbit of each planet draws an ellipse .around the sun. The radius of the planet moves along an arc of a circle of length $v\cdot\Delta t$at each time moment Δt. The areas of curve triangle is the same anywhere of the circle:

$$S = \frac{1}{2}rv\cdot\Delta t \tag{6}$$

As previously discussed, $L = mr = const$ is appeared same at radius values and time moment on the motion plane. This demonstrates universality second law of Kepler.

2. Results demonstrating the importance of the universality of classical laws

The universality of the laws of classical physics is an essential tool for building a virtual laboratory, which turns out to be equal to a real technical one. Conducting numerical experiments using a virtual laboratory [1], students will themselves derive equations (1) and (2) for the classical law of aggravation.

Deriving the law of gravity.

In accordance with the universality of Newton's law, measurements of a numerical experiment can be carried out using different values of mass with a constant radius (table 1).Here $r = 500m$.

Table 1: Data of experiment force in kg and mass in

	1	2	3
$m\,(kg)$	2	5	10
$F\,(N)$	19.6038	49.0098	98.0188
$F/m[m/s^2]$	9.8019	9.8019	9.80188

When the mass of the earth is constant, gravity is directly related to the mass of the body. As the gravitational force is the interaction of the earth and the body mass:

$$F \sim Mm$$

The following table shows the estimated values of gravity in different values of radius.

Table 2: Data of experiment force and distance. Here $m = 10kg$

	1	2	3	4
$r\,[10^3, m]$	6381	63815	3682	6380
$F(H)$	98.0042	97.9889	97.9735	98.0350

Due to the universality of Newton's law at different scales, we conclude that gravity is inversely proportional to the distance $F \sim 1/r^n$. Combining the conclusions of the two experiments, one can write that the gravity force is $F \sim \frac{Mm}{r^n}$. If we add correlation coefficient, $F = G\frac{Mm}{r^n}$. Here: n,G–uncertain constants. So we showed that the gravitational field Newton's equation is universal for all values of coordinates.

C***alculation of constants using experimental data***

$$\frac{F_1}{F_2} = \left(\frac{r_2}{r_1}\right)^n = \frac{98.0042N}{97.9735N} = \left(\frac{6382000}{6381000}\right)^n, \qquad n = \frac{ln(1.0003134)}{ln(1.0001567)} = 2 \tag{7}$$

Once, defined that $n = 2$.

$$G = \frac{F \cdot r^2}{m \cdot M}, \quad G = \frac{97.973N \cdot (6382 \cdot 10^3)^2 m^2}{10 \cdot 5.980 \cdot 10^{24}\, kg^2} = 6.673 \times 10^{-11} \frac{Hm^2}{kg^2} \tag{8}$$

Note that in the general theory of relativity G acquires a new scale meaning, which determines the curvature in the geometry of the universe**.**

Example-2. Coulombs' law

In the numerical experiment of the Virtual laboratory[2], students will perform the experiment under the guide of teacher.

Charges interaction, Coulomb's field.

To derive the Coulomb's law, we will conduct a numerical experiment. The table below shows the strength of the interaction of two charges in a numerical experiment's. Here universality of Coulomb's law is used as in the case of Newton's one. This interaction is proportional to multiplication the two charges:$F \sim q_1 q_2$ and for values of the force at different values of distance are shown in Table 3, at same distance with different charges in table.

Table 3: Data of experiment force and charge.

	$r\,(m)$	$q_1\,(nC)$	$q_2\,(nC)$	$F\,(nN)$
1	1.5	0.6	1.0	2.38
2	1.5	1.0	1.0	3.96
3	1.5	1.0	1.0	6.34

Table 4: Data of experiment force and distance.

	$r\ (m)$	$q_1\ (nC)$	$q_2\ (nC)$	$F\ (nN)$
1	1.4	1.12	1.0	9.86
2	1.4	1.59	1.0	4.97
3	1.4	2.10	1.0	3.07

From Table 3, we see the Coulomb force is: $F_n \sim \frac{1}{r}$. Here the n degree of r distance is unknown. Now we perform similar calculations as in previous section According to above mention, it can be written relation in next form $F = k\frac{q_1 q_2}{r^n}$. Then performing simple calculation as made for the Newton's law one may obtain $n = 2$. Also using force ratio for two values of the distance coefficient is calculated. So $k = 8.996 \cdot 10^9 N\frac{m^2}{c^2}$.

3. Conclusions

It is shown that the universality of the classical laws of physics is the conceptual and practical tool for constructing a virtual laboratory. Conducting numerical experiments and discussing the data, students can derive mathematical formulas of the basic laws. Moreover, they can formulate laws under the direction of the teacher.

In essence, the universality of classical laws contains geometries created on experimental data and a mathematical formulas. The greatest value of a virtual laboratory is the development of the students' creative thinking, penetrating into the essence of physical phenomena and experiments.

References

[1] Lkhagva, P. Enkhtsetseg, T. Ulambayar et al., *3D virtual laboratory of physics*, Ulaanbaatar, Mongolia, 2017 (CD).

[2] Lkhagva, T. Ulambayar, P. Enkhtsetseg, Virtual laboratory for physics teaching, *Intern, Proc. Econom. Develop. Res.* 37: 319-323, 2012.

LED BASED MINI RAMAN LIDAR FOR HYDROGEN GAS DETECTION

T. Shiina

Chiba University, 1-33 Yayoi-cho, Inage-ku, Chiba-shi, 263-8522 Japan
E-mail: shiina@faculty.chiba-u.jp

Abstract

The Great East Japan Earthquake revealed the fear of hydrogen explosion on Fukushima nuclear power plant in 2011. The treatment of the hydrogen gas is refocused in the view point of its safety. In this study, LED-based mini Raman lidar was developed for hydrogen gas detection. The LED beam is hard to collimate strictly, while it never focuses after the transmission. It gives advantage in the closed space in the viewpoint of human safety concern. The system is so compact and handy that one can use it in any observation direction. The system power consumption is about 2 W. The quantitative hydrogen gas measurement was conducted by using the LED mini lidar and a gas chamber. Hydrogen gas concentration was adjusted by mixing the air and hydrogen gas. As a result, the hydrogen gas concentration could be successfully evaluated with linearity up to 1%.

1. Introduction

The hydrogen gas has been focused for new clean energy source. Fuel cell vehicle (FCV) is installed into the market from 2014 and the hydrogen gas station is increasing in Japan. The fuel cell has been already started to use in home power generation systems from 2008, too. On contrary, the Great East Japan Earthquake revealed the fear of hydrogen explosion on Fukushima nuclear power plant in 2011. The treatment of the hydrogen gas is refocused in the view point of its safety.[1, 2] The current hydrogen gas detectors, however, are mainly contact type, which is the chemical or the semiconductor device.[3, 4] It is hard to get the gas concentration distribution in hydrogen leakage area by these sensors.

As the above backgrounds, we focused on optical sensing for the hydrogen gas detection. The optical sensor is high speed, non-interfered in gas flow, and it has possibility to obtain the concentration distribution of hydrogen gas leakage with remote sensing. The hydrogen gas, however, does not have strong absorption lines in visible and infrared ray regions. It means that light absorption techniques such as Infrared absorption spectrum analysis on DOAS (Differential Optical Absorption Spectroscopy) or DIAL (Differential Absorption Lidar) cannot be adapted for the hydrogen gas.[5, 6]

In this study, Raman lidar was applied to the hydrogen gas detection.[7] Raman scattering has the wavelength shift due to the scattering material. The hydrogen gas causes the strong Raman scattering especially in near ultra violet region. The LED lamp was utilized as a lidar pulse transmitting light. The LED beam is hard to collimate strictly, while the optical alignment becomes robust on the lidar set-up, that is, the usual lidar needs to make a strict alignment for the transmitting beam and receiver view angle, in the case of the LED lidar, the LED beam has a wider divergence, and a part of the transmitting beam always enter in the receiver's field of view. The LED lamp does not need to have a cooling device and its power consumption is quite low. The system can operate with DC power supply. The power-LED for illumination (1 W, 12 ns @365 nm) was installed with the repetition frequency of 500 kHz.

The quantitative hydrogen gas measurement was conducted by using the LED mini lidar and a gas chamber. Hydrogen gas concentration was adjusted by mixing the air and hydrogen gas. As a result, the hydrogen gas concentration could be successfully evaluated with linearity up to 1%.

2. Principle

Lidar consists of transmitter part, receiver part and signal processing part. Figure 1 shows the typical setup of lidar system.[8]-[10] The pulsed laser beam was collimated and fired into the atmosphere with almost parallel to the receiver's optical axis. The optical receiver is adjusted its field of view (FOV) to detect the lidar echo from the target with an adequate signal-to-noise ratio. A traditional lidar has individual optics (biaxial optics) for a laser transmitter and a receiver, and the system has a blind area, which the transmitting beam cannot enter within a receiver's FOV, especially in near range. As the receiver's FOV is wider, or the beam divergence is wider, the blind area will be shortened, while the background light enters a lot into the receiver. As a result, the signal-to-noise ratio of the lidar echo will be lower.

The traditional large lidar is good at the long-range observation from a few kilometers to a hundred kilometers. On the other hand, the compact lidar is not a down-size one of the large lidar. Table 1 shows the spatial and time scales in atmospheric phenomena. The large phenomena such as HP / LP have a large spatial and time scales, while the small phenomena like tornado takes small spatial and time scales. That is, the small phenomena become small structure and quick motion. To detect and visualize such small phenomena, the compact lidar should follow with the quick motion with high resolution. Furthermore, near range detection is often a sensing in human living space. In that meaning, the transmitting optical power should keep eye-safety. It causes the limit of transmitting power and the selection of optical wavelength.

The lidar is not efficient in the near range detection because of blind area. When the transmitting beam has enough power, its divergence can be wider than the receiver's FOV. Such a lidar optics is free from misalignment and the system becomes robust. Under that consideration, the overlap efficiency of the lidar optics was calculated as shown in Fig. 2. The main graph (right) indicates the transmitting / receiving ratio under the transmitting beam divergence of 10mrad. The sub-graph (left) shows the overlap function and its shift to the transmitting / receiving ratio. In the case that the receiver's FOV is 5 mrad and 3 mrad, the transmitting/receiving ratio keeps 30% and 10%, respectively. In other words, when the transmitting beam power has a margin of 3 – 10 times compared with its usual operation, one can utilize this advantage.

The signal-to-noise ratio was estimated with the lidar equation. The transmitting pulse power was 1 W(=10 nJ/10 ns), and the backscattering coefficient of Raman scattering from the hydrogen gas was assumed as 10^{-3} than the Mie scattering echo intensity. The red line shows the same level of the echo and noise, that is, signal-to-noise ratio is 1. In the daytime measurement is quite severe, while the nighttime measurement will be possible within 30 – 40 m. The power-LED for illumination has the enough power to transmit the above intensity.

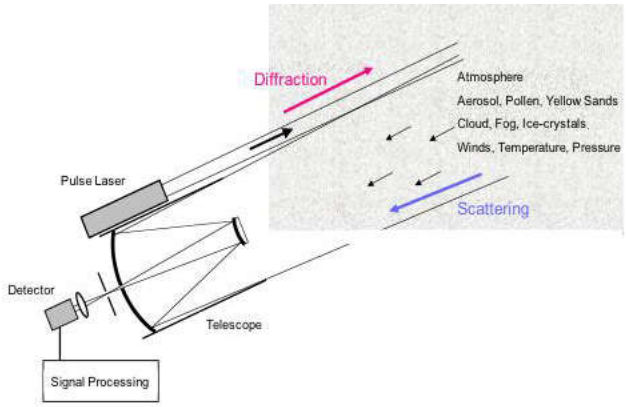

Figure 1: Principle of Lidar observation.

Table 1: Spatial and time scales of atmosphere.

Phenomena	Spatial Scale	Time Scale
HP /LP	1,000 km	10 hrs
Typhoon	100 km	3 hrs
Convection	50 km	2 hrs
Thunder Clouds	10 km	1 hrs
Cumulus	2 km	10 min
Down Burst	600 m	7 min
Tornado	200 m	5 min
Boundary Layer	60 m	10 s

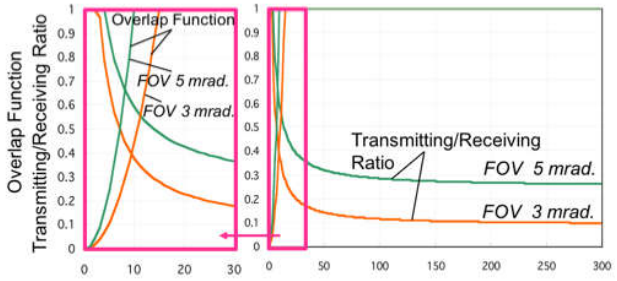

Figure 2: Overlap efficiency of lidar optics.

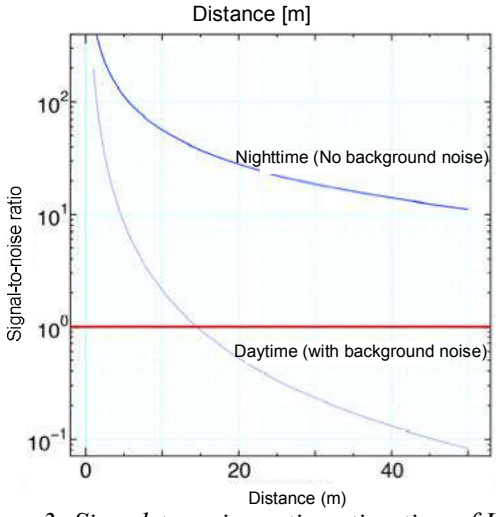

Figure 3: Signal-to-noise ratio estimation of LED-based lidar.

3. Development

Considering the above estimation, we developed the LED-based mini Raman lidar. The LED lamp module of the optical power of <1 W (=10 nJ/10 ns) was used as the lidar light source. The wavelength of LED light is 365 nm, and the wavelengths of Raman scattering echoes become 400 nm for atmospheric nitrogen, 420 nm for water vapor and 430 nm for hydrogen gas. The LED mini Raman lidar optics is shown with photo in Fig.4. The Nitrogen Raman echo was detected separately with the dichroic mirror and the other gas Raman echoes were detected by changing the optical interference filter with a filter wheel. All of the wavelength widths of the interference filters were 10 nm. It is the same width the used LED spectrum. The transmitting beam was enlarged to 50 mmϕ. Its divergence was about 10mrad. The LED pulsed power was <1 W, while the pulse repetition frequency was 500 kHz. The receiving telescope was Cassegrain type of the aperture of 127 mmϕ. The receiver's FOV was 3 mrad. The transmitting power is so weak, and the echo detection is photon counting with photomultipliers. The observation range is aimed up to 20 – 30 m for hydrogen Raman signal. This observation range design comes from the facility space of a nuclear reactor to detect the hydrogen gas leakage.

The high-speed photon counter was developed, too. It can follow the pulse repetition frequency of >500 kHz.[11] Its time resolution is 1ns. It is equivalent to the spatial (distance) resolution of 0.15 m. It has 2 channels, and their simultaneous measurements are possible with a single input or output trigger signal.

Figure 5 shows the observed Raman echo of the atmospheric nitrogen gas and the water vapor. The observation direction is nearly horizontal. The experiment was conducted in night time. Trees were captured at 80m ahead. Accumulation was 3.5 minutes. Nitrogen echo was obtained up to 70 m (Fig.5(a)). After that the fluorescence echo of the tree was also detected at 80m. The atmospheric nitrogen is stable and its echo waveform becomes smooth. On the other hand, the water vapor echo had fluctuation because of low counts (Fig.5(b)). It was drastically changed by depending on the humidity. In the figure, the humidity was 25% on Feb. 7 in fine day, while it was 90% on Feb. 9 in rain day. The observation range of the water vapor was 70 m, which is equal to that of the nitrogen echo. The fluorescence echoes of trees were detected, too.

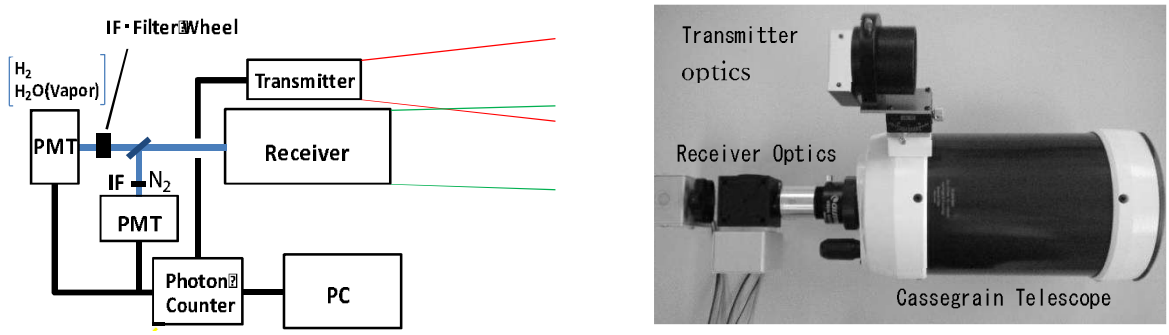

(a) Optical structure *(b) Lidar setup*

Figure 4: LED mini-Raman Lidar.

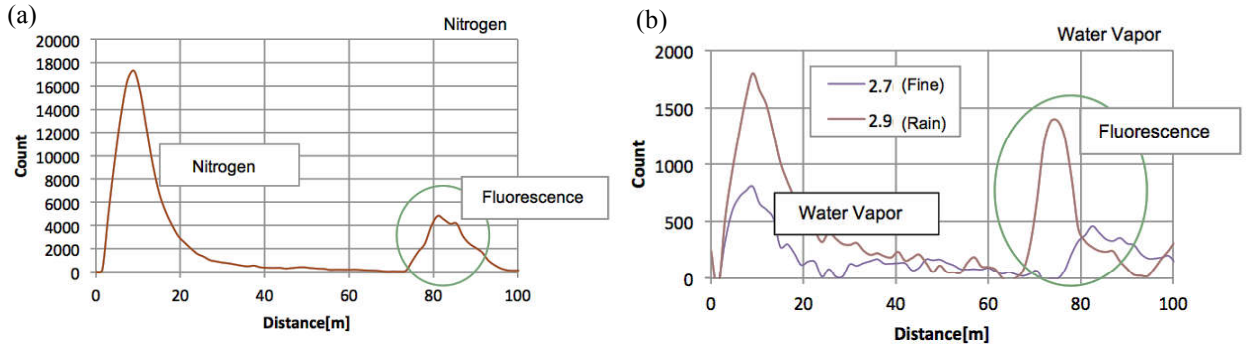

Figure 5: Atmospheric measurement by LED mini-Raman lidar.

4. Hydrogen Gas Observation

The quantitative measurement of hydrogen gas was conducted with a large gas chamber as shown in Fig.6. The hydrogen gas chamber has an aperture of 200 mm and a length of 500 mm. Pyrex glass of 10 mm thickness was used for light path windows to restrict the fluorescent light. It was set 5 m ahead from the LED mini Raman lidar. The transmitting beam was adjusted its optical path against the receiver's field of view to cross both of optical paths at the chamber. The hydrogen gas concentration was adjusted by vacuuming the air inside the chamber of 0.5 Pa and inserting the 100% hydrogen. This procedure repeated twice, and the hydrogen gas concentration of 75% was prepared. We also confirmed the air and hydrogen gases were well mixed in the chamber. After the first measurement, hydrogen gas concentration set to half, that is, 37.5% by vacuuming the inside gas of 0.5 Pa and inserting the air. Repeating these procedures, hydrogen gas concentration was adjusted as 18.8%, 9.4%, 4.7%, and 2.4%.

Experimental results are shown in Fig.7. The accumulation time was 3.5min. The hydrogen Raman echo was appeared on the fluorescent light from the Pyrex glass. Figure 7(a) shows enlargement of the peak change of the echo signals. Depending on the hydrogen gas concentration, the peak counts were changed. The echo counts of hydrogen gas Raman signal were subtracted from the reference echo (0% hydrogen gas). The results were shown in Fig.7(b). The errors were large, which came from the inexact concentration control of the hydrogen gas and the fluctuation of the fluorescent light, while the linear change was obtained down to the lowest concentration of a few percent. The Raman echo counts were remained at the 0% hydrogen gas concentration. We regarded hydrogen concentration after the procedure of vacuuming the content gas of 0.5 Pa and inserting the air two times as equal to 0%. It caused the remained echo counts at 0% concentration. And the fluctuation of the fluorescent light peak echo will cause it, too.

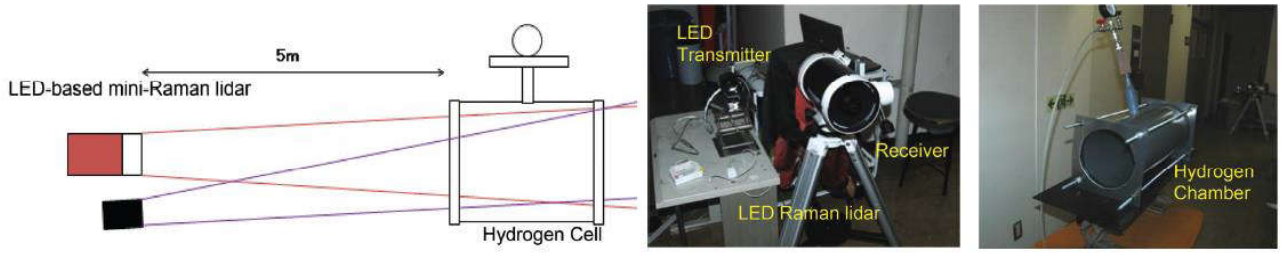

(a) Experimental Setup for hydrogen gas *(b) Apparatuses*

Figure 6: Hydrogen gas measurement.

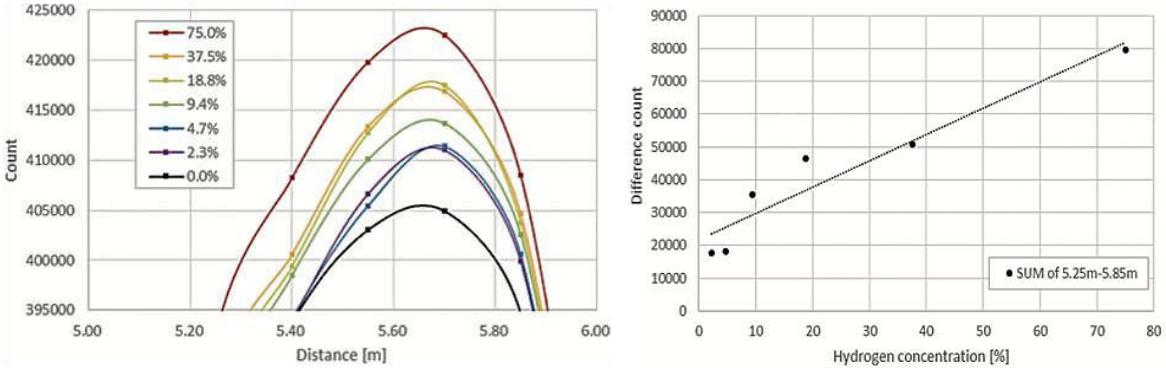

(a) Raw signasl form the hydrogen Raman echo *(b) Variation of Raman echo against hydrogen concentration*

Figure 7: Experimental results of Raman echo counts of hydrogen gas.

5. Summary

We developed the LED-based mini Raman lidars for quantitative measurement of hydrogen gas. The current minimal detection limit of hydrogen gas concentration is 1% at the observation range of 0 – 20 m with this LED-based mini-lidar. The accumulation time is 3.5 min. The Raman signal is weak. It is 1/1000 of the Mie scattering signals. Our current experiments were limited in nighttime and at indoor; the artificial light was no effect for Raman signal detecting even if in the case of the LED-based lidar. The application of the Raman echo detection for a certain gas sensing such as CO_2, water vapor, and O_3, will be possible.

The hydrogen has a potential to become major energy resource. It will be popular in daily life near future. On contrary, its dangerousness is important to recognize once more. Remote sensing device for leaked hydrogen gas is essential. Compact and mini Raman lidars will be one of the solutions.

Acknowledgements

This study was granted by Chubu Electric Power Co., Inc. from 2013 – 2016. Shikoku research institution Inc. was cooperated on the outdoor experiment, too. The author really appreciates to these companies.

References

[1] H. Ninomiya, I. Asahi, S. Sugimoto et al., Development of Remote Sensing Technology for Hydrogen Gas Concentration Measurement Using Raman Scattering Effect, *IEEJ Trans. Electron. Inf. Syst.* 129: 1181-1185, 2009.
[2] C.E. Thomas, Fuel cell and battery electric vehicles compared, *Hydrogen Energy* 34: 6005-6020, 2009.
[3] H. Gu, Z. Wang, Y. Hu, Hydrogen gas sensors based on semiconductor oxide nanostructures, *Sensors* 12: 5517-5550, 2012.
[4] X.Q. Zeng, M.L. Latimer, Z.L. Xiao et al., Hydrogen gas sensing with networks of ultrasmall palladium nanowires formed on filteration membranes, *Nano let.* 11: 262-268, 2011.
[5] H. Volten, J.B. Bergwerff, M. Haaima et al., Two instruments based on differential optical absorption spectroscopy (DOAS) to measure accurate ammonia concentrations in the atmosphere, *Atmos. Meas. Tech.* 5: 413-427, 2012.
[6] S.M. Spuler, K.S. Repasky, B. Morley et al., Field-deployable diode-laser-based differential absorption lider (DIAL) for profiling water vapor, *Atmos. Meas. Tech.* 8: 1073-1087, 2015.
[7] T. Fukuchi, T. Shiina Eds., *Industrial application for laser remote sensing*, Bentham Science Publishers, 2012.
[8] R.M. Measures, *Laser Remote Sensing; Fundamentals and Applications*, John Wiley & Sons, New York, 1984.
[9] T. Fujii, T. Fukuchi Eds., *Laser Remote Sensing*, Taylor&Francis, 2005.
[10] C. Weitkamp Eds.. *Lidar: Range-Resolved Optical Remote Sensing of the Atmosphere*, Springer, 2005.
[11] N. Britun, A. Nikiforov Eds. *Photon Counting - Fundamentals and Applications*, Chapter 11 Intech Open, 2018.

FULLY DIFFERENTIAL CROSS SECTIONS OF PROTON-HYDROGEN AND ANTIPROTON- HYDROGEN COLLISIONS

G. Zorigt*, L. Khenmedekh, Ch. Aldarmaa

Department of Physics, School of Applied Sciences, Mongolian Science and Technology University
**E-mail: g_zorigt@yahoo.com*

Abstract

Nonrelativistic collision of proton and antiproton with hydrogen atom described by solving time-dependent Schrodinger equation numerically. Coulomb wave function discrete variable method (CWDVR) had been used to calculate electron wave function evolution, while projectile defined classically, moving along the straight line trajectories with constant velocity. The ionization amplitude calculated by projection of the wave function into continuum wave function of the hydrogen electron. The fully differential cross sections calculated depending on projectile impact energy, scattering angle and electron ejection energy and angles. Our results in good agreement with the relativistic calculation results.

1. Introduction

Theory of charged particle collision had been studied from establishment of quantum theory in the middle of 1920s, beginning from the Born theory of collision. Experimental equipment's are continuously improved, and can accurately measure the differential cross sections of the collision. From the computational point of view, the antiproton collision with Hydrogen atom is simplest case, because against the proton case, the electron capture channel doesn't contribute to the collision cross section.

In the resent years, few theoretical works among them perturbative theory of Voitkiv et al [1] based on Continuum Distorted Wave (CDW) approximation. At low energy of projectile, for few hundred keV, the perturbation theory become inaccurate, and non perturbative theory can be applied. Recently, developed few non preturbative theories, treating the projectile classically, as moving along a straight line, but the atomic electrons treated quantum mechanically. Among them, coupler pseudo state (CP) theory of McGovern et al [2,3], time dependent convergent – close – coupling (QM - CCC) approach (Abdurakhmanov et al [4]) , time dependent close coupling (TDCC) method (Ciappina et al [5]) could be mentioned. Recently, Boudarev et al [6] used the relativistic single center semi classical coupled channel approach had been developed to calculate fully differential cross section (FDCS).

In the present study, for the first time, the Coulomb wave functions have been used as a basis in the discrete variable representation (L.Y. Peng, A.F Starace [7]) to study the antiproton-hydrogen collisions. These wave functions have been first expanded into the spherical harmonic functions as they enable to explicitly calculate the time-dependent radial functions. By considering the classical assumption that an antiproton with a particular impact parameter preserves its straight trajectory, we show how the hydrogen electron has temporally evolved from its ground state in the field produced by the presence of the antiproton and compared the results of the FDCS to the previously published theoretical data. In particular, we compare our results for the FDCS-s in the antiproton and proton -atom collision, in which an initially 200 − 900 keV energetic antiproton is momentum transfer 0.1 au. to the previously published results.

2. Theory

Assuming the antiproton moving along the straight trajectory, the atomic electron excitation and/or ionization processes are studied here as functions of the antiproton impact parameter. We adopt numerical approach constructing a space net and calculate the wave function on each knot of the net in the spherical coordinate system. This is accomplished by solving the one of the fundamental equations of the quantum mechanics – the time-dependent Schrödinger equation. Namely, the Schrödinger equation for an electron of the hydrogen atom in the external field is given by

$$i\frac{\partial\Psi(\vec{r},t)}{\partial t} = \left(\hat{H}_0 + \hat{V}(\vec{r},t)\right)\Psi(\vec{r},t) \quad (1)$$

where $\Psi(\vec{r},t)$ is wave function and $\hat{H}_0$ is the Hamiltonian for an electron of a hydrogen atom, $\hat{V}(\vec{r},t)$ is the interaction opreator due to the external field. Assuming that the antiproton or ion moves along the straight line (z-axis), the produced electric potential is expressed as follows

$$\hat{V}(\boldsymbol{r},t) = -\frac{1}{|\boldsymbol{R}(b,0,\upsilon t)-\boldsymbol{r}|} \tag{2}$$

here $\boldsymbol{R}$ is ion radius vector, b is impact parameter, υ is ion velocity, $\boldsymbol{r}$ is electron radius vector, t is time. With this assumption that the antiproton moves along the classical trajectory, the ionization and scattering calculations have been performed in the cases of antiproton-helium [8-10] and antiproton-hydrogen [6] collisions. The total differential cross section is the one of the experimentally verifiable quantities as results of ionization processes. The ionization amplitude is obtained by an overlap integral constructed from the wave functions calculated in the discrete variable representation as

$$T(\varepsilon,\theta_e,\varphi_e,b\,,\varphi_b) = \langle\psi^-|\psi_f\rangle \tag{3}$$

where for impact parameter $\vec{b}(b,\varphi_b)$, an electron ionization amplitude for scattering angle θ_e,φ_e and energy ε is $T(\varepsilon,\theta_e,\varphi_e,b\,,\varphi_b)$ and ψ^- is continuum wave function, ψ_f is wave function at a final moment in the calculation.

Next, the ionization amplitude is converted from its impact parameter representation to the momentum transport representation by two-dimensional Fourier transform as in Bondarev et al. [3].

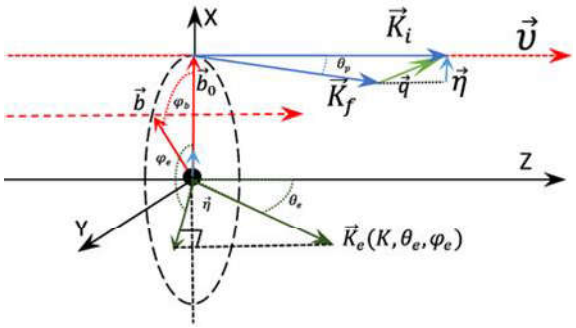

Figure 1. Antiproton enters along z-axis. $\vec{K}_i,\vec{K}_f$ are initial and final momenta of the antiproton $\vec{K}_e$ is the electron momentum, $\vec{\eta}$ is the component perpendicular to the antiproton velocity $\vec{\upsilon}$ of the momentum transport from the antiproton to the atom.

The geometric construction of the vectors for impact parameter and momentum transport is illustrated schematically in Fig. 1. As shown in Figure 1, the ionization amplitude is obtained by the integral given in Eq. (4) in the representation of $\vec{\eta}$ - the perpendicular component of the momentum transfer to the antiproton's velocity $\vec{\upsilon}$ as follows,

$$T(\varepsilon,\theta_e,\varphi_e,\eta,\varphi_\eta) = \frac{1}{2\pi}\int d\vec{b}e^{i\vec{\eta}\vec{b}}e^{i\delta(b)}T(\varepsilon,\theta_e,\varphi_e,b\,,\varphi_b) \tag{4}$$

here $\delta(b)$ is the phase shift accounting the ion-atom interaction as given by [14]

$$\delta(b) = \frac{2Z_PZ_T}{\upsilon}\ln(\upsilon b) \tag{5}$$

Due to the momentum transfer $\vec{\eta}(\eta,\varphi_\eta)$ from the antiproton, assume that the electron is ionized with an energy of ε with angle θ_e,φ_e. The corresponding ionization fully differential cross section is expressed as

$$\frac{d^3\sigma}{d\varepsilon d\Omega_e d\Omega_P} = \vec{K}_i\vec{K}_f\left|T(\varepsilon,\theta_e,\varphi_e,\eta,\varphi_\eta)\right|^2 \tag{6}$$

where $d\Omega_p$ is differentiation of the scattering solid angle for the antiproton, K_i, K_f are initial and final momenta of the antiproton. In the relative coordinate system, the atomic nucleus is assumed to be at rest and antiproton is expressed with its reduced mass.

3. Results and Discussion

We consider the proton and antiproton collision with Hydrogen atom in it is ground state. First, we calculated the ionization amplitude for projectile flying along straight-line trajectory with constant velocity and for given impact parameter. Impact parameter b varies with in the integral (0.1-100 a.u.). We used symmetry properties (axial symmetry around the Z- axis, which is parallel to projectile trajectory and mirror symmetry with respect to the scattering plane.) to economy the calculations. The ionization amplitudes for different impact parameters are collected as a data for further calculations of scattering amplitude with given projectile scattering angle using formula (4), in which the integrals calculated numerically.
Then fully differential cross sections are obtained via the formula (6). We perform calculations for different projectile energies and different scattering angles. Fig. 2 shows differential cross sections of ionization for projectile with energy of 200 keV and scattering angle of 0.2 mrad, where electron ejection energy is equal to 4 eV and 10 eV. As it seen from the Fig. 2, our calculations are in agreement with the relativistic cross sections of Bondarev et al [6]. At this impact energy, the first Born cross section binary peak is much higher in comparison with our calculated result, but the recoil peak is much smaller.

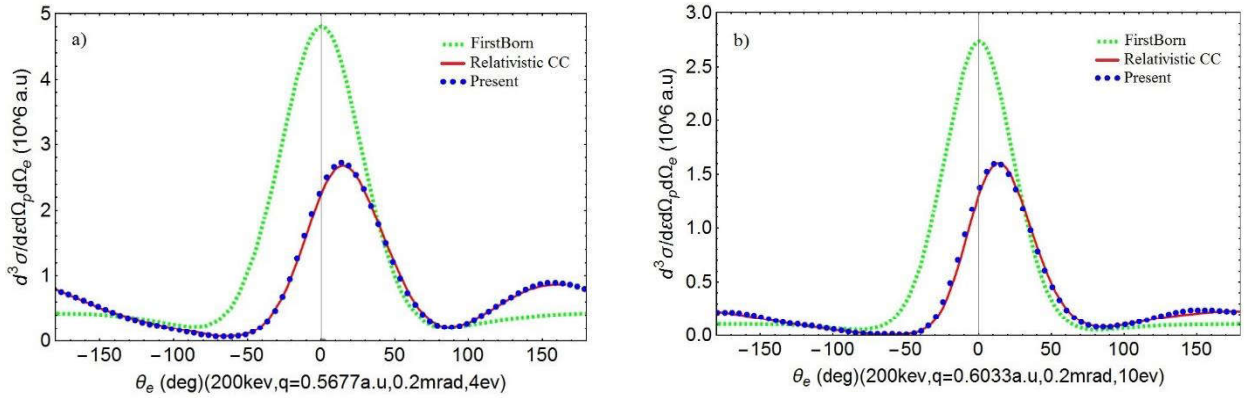

Figure 2. FDCS in the scattering plane. The collision parameters: The projectile energy of 200keV and scattering angle of 0.2mrad, where electron ejection energy is equal to a). 4 eV and b).10eV .The results of the relativistic coupled-channel are from Refs.[6]

Notable shift of the binary and recoil peak direction relative to the first Born peak directions also observed. At the 500keV energy differences between numerical results and first Born approximation has same feature as in the previous energy but getting smaller. Fig. 3.

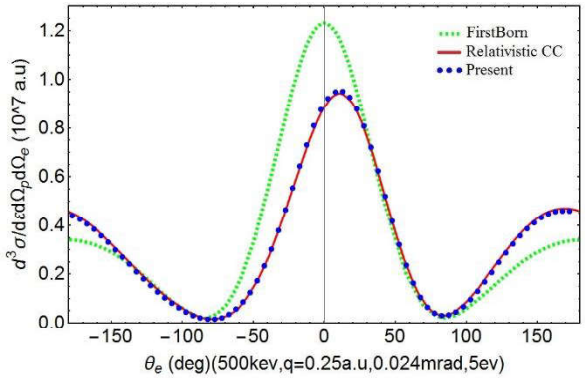

Figure 3. FDCS in the scattering plane.The collision parameters:The projectile energy of 500keV and scattering angle of 0.024mrad, where electron ejection energy is equal to 5eV .The results of the relativistic coupled-channel are from Refs.[6].

Next, we compare our proton and antiproton impact ionization results with CDW cross sections Voitikiv et.al [1]. In this case, the binary and recoil peak height and shift for proton are opposite in comparison to the antiproton case, the first Born results lie between proton and antiproton cases. This is of course, the projectile charge effect; first Born approximation does not defend on projectile charge. On the other hand, CDW approximation can handle with charge sign difference, as seen from Fig. 4 but did not fully take into account in comparison to the numerical solution of the Schrödinger equation. At the highest projectile energy of 900keV the CDW cross sections are nearly coincide with numerical cross sections as seen from Fig. 4c.

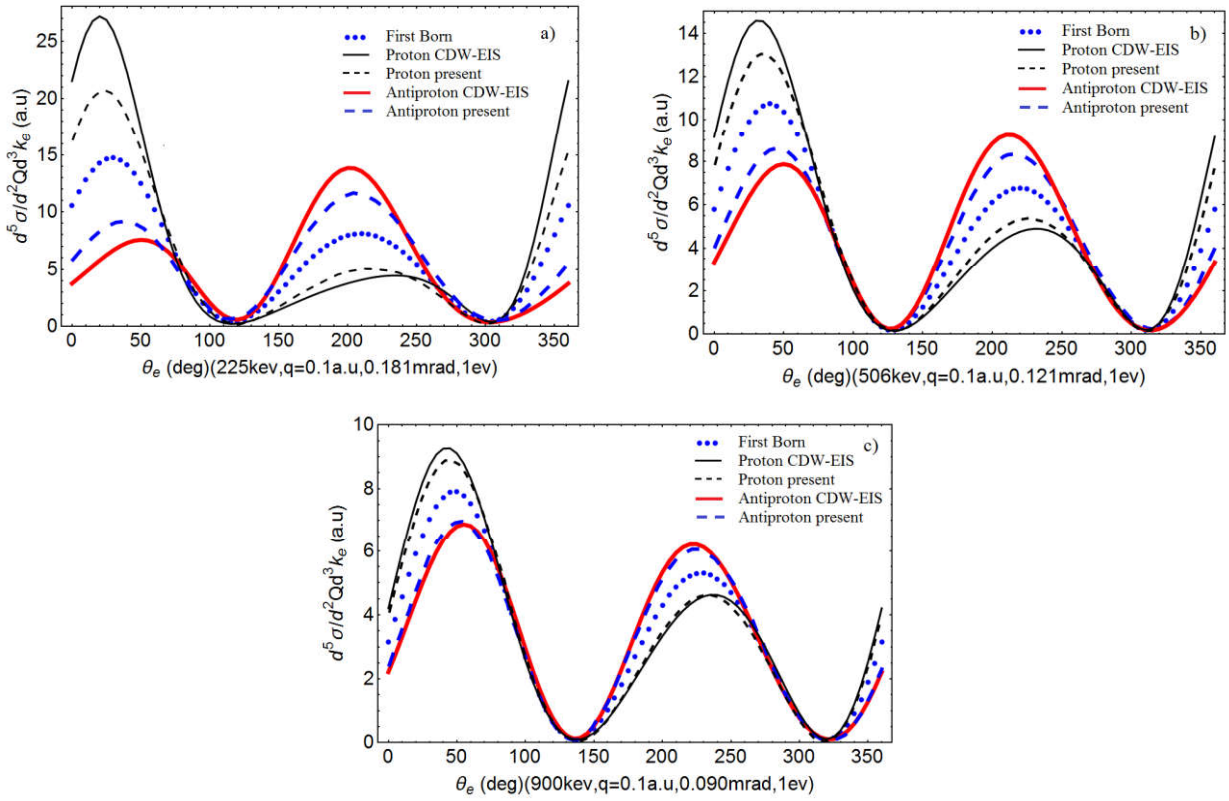

Figure 4. FDCS in the scattering plane. The collision parameters:The electron ejection energy 1eV and the component perpendicular to the antiproton velocity of the momentum transport 0.1 a.u. , projectile energy where is equal to a). 225 keV and b).506 keV c). 900 keV.The results of the CDW from Refs.[1].

4. Conclusions

Fully differential ionization cross sections of proton and antiproton collisions with Hydrogen atom are obtained from the numerical solutions of the time dependent Schrödinger equation using CWDVR method.
The calculated FDCS-s are agree will with the relativistic FDCS of Bondarev et al [6]. We test our numerical method for different incident energiys and scattering angles of the projectile and get convergence to the relativistic cross sections Bondarev et al.

References

[1] A.B. Voitkiv, J. Ullrich, Three-body Coulomb dynamic in hydrogen ionization by protons and antiprotons at intermediate collision velocities, *J. Phys. Rev. A* 67: 062703, 2003.
[2] M. McGovern, D. Assafrao, J.R. Mohallem, et al., Coincidence studies of He ionized by C^{6+}, Au^{24+}, and Au^{53+}, *J. Phys. Rev. A* 79: 042707, 2009.
[3] M. McGovern, D. Assafrao, J. R. Mohallem, et al., Pseudostate methods and differential cross sections for antiproton ionization of atomic hydrogen and helium, *J. Phys. Rev. A* 81: 032708, 2010.
[4] I.B. Abdurakhmanov, A.S. Kadyrov, I. Bray, et al., Differential ionization in antiproton-hydrogen collisions within the convergent-close-coupling approach, *J. Phys. B*: *At. Mol. Opt. Phys.* 44: 165203, 2011.
[5] M.F. Ciappina, T.G. Lee, M.S. Pindzola, et at., Nucleus-nucleus effects in differential cross sections for antiproton-impact ionization of H atoms, *J. Phys. Rev. A* 88: 042714, 2013.

[6] A.I. Bondarev, Y.S. Kozhedub, I.I. Tupitsyn, et al., Relativistic calculations of differential ionization cross sections:Application to antiproton-hydrogen collisions, *J. Phys. Rev. A* 95: 052709, 2017
[7] L.Y. Peng, A.F Starace, Application of Coulomb wave function discrete variable representation to atomic systems in strong laser fields, *J. Chem. Phys.* 125: 154311, 2006
[8] S.Sahoo, S.C. Mukherjee, H.R.J Walters, Ionization of atomic hydrogen and He+ by slow antiprotons, *J. Phys. B: At. Mol. Opt. Phys.* 37: 3227-3237, 2004.
[9] S.Borbely, J.Feist, K. Tokesi, et al., Ionization of helium slow antiproton impact: total and differential cross section, *J. Phys. Rev. A* 90: 052706, 2014.
[10] M. Foster, J. Colgan, M.S. Pindzola, Fully Correlated Electronic Dynamics for Antiproton Impact Ionization of Helium, *J. Phys. Rev. Lett.* 100: 033201, 2008.

PRELIMINARY NEUTRONIC ANALYSIS OF THE LEAD COOLED FAST REACTOR CORE AND SUBASSEMBLY

G. Tsembelmaa[1]*, S. Odmaa[1,2], B. Munkbat[1,2], N. Norov[1,2]

[1]*Nuclear Research Center, Peace avenue/122, Ulaanbaatar, Mongolia,*
[2]*School of Engineering and Applied Sciences, National University of Mongolia, Ikhsurguuliin gudamj/3, Ulaanbaatar, Mongolia,*
**E-mail: tsembelmaa2005@gmail.com*

Abstract

In this work, we have studied the lead-cooled fast reactor (LFR), one of the Gen-IV reactors for which a Russian type reactor with power of 300 MW(e)named BREST-OD-300 is a reference design. The purpose of this study is to investigate the lead-cooled fast reactor core design and to learn SERPENT-2 code as for basis to develop LFR core design for Mongolia.

We have performed the preliminary neutronic analysis of BREST-OD-300 reactor core and three types of the fuel assembly using the continuous energy Monte Carlo SERPENT-2 code and cluster server at Nuclear Research Center, NUM. It is the firstly studied in NRC, NUM as for fast reactor core design and use of Serpent code.

Fuel rods' diameters were different as 9.4 mm, 9.8 mm and 10.5 mm for the fuel assemblies in inner, intermediate and outer zones of the core, however, rod pitch was the same for these subassemblies in three zones.From the obtained results, the fuel assembly with the largest diameter gives higher effective neutron multiplication factor as an expectation, and the fuel assembly with the smallest diameter gives higher conversion ratios.

1. Introduction

Development of nuclear power reactors have been divided into four generation, and Generation-IV(GEN-IV) reactors are being developed and designed since 2005.

Six advanced reactor concepts have been selected for GEN-IV reactors and are being investigated worldwide to meet the challenging goals of effective resource utilization and waste minimization (sustainability), improved safety, enhanced proliferation resistance, and reduced system cost. GEN –IV reactors include Gas-Cooled Fast Reactor (GFR), Sodium Cooled Fast Reactor (SFR), Lead Cooled Fast Reactor (LFR), Molten Salt Reactor (MSR), Very High temperature Reactor (VHTR), and Super Critical Water Reactors (SCWR) [1]. Three of them are fast reactors with closed fuel cycle. Fast neutron reactors are many advantages compared to thermal neutron reactors. In frame of uranium resource utilization, waste management and thermal efficiency.

LFR is based on a closed fuel cycle for efficient conversion of fertile uranium to fissile plutonium (enhanced sustainability), and management of actinides (reduce waste),passive coolant system provides important design simplification (improved economics) and allows for designing decay heat removal systems based on well-known light water technology and passive features (increased safety)[2].

In this work, we have studied the LFR, one of the Gen-IV reactors for which a Russian type reactor with power of 300 MW(e) named BREST-OD-300 is a reference design. LFR is used for multi-purpose such as hydrogen production, water purification beside production of electricity and heat. The purpose of this study is to investigate the LFR core design and to learn SERPENT-2 code as well as help to developLFR core design for Mongolia.

2. Reactor core design

In this work, we have studied the Russian type LFR with power 300MW(e) as a reference design which is one of Gen- IV designsand its subassemblies. BREST-OD-300 uses 3 different types of subassemblies in which diameter of fuel pins in each subassemblies is different, while fuel composition is the same. Main characteristics of BREST-OD –300 reactor are shown in Table 1, and the horizontal and vertical layout of the core are shown in Figure 1. The core has not radial blanket, and issurrounded by reflectorconsist of lead and steel.

Table 1: Main characteristics of BREST-OD-300 [3].

Parameter	Value
Power, MW(e)	300
Thermal power, MW	700
Core shape	square
Fuel type	U-Pu nitride
Fuel enrichment (Pu)	14.6%
Fraction of Pu, %[3]	
$^{238}Pu/^{239}Pu/^{240}Pu/^{241}Pu/^{242}Pu/^{241}Am/^{242}Am/^{242}Am$	0.5/64/28/3.1/1.7/2.1/0.1/0.5
Coolant	lead
Cladding material	Ferritic-martensitic (12% Cr)
Active core height,cm	110
Core diameter, cm	230
Fuel rod pitch, cm	1.3
Fuel assembly pitch, cm	16.9
Gas plenum height, cm	90

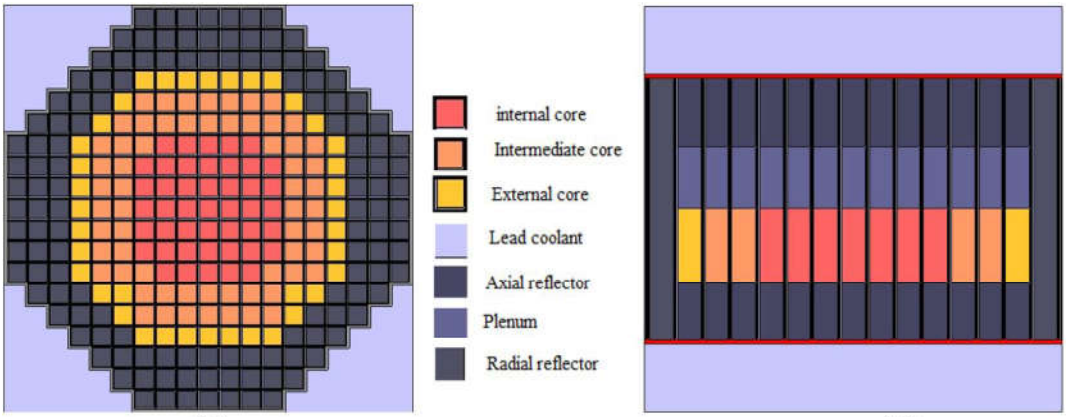

Figure 1: Core layout of horizontal (a) and vertical (b) cross sectional view.

Advantages of lead coolant are high boiling temperature (1740^0C), chemically inactive with air and water, low neutron absorption and moderation. These advantages could improve safety and economic benefits. Nitride fuel is compatible with liquid metal coolant as some advantages with compared other fuel such as high density (ρ=14.5g/cm^3), good thermal property, high melting point (2800^0C). The combination of lead coolant and nitride fuel is the most compatible candidate with a passive safety system.

This reactor core is consisting of three subassemblies in which diameter of fuel pins in each fuel assembly is different, while the fuel composition is the same. In the central zone the pins with the smallest diameter are located while the outer zone holds the fuel pins having the largest diameter.

Characteristics of the fuel pin are shown in Table 2, and the subassembly and the fuel cell are shown in Figure 2.

Table 2: Characteristics of fuel rod [3].

Parameters	Fuel assembly type		
	Zone-1 (R_{small})	Zone-2 (R_{middle})	Zone-3 (R_{large})
Number of the subassembly	45	64	36
Number of the fuel pin in subassembly	156	162	160
Outer diameter of fuel pin, mm	9.4	9.8	10.5
Inner diameter of fuel pin, mm	7.9	8.3	9.0
Gap thickness, mm	0.2		
Cladding thickness, mm	0.5		

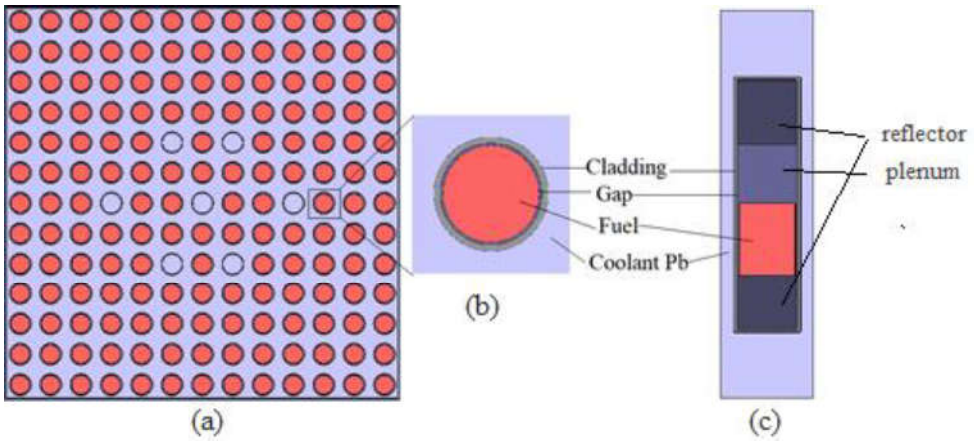

Figure 2: Fuel subassembly (a), horizontal cross section of fuel cell (b) and vertical cross section of fuel cell(c).

3. Calculation tool and results

In this study, we use the continuous energy Monte Carlo simulation tool SERPENT-2 code, version 2.1.30 [5] with JEFF3.1nuclear reaction cross section library and cluster server at the Nuclear Research Center, NUM.

The Serpent is developed and optimized for reactor physics applications since 2004. Serpent code uses Woodcock delta-tracking and unionized energy grid [5]. The main intended use of this code is the generation of homogenized multi-group constants for deterministic 3D core analysis. Similar to other Monte Carlo codes the basic geometry description in Serpent relies on a universe-based constructive solid geometry (CSG) model, which allows the description of practically any twoor three-dimensional fuel or reactor configuration. Serpent supports conventional square and hexagonal lattices, and provides special geometry types for CANDU and randomly-dispersed particle fuels. Input should be provided by completed and corrected geometer and material information.

For neutronic analysis, the number of source neutron per cycle was 10000 for all cases. The number of active cycles was 1000 for all cases. The first 20 cycles were neglected for the error treatment.

The subassembly calculation was considered reflective boundary condition as no leakage of the neutron. The core calculation was considered vacuum boundary condition. An effective neutron multiplication factor (K_{eff}) and the conversion ratio of whole core and three subassemblies are shown in Table 3.

Table 3: Neutronic parameters of core and subassembly.

Geometer	K_{eff}	Conversion ratio
Subassembly at zone-1	1.0817±0.0017	1.0925±0.0007
Subassembly at zone-2	1.1029±0.0004	1.0857±0.0007
Subassembly at zone-3	1.1315±0.0004	1.0759±0.0007
Reactor core	**1.0094±0.0004**	**1.0698±0.0008**

From the obtained results, the fuel assembly with the largest diameter gives higher effective neutron multiplication factor as an expectation. As a reason, fuel rod's pitches in all assembly were the same, but diameters are different, it means an amount of fuel fraction and fissile material was different. In case of conversion ratio, the fuel assembly with the largest diameter gives the lowest value. The conversion ratio is determined by the ratio of the capture of fertile material and absorption of the fissile material.

The neutron spectrum and capture reaction ratio in each subassembly are shown in Figure 3 and 4, respectively. The fuel assembly with the largest diameter is captured low amount neutron in the fertile material (Figure 4.). It is explained by neutron flux and difference of capture reaction rate on three of assemblies which are shown in Figure 3 and Figure 4. K_{eff} of the whole core is 1.00938, its lower than all subassemblies. It may depend on the boundary condition of calculation as we were used reflective BC in core calculation and vacuum BC in subassembly calculation.

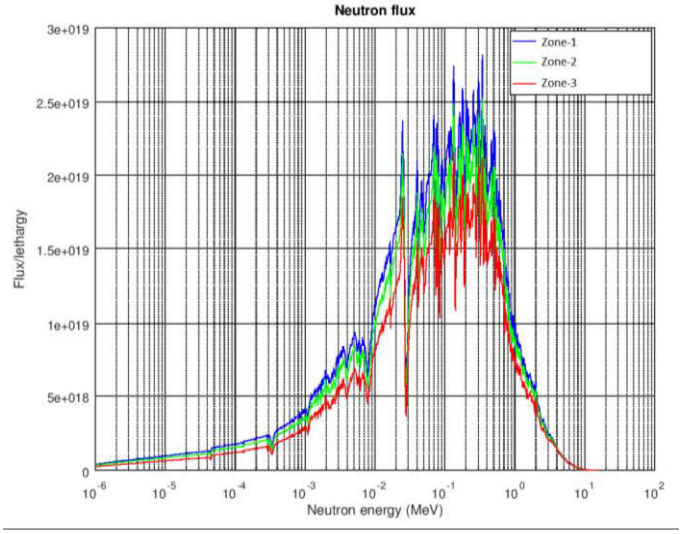

Figure 3: Neutron spectrum on fuel assembly.

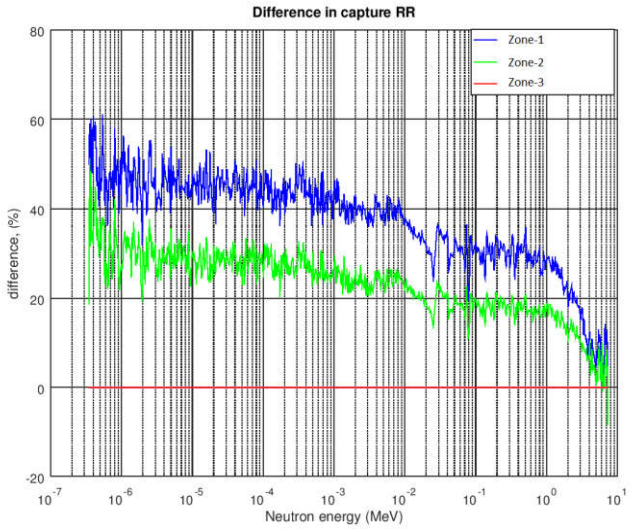

Figure 4: The difference in capture reaction rate.

The linear power distributionof the whole reactor core at the beginning of the cycle(BOC) is shown in Figure 5. The maximum linear power was about 380 W/cm in the center of the reactor core. From the Figure 5, fuel subassembly with different diameters has no impact on power distribution of whole core.

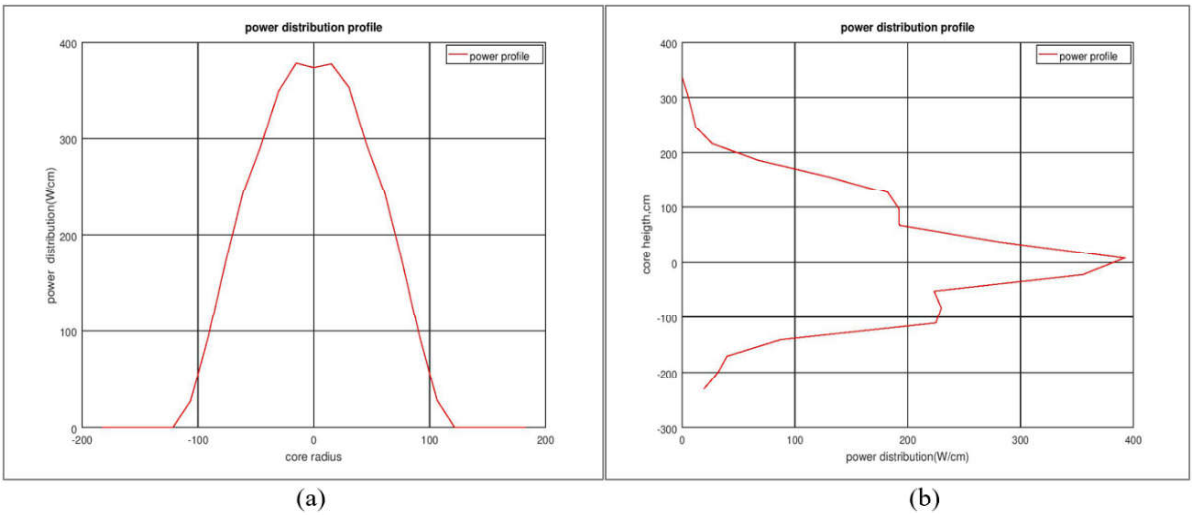

(a) (b)

Figure 5: Linear power distribution (a) radial and (b) axial in the core at BOC, (W/cm).

4. Conclusion

In this work, we have studied LFR, one of the Gen-IV reactors for which a Russian type reactor with power of 300 MW(e) named BREST-OD-300 is a reference design. The purpose of this study was to investigate the LFR core design and to learn SERPENT-2 code. Fuel rods' diameters were different as 9.4 mm, 9.8 mm and 10.5 mm for the fuel assemblies in zone-1, zone-2 and zone-3 of the core, however, rod pitch was the same for these subassemblies in three zones. From obtained results, the fuel assemblies give effective neutron multiplication factor respectively 1.0817 in zone-1, 1.1029 in zone-2and 1.1315 in zone-3 of the core, respectively. Effective neutron multiplication factor of reactor core was 1.0094, and conversion ratio was 1.0698. This is firstly studied in NRC, NUM as fast reactor core design and use of Serpent code, and will be further studied to provide the basis of suitable power reactor for Mongolia.

Acknowledgements

This work is supported by the project from Mongolian Foundation for Science and Technology named "Comparative study on an advanced suitable nuclear reactor in Mongolia".

References

[1] T. Abram, I. Sue, Generation-IV nuclear power: A review of the state of the science, *Energy police* 36: 4323-4330, 2008

[2] *A Technology Roadmap for Generation IV Nuclear Energy Systems*, United States Department of energy nuclear energy research advisory committee, generation IV international forum, US DOE, Washington, DC, 2002.

[3] V. Smirnov, V. Orlov, The lead cooled fast reactor benchmark BREST-OD-300: analysis with sensitivity method*, Proceeding of International Workshop: Nuclear Data Needs for Generation IV Nuclear energy systems*, 173-182, 2005.

[4] H. Khalil, M.J. Leneberry, J.E. Cahalan et al., *Preliminary Assessment of the BREST Reactor Design and Fuel Cycle concept*, Argonne National Laboratory, 2000.

[5] J. Leppanen, *PSG2 / Serpent – a Continuous-energy MonteCarlo Reactor Physics Burnup Calculation Code*, User manual, 2015

NEUTRONIC ANALYSES ON VHTR CORE DESIGN

B. Khukhsuvd[1,2]*, S. Odmaa[1,2], T. Jamiyansuren[2], B. Munkhbat[1,2]

[1] *Department of Chemical and Biological Engineering, School of Engineering and Applied Sciences, National University of Mongolia, Ulaanbaatar, Mongolia*
[2]*Nuclear Research Center, National University of Mongolia, Ulaanbaatar, Mongolia*
**E-mail: b.khukhsuvd@gmail.com*

Abstract

In the present work, we have focused to design an annular and solid cylindrical prismatic, very high temperature reactor (VHTR) core. The fundamental neutronic analyses using the continuous energy Monte Carlo code MVP2.0 and MVPBURN with the nuclear data library of JENDL-4.0 were carried out for the core with power of 100 MW_{th}. In the study, it was used the advanced TRISO fuel with a solid layer of ZrC deposited over the kernel in which ^{235}U was enriched by 20% of. Moreover, we aimed to investigate the possibilities of using alternative thorium-based fuel composition in this reactor. The calculation had been carried out to compare neutronic results of differences between standard uranium dioxide fuel and thorium based fuel.

1. Introduction

The increasing energy needs of many nations require reliance on nuclear energy in near future. To enhance the viability of this option several advanced reactor concepts are currently under development in different countries. The main emphasis in the development of these advanced reactors is on the improved safety, taking advantage of basic physical laws and using completely passive safety systems wherever possible. Very high temperature reactors (VHTRs) are expected to achieve coolant outlet temperatures up to 1000°C, allowing for increased plant efficiency. The VHTR utilize an all-ceramic core, a graphite core structure as moderator and reflector, ceramic-coated fuel particles, complete ceramic fuel elements and a low power density core. The use of refractory core materials combined with single phase inert helium coolant allows high coolant temperature and a high thermal efficiency results in a lot of remarkable advantages. The large thermal capacity of the graphite core and low power density of core, the absence of coolant phase changes, and prompt negative temperature coefficient represent inherent safety advantages and mitigate reactor siting constraints by reducing both cooling water requirements and the consequences of postulated accident. In the VHTRs, main concept is the fuel element. VHTR employs so-called advanced TRISO-CFPs, where the fuel microsphere (kernel) is coated with the solid ZrC layer, carbon buffer, the inner isotropic high-density carbon (IPyC), the silicon carbide (SiC) and the outer isotropic high-density carbon (OPyC) layers. Using this advanced fuel, it maintains thermochemical stability up to a higher temperature and it has higher resistance to chemical attack by fission products.

In our previous papers, we studied the dependence of design parameters of an annular prismatic high temperature gas-cooled reactor (HTGR) which can remove decay heat by passive ways [1]. The purpose of the present study was to design a solid and annular cylindrical prismatic VHTR cores and to perform neutronic analyses of both cores and to compare the obtained results with those for HTGR cores. Secondary objective of this study was to show the thorium oxalate fuel impact for neutronic results.

2. Methodology

2.1. Core design concept

Both cores of solid and annular cylindrical VHTRs consist of hexagonal blocks for fuel, control rods and a replaceable reflector which are made of IG-110 graphite, and both cores surrounded by a permanent reflector that are made of PGX graphite. Design, configuration and size of the core blocks are based on the Japanese prismatic high temperature test reactor (HTTR) core [2-5]. Their main specifications are listed in Table 1 and horizontal cross sections of both cores are displayed in Fig. 1.

Table 1: Main specifications of cores.

Specifications	Solid cylindrical VHTR	Annular cylindrical VHTR
Thermal power, MW_{th}	100	
Core temperature, °C	850	
Effective height of an active core, m	6.38	6.38
Equivalent outer radius of an active core, m	2.46	2.47
Inner reflector radius/pitch, m	0	0.18/0.36
Top and bottom reflector thickness, m	0.58	0.58
Side reflector thickness, m	0.39	0.87
Average power density, W/cm^3	0.82	
Coolant material	Helium gas	
Fuel	UO_2	
Fuel enrichment (wt%)	20	
Total number of fuel blocks	1452	
Number of layers	11	
Total number of CR blocks in core/in outer reflector	407/264	396/264
Number of inner/outer reflector blocks	-	11/264

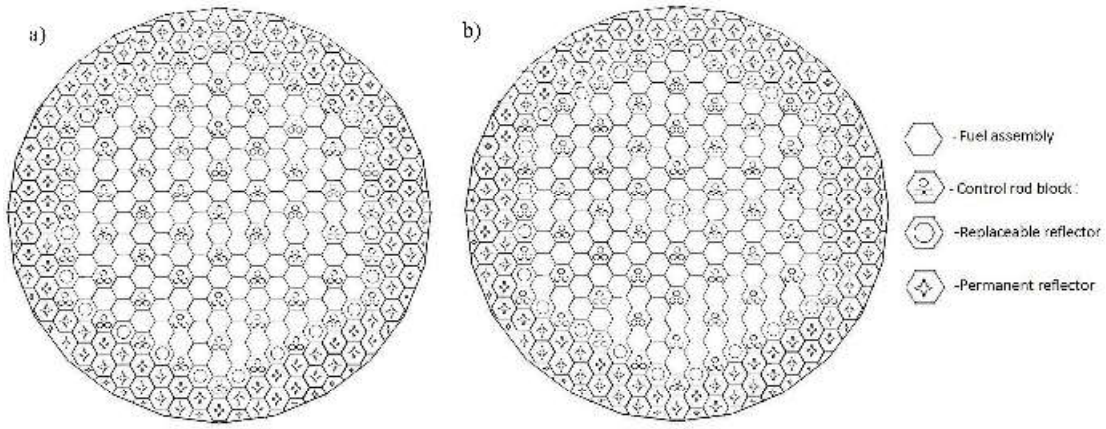

Figure 1: Horizontal cross sections of the both proposed reactor core configuration. a) solid cylindrical core. b) annular cylindrical core.

Dimensions of both cores were determined from parametric conditions which were obtained in our previous works [1, 6].

2.2. Fuel design

The main issue of VHTR as one of the Gen IV reactors is the fuel concept. The fuel concept of VHTR considered in the present work is an advanced TRISO which has an additional layer of ZrC on the fuel kernel as shown in Fig.2. ZrC barrier layer has a much higher temperature capability than SiC layer and it is as an improved barrier against fission product release. This concept was already tested at high temperature up to 1719 K in 500 days under neutron irradiation and both volatile and non-volatile fission products were not released from the advanced TRISO and therefore, its mechanical and safety feature was not degraded at all [7].

In the present work, we used $(U,Th)O_2$ fuel as kernel. Due to the scarcity of natural uranium resources and mismatch between uranium production and reactor requirements, thorium has been explored as an alternative nuclear fuel in reactors. Moreover, main advantages of thorium fuel are that it has higher melting point, somewhat higher thermal conductivity compared conventional uranium dioxide fuel and it does not produce transuranic.

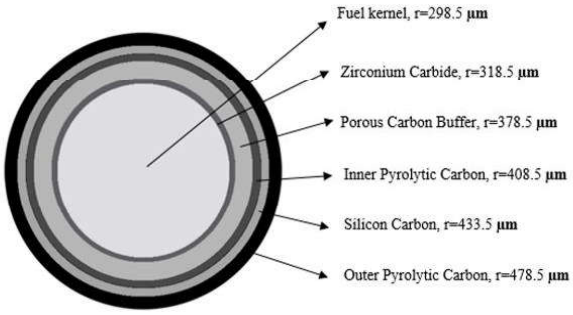

Figure 2: The horizontal cross section of the advanced TRISO particle.

2.3. Neutronic analyses

The neutronic analyses of both cores of the solid and annular cylindrical VHTRs were performed to confirm the possibility of designing a long-life VHTR core with high burnup by using Monte Carlo codes of MVP2.0 [8] and MVPBURN [9] with JENDL4.0 [10] nuclear data library for neutron cross section at arbitrary temperature. In the analyses, all calculations were performed for whole core, and control rods were withdrawn from the core and their locations were filled with the helium gaseous. The most probable value for the neutron multiplication factor (k_{eff}) was evaluated based on track length, collision and analog estimators with the method of maximum likelihood. The number of histories per batch was 50,000 for all analyses and the number of batches was 100 and the first 20 batches were neglected for the statistical treatments. This calculation condition was the same with that was used in our previous works [1,6].

3. Results

The fundamental neutronic analyses results for both cores of annular and solid cylindrical VHTR with power of 100 MWth operating at temperature of 850^{o}C using the continuous energy Monte Carlo code MVP2.0 [8] and MVPBURN [9] with the nuclear data library of JENDL-4.0 [10] were obtained in our previous work [11] as shown in Table 2. Therefore, neutronic results that include neutron fluxes at BOC and EOC, fission reaction rate of ^{235}U isotopes at BOC and EOC were discussed and explained in our previous work [11].

Table 2: Results from neutronic analyses for cores with and without ZrC additional layer on TRISO particles [11].

Core type	ZrC layer on TRISO	K_{eff} in BOC (error SD %))	Core life (year)	Burnup at EOC (GWd/t)
Solid cylindrical HTGR core	No	1.4862(0.0205)	25.5	100.0
	Yes	1.4921(0.0228)	22.9	106.0
Annular cylindrical HTGR core	No	1.4977(0.0183)	26.1	106.0
	Yes	1.5025(0.0207)	23.4	108.0

Core operating temperature of VHTR is higher than that of HTGR, it is needed to determine the neutronic parameters for the core operating at about 1500K temperature. The effective neutron multiplication factor obtained from the calculation with increased temperature was shown in Fig. 3 and it was slightly reduced due to negative reactivity feedback of fuel Doppler effect.

For (Th,U)O_2 kernel, the UO_2 mass fraction in the fuel composition was 25%. The density of thorium oxalate fuel was ρ=11.03 g/cm^3 (95% TD) [12]. ^{235}U was enriched by 20% of. The effective neutron multiplication factor, fuel burnup, core life time were reduced to 1.2458, 40000 MWd/tonnes, 18.4 years, respectively in case of thorium oxalate fuel (Fig. 4, Fig. 5, Fig. 6). Therefore, the total fission reactions rates of ^{235}U throughout the annular cylindrical core with TRIZO particles which consist of UO_2 and (U,Th)O_2 fuel kernel were compared and discussed to describe those results. Fig.6 shows the fission reaction rate of ^{235}U

throughout the annular cylindrical core. It provides that lower fission reaction rate of ^{235}U occurs for core TRIZO fuel particles with $(U,Th)O_2$ kernel. A decrease in fission reaction rate of ^{235}U is related to the fissile isotope fraction in fuel. Even though, only 25% of fuel consists of fissile isotopes, the impact of ^{232}Th still exists. Thorium has about a three-fold larger absorption cross section than ^{238}U in thermal energy. Therefore, ^{232}Th can convert to fissile ^{233}U more readily than ^{238}U can convert to ^{239}Pu in the uranium fuel cycle that implicates the slight change of neutronic features in present work.

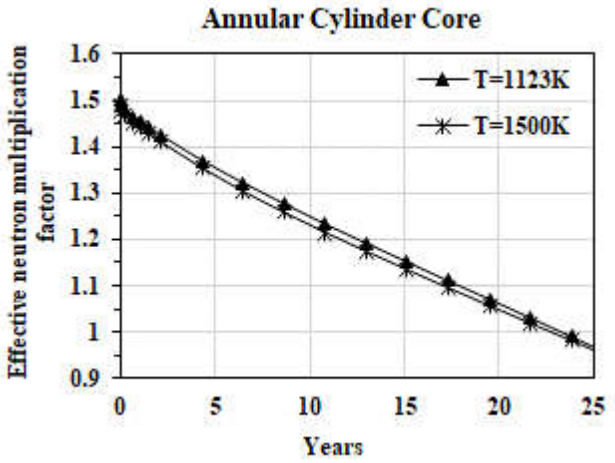

Figure 3: Changes in effective neutron multiplication factor of annular VHTR at different operating temperatures as time.

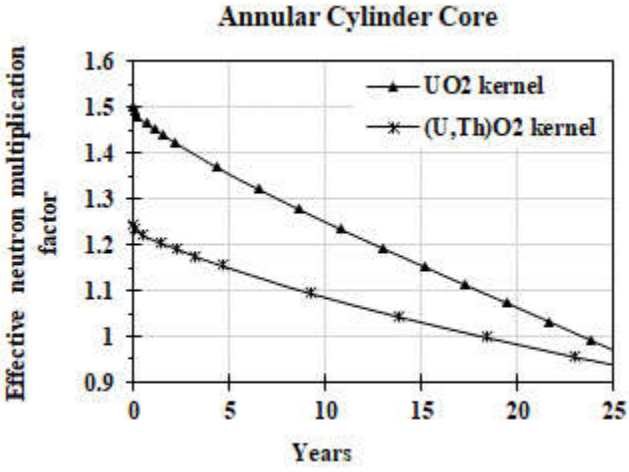

Figure 4: Changes in effective neutron multiplication factor of annular VHTR with different fuel kernel as time.

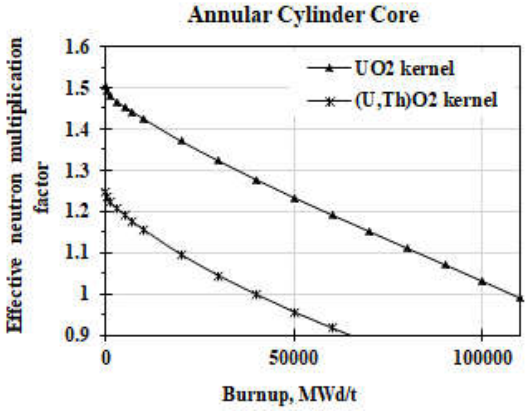

Figure 5: Changes in effective neutron multiplication factor of annular VHTR with different fuel kernel as fuel burnup.

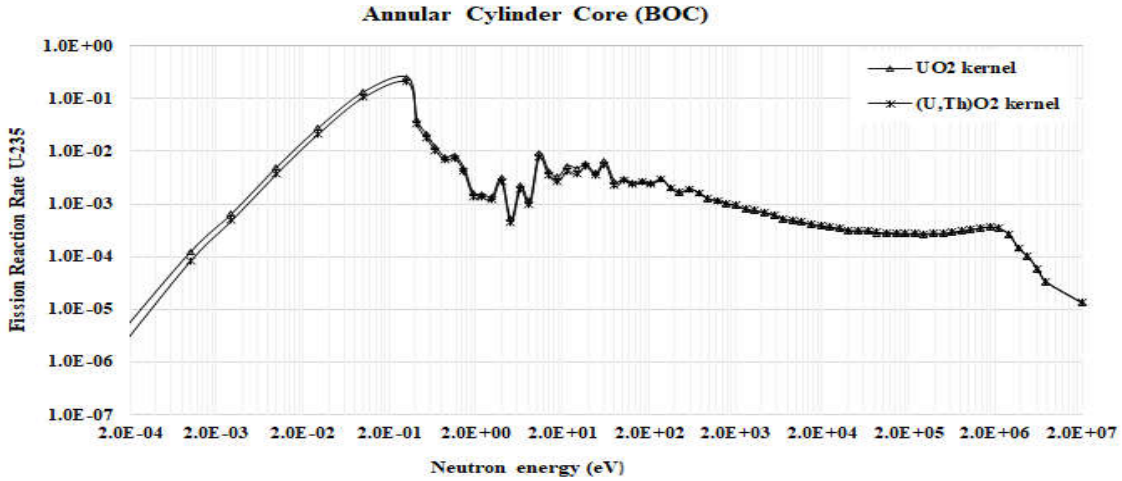

Figure 6: Total fission reaction rates throughout the annular cores with different fuel kernel at BOC.

4. Conclusions

In the present work, we performed the preliminary neutronic analyses for an annular and solid cylindrical prismatic VHTR core with advanced TRISO fuel with a solid layer of ZrC deposited over the kernel and with power of 100 MW_{th} at operating temperature of 1123K. The effective neutron multiplication factor in BOC and discharged burnup were increased, while core lifetime was reduced due to existence of the ZrC layer. Therefore, neutronic analyses using $(Th,U)O_2$ fuel kernel was calculated. Neutronic features of VHTR core with ZrC-containing TRISO which consists of $(Th,U)O_2$ fuel was decreased for long term operation as higher fuel burnup in effect of fissile isotope mass fraction.

Acknowledgements

This work has been done within the framework of the project named "Study on very high temperature reactor" supported by the Asia Research Center-National University Mongolia, Mongolia and Korea Foundation for Advanced Studies, South Korea. The calculation performed at MINATO cluster server, NRC, NUM.

References

[1] S. Odmaa, T. Jamiyansuren, T. Obara et al., Design Parameters in an Annular Prismatic HTGR for Passive Decay Heat Removal, *Annal. Nucl. Ene.* 111: 441-448, 2018.
[2] S. Saito, T. Tanaka, Y. Sudo et al., Design and Safety Consideration in the HTTR, *Energy* 16: 449-458, 1991.
[3] S. Saito, T. Tanaka, Y. Sudo, *Design of HTTR*, JAERI-1332, Japan: Japan Atomic Energy Research Institute, 1994.
[4] S. Shiozawa, S. Fujikawa, T. Lyoku et al., Overview of HTTR Design Features, *Nucl. Eng. Des.* 233: 11-21, 2004.
[5] *Evaluation of HTGR Performance, Benchmark Analysis Related to Initial Testing of the HTTR and HTR-10*, IAEA-TECDOC 1382, IAEA, Vienna, 2003.
[6] S. Odmaa, T. Obara, Neutronic and Thermo-Hydraulic Analysis of a Small, Long-Life HTGR for Passive Decay-Heat Removal, *J. Nucl. Sc. Tech.* 52: 1519-1529, 2015.
[7] R.J.M. Konings, Advanced Concepts in TRISO Fuel, *Comp. Nucl. Mat.* 3: 215-236, 2012
[8] Y. Nagaya, K. Okumura, T. Mori et al., *MVP/GMVP II: General Purpose Monte-Carlo Code for Neutron and Photon Transport Calculations Based on Continuous Energy and Multigroup Methods*, JAERI-1348, Japan: Japan Atomic Energy Research Institute, 2005.
[9] K. Okumura, Y. Nagaya, T. Mori, *MVP-BURN User's Manual*, Japan: Atomic Energy Agency, 2005.
[10] K. Shibata, O. Iwamoto, Ts. Nakagawa et al., Japanese Evaluated Nuclear Data Library-JENDL-4.0, A New Library for Nuclear Science and Engineering, *J. Nucl. Sc. Tech.* 48: 1-30, 2011.
[11] B. Khukhsuvd, S. Odmaa, T. Jamiyansuren, Study on Very High Temperature Reactor core design, Scientific Transaction of the National University of Mongolia, *Physics* 27: 66-72, 2018.
[12] I.S. Kurina, L.S. Gudkov, V.N. Rumyantsev, Investigation of ThO_2 and $(U,Th)0_2$, *Atomic Energy* 92: 461-467, 2002.

DESIGN STUDY ON A SMALL BREED-AND-BURN TYPE FAST REACTOR DEDICATED FOR REMOTE AREAS OF MONGOLIA

A. Tsendsuren[1,2]*, B. Munkhbat[1,2], S. Odmaa[1,2]

[1]*School of Engineering and Applied Sciences, National University of Mongolia,*
Ikh surguulin gudamj-1, Sukhbaatar, Ulaanbaatar 14201, Mongolia
[2]*Nuclear Research Center, National University of Mongolia,*
Peace Avenue-122, Bayanzurkh, Ulaanbaatar 13330, Mongolia
**E-mail: Tseegii0100@gmail.com*

Abstract

In this study, the preliminary design study on a small breed and burn type reactor was carried out. This study was performed in three stages, namely fuel pin, fuel assembly and core calculation. In the first two stages, neutronics calculations was performed in order to investigate fast reactor physics' characteristics and preliminary burnup calculation was carried out in the last stage. The result of burnup calculation showed that the reactor could operate more than 10 years with initially loaded fuel, which is homogenous for whole core.

Key words: Breed-and-Burn, Travelling wave, CANDLE, low-power reactor.

1. Introduction

Energy is central to achieving the interrelated economic, social, and environmental aims of sustainable development. However, if we are to realize this important goal, the kinds of energy we produce and the ways we use them will have to change due to the fact that most of the energy resources are fossil fuels emit poisonous substances, particularly Carbon dioxide which leads major global challenges to increasing global average temperature. Moreover, the cost of electricity generation becomes higher because of the decreasing amount of resources. Therefore, alternative energy source and new and advanced technologies that could provide substantial amount of energy safely, at affordable costs and with near zero emissions, must be promoted. Otherwise, environmental degeneration will accelerate, and global economic growth will be jeopardized.

Nuclear power is among the energy sources and technologies available today that could help meet the challenges. There are about 449 nuclear reactors in operation worldwide and most of countries use Light Water Cooled Reactors (LWRs) which use thermal neutrons in the reactor. However, as of 2014, identified uranium resource in the worldwide could supply current LWRs for about 100 years because of low efficiency of use of natural uranium and inexpediency of closing the nuclear fuel cycle for those reactors that makes production of electricity more expensive. Due to this fact, the nuclear technologies based on fast reactors (FRs) that can utilize both natural and depleted uranium must play an important role large-scale development of nuclear power and make it possible to find the solution to the issue of sustainable power supply without limitations on fuel resources and adverse effect on the environment. Therefore, the most of developed countries have been developing fast reactor technology in order to commercialize it by 2025-2030 [1].

With regards to Mongolia, there are minor fraction of world uranium resource accounting for around 2%. Although the fraction seems small, it can be sufficient provided that there are few nuclear reactors. As of current energy supply and demand for the country, over 80% of nation's electricity is provided from coal power plants and around 20% of electricity is imported from China and Russia for subordinated provinces and some remote areas. According to the project result conducted by "I-Jen and Mon-Energy LLC" concerning the Sustainable Energy Development of Mongolia in 2013, there would be significant increase in nation's electricity demand as compared to the current demand. For example, in the central regions including capital, it is required to establish new power system with 1920 MWe and in other regions including western and eastern regions and other remoted areas, it is expected that there should be at least 450 MWe in total power by 2025. It means that approximately 100 MWe is required for some remote regions [2].

Fast reactors could sustain the nuclear chain reaction with natural uranium or depleted uranium fuel. This type of reactor, called Breed-and-Burn (B&B), is able to breed the fissile material and burn it in situ, without fuel reprocessing and enrichment. The concept was first proposed by Feinberg [3] in 1958 and further studied by Atefi and Fischer et al. of Brookhaven National Laboratory [4], [5] in 1979 and Feoktistov[5] in

1988. In 1996 Teller et al. [7] proposed a traveling wave core concept in which nuclear breeding/burning wave was ignited and propagates slowly in the axial direction of cylindrical reactor core.

In 1997, Toshinsky [8] proposed a breed and burn reactor concept the core layout of which is similar to that of a conventional fast reactor. The core is composed of several blankets and enriched fuel batches that are radially shuffled in an optimal sequence. At the end of a cycle, the highest burnup fuel batch is discharged and a fresh blanket batch is loaded in place of the blanket batch that has been shuffled to the higher fuel burnup location.

In 2000, Sekimoto [9], pursued Teller's idea and core geometry, proposed the CANDLE reactor in which the igniter region is located at an extremity of the cylindrical core and the axial propagation of the fission region is controlled by the core dimensions and fuel characteristics.

In 2005, Driscoll [10] developed a breed and burn core concept derived from the Gas cooled Fast Reactor (GFR). This core was designed to be fueled with uranium carbide rather than uranium oxide, cladded with an oxide dispersion strengthened (ODS) steel cladding and cooled with helium.

In 2008, the TerraPower LLC team, composed of several scientists who previously worked with Driscoll, announced the development of a traveling wave reactor (TWR). Two general design variants were developed by TerraPower LLC: a travelling-wave concept similar to that proposed by Teller et al., and a standing-wave concept somewhat similar to Toshinsky's concept.

In 2010, the Energy Multiplier Module (EM2), has been proposed by General Atomics (GA) [11]. The core is composed of bricks made of uranium carbide coated in a silicon carbide layer and is cooled with helium. The fission region is expanding in all directions .

Such designs are pursued by various research institutions, mainly Tokyo Institute of Technology, UC Berkeley and Terra Power LLC. Furthermore, the International Atomic Energy Agency (IAEA) devotes a number of its initiatives in support of the development and deployment of innovative FRs and the related closed fuel cycles, recognizing their importance in ensuring the long term sustainability of nuclear power [12, 13].

2. Purpose of study

Considering uranium resources and subordinated provinces and future energy demand of remoted areas in Mongolia, the main objective of this study is to carry out neutronics analyses of a small breed-and-burn type fast reactor-"CANDLE" as it is more preferable energy source for remoted areas where the infrastructure is immature and reactor system is also simple to operate and maintain, and use only natural or depleted uranium. Moreover, availability to ship or transport to the dedicated location is also the main concern for this study.

3. Calculation Condition

With regards to "CANDLE" burning reactor, it is composed of three fuel regions, namely fresh fuel region, burning region, spent fuel region. The fuel burning region is similar to household candle burning as propagating from top to bottom or bottom to top which depends on where the fresh fuel region is located. This is accomplished by transmuting U-238 to Pu-239 in the fresh fuel region and burning the Pu239 in the burning region at the same time. As result of this in situ fissile material production and consumption, reactor can operate continuously without fuel enrichment or reprocessing [14]. The fresh fuel can be only natural uranium or depleted uranium. In this work, the reference "CANDLE" core design parameters [15], [16] were temporary set as shown in Table 1. Uranium nitride (UN) fuel, ferritic-martensitic HT-9 steel cladding and lead bismuth coolant were used.

Calculation was carried out as following:

1. Fuel pin calculation
2. Fuel assembly calculation
3. Core calculation

As for fuel pin calculation, in order to investigate how the effective multiplication factor changes in terms of temperature on uranium nitride fuel in tube in shell cell with different reflective conditions and reflector, fuel pin calculation was carried out.

Later, in order to find how many kilograms enriched uranium (EU) is required to initiate CANDLE burning with UN, we carried out assembly calculation. With this result, we could predict the required EU for the whole core. The assembly consists of 127 UN fuels with 200 cm in length.

Finally, preliminary core calculation was carried out in order to investigate how many years the reactor could sustain criticality with first loaded fuel. The core consist of 169 assemblies with 127 pins and detailed

core characters were shown in Table 1. All calculations were conducted using continuous energy Monte Carlo code MVP/GMVP II [17] and MVP-BURN with the JENDL-3.3 nuclear data library [18].

Table 1: Design parameters for Small CANDLE reactor.

Design parameters	**Values**
Thermal power	350 MWth
Core radius	100 cm
Core height	200 cm
Radial reflector thickness	50 cm
Fuel material	UN, (N-15 enriched)
Cladding material	HT-9
Coolant material	Pb-Bi (44.5, 55.5%)
Cell type	Tube in shell
Coolant channel diameter	0.668 cm
Cladding thickness	0.035 cm
Fuel theoretical density	14.32 g/cm3

4. Preliminary Results and Discussion

The effective multiplication factor (k-eff) evolution for UN-fueled 7 pins with different reflector materials, namely mirror reflective condition, white reflective condition and lead-bismuth was carried out. Temperatures changes were between 300K and 1500K. The mirror reflective condition indicate that no neutron leaves the core and white reflective condition indicates that neutron is isotopically reflected at core outer surface. The results are shown in Figure 1 and Figure 2.

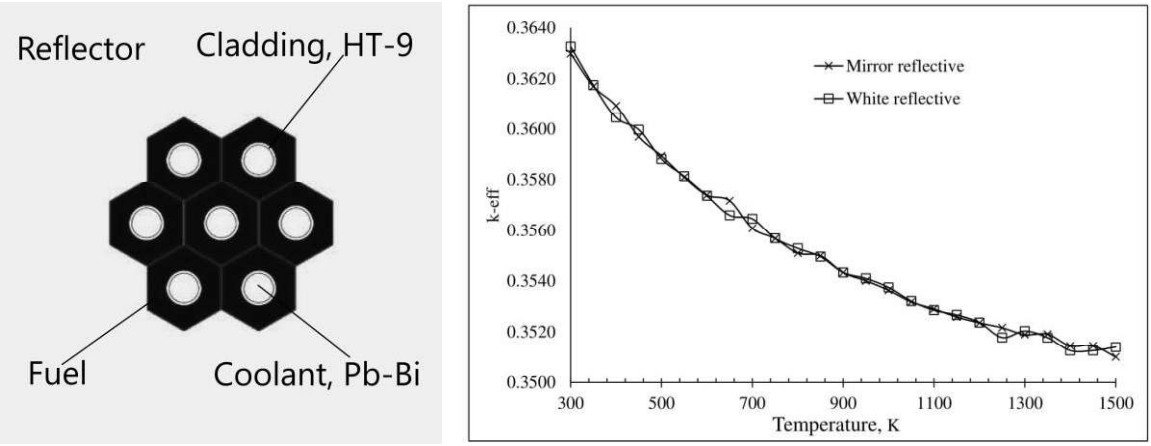

Figure 1: Change of k-eff with mirror and reflective condition.

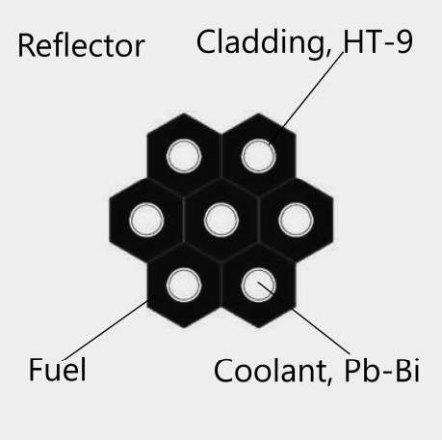

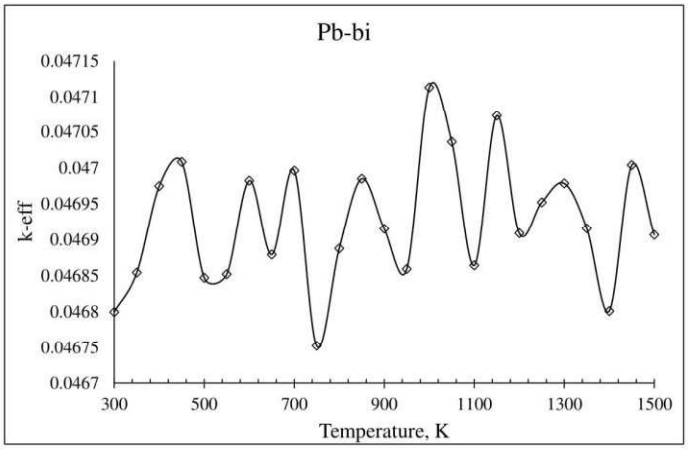

Figure 2: Change of k-eff with Pb-Bi reflector.

From Figure 1 and Figure 2, it was shown that reflector material choice is important for fast reactor. Further analysis is required in our future work. In case of Figure 2, the difference between highest and lowest points is only 0.0004. This means the change of k-eff can be significant small throughout the operation period.

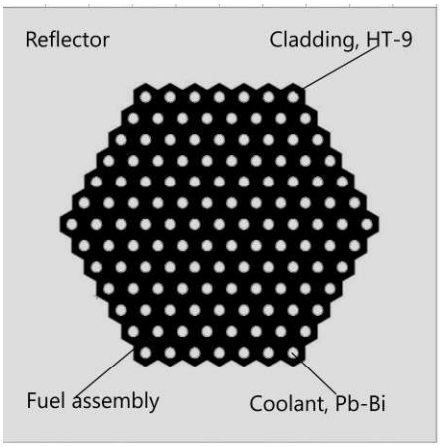

Figure 3: Fuel assembly.

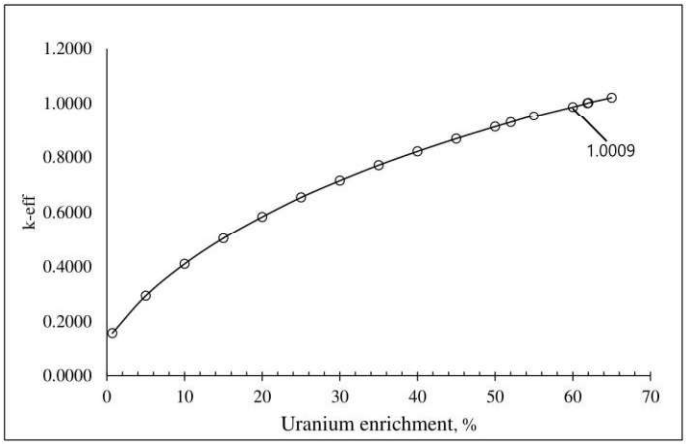

Figure 4: Change of k-eff as a function of uranium enrichment.

The assembly consist of 127 fuel pins with 200cm height, as shown in Figure 3. It is shown in Figure 4 that critic value of k-eff is obtained as a function of uranium enrichment. The mass of U-235 was obtained 183.98kg with 61.9% enrichment, which is 46.42% of total mass of fuel in assembly. The reaction rate spectra for fission and capture of U-235 and U-238 in fuel are illustrated in Figure 5 and Figure 6.

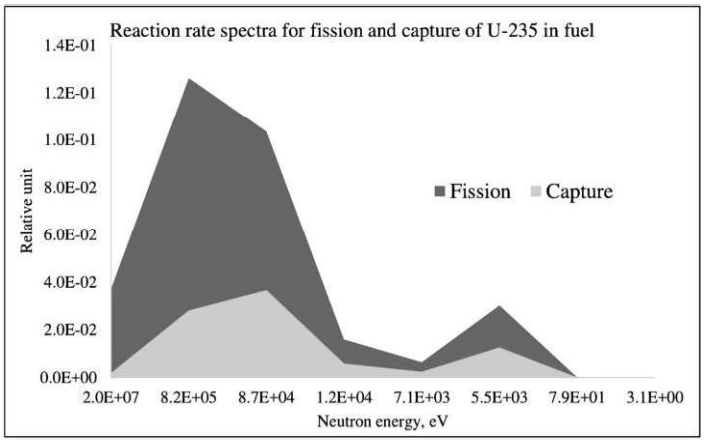

Figure 5: Reaction rate spectra for fission and capture of U-235 in fuel.

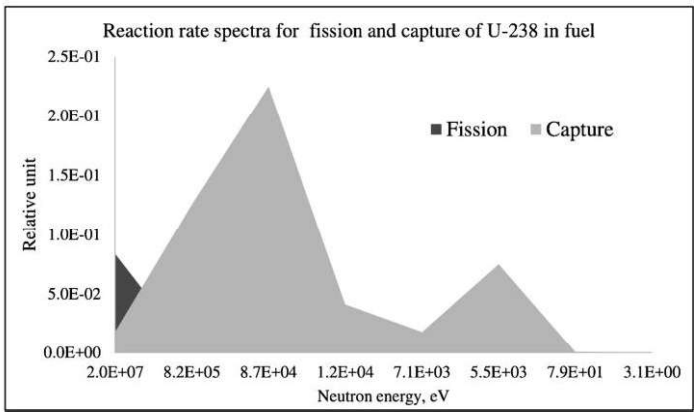

Figure 6: Reaction rate spectra for fission and capture of U-238 in fuel

The fraction of fission reaction is much higher in U-235 as compared with U-238. On the contrary, the fraction of capture reaction is much higher in U-238 as compared with U-235. This is because igniter isotope for chain reaction is U235 and U238 is captured neutron to transmute Pu239, which is fissile material. As result, chain reaction can last for with fission of Pu-239 even the amount of U-235 is depleted.

Core calculation was carried out for homogeneous core (same enrichment in all fuel assembly), as shown in Figure 7. As for the enrichment, If the enrichment is much higher than 8.7%, the reactivity change will become too sensitive or lower than 8.7%, the reactor operation period is too small. Therefore, 8.7% enrichment was selected as a minimum enrichment with appropriate reactor operation period and reactivity change. The details of these issues showed in figure 8.

Looking at details in the figure, the core could sustain criticality for more than 10 years, but k-eff fluctuates throughout the reactor operation period. The difference between maximum and minimum k-eff is 0.0028. At the 5110 days, the reactor became sub-critic (k-eff=0.9976), but it became critic again at 7300 days. Therefore, in order to solve these issues, further study is required. The horizontal line in the figure indicates the criticality.

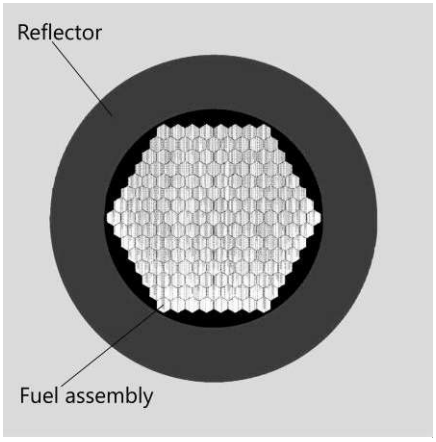

Figure 7: Core configuration.

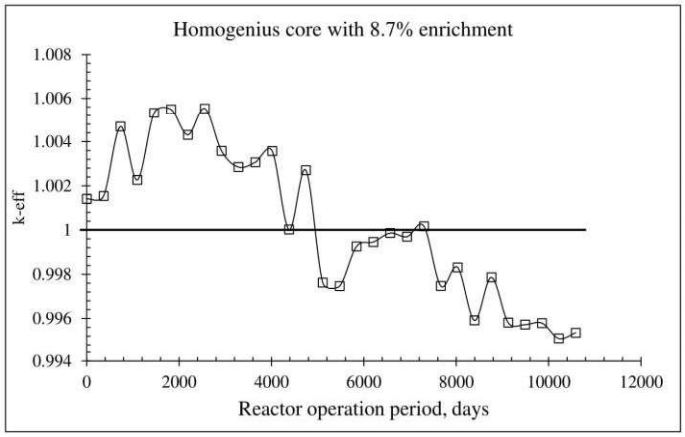

Figure 8: Change of k-eff from reactor operation period with 350 MWth power.

5. Conclusion

As for the fuel pin calculation, the k-eff in terms of temperature was continuously declined when the core had reflective conditions due to the Doppler broadening effect, which is more effective for ceramic fuels, UN as compared with metal fuels in the fast reactor. However, as for the different reflector material, Pb-Bi, the k-eff was tend to fluctuate and the difference between maximum and minimum was only 0.0004. Therefore, the reflective material choice is crucial for this core.

In order to reach the criticality, 61.9%-enriched uranium is required for the assembly. That means that 183.98 kg EU is needed to initiate chain reaction. However, the main fissile material, which sustain the chain

reaction, is Pu-239 via transmutation. Since the required amount of EU is known for ignition in the assembly, from here we could predict the total required fissile material for the initial core.

Through the core calculation, homogeneous core with 8.7% enrichment was analylised. The result showed that the core (EU-8.7%) could operate more than 10 years.

The study is still in progress. Therefore, further analyses will be carried out for heterogeneous core. The reactor other parameters such as the power peaking factor and power density will be calculated.

Acknowledgments

All calculations were carried out using MINATO at Nuclear Research Center, National University of Mongolia. Moreover, this work was supported by "Comparative study on an advanced, suitable nuclear reactor in Mongolia Project" which was funded by Mongolian Foundation for Science and Technology (MFST).

References

[1] IAEA, Fast Reactors Provide Sustainable Nuclear Power for Thousands of Years, 2013.
[2] I-Jen, Mon-Energy LLC, *Project on Sustainable Energy Development of Mongolia,* TT No. 7619-MON, 2013.
[3] S.M. Feinberg, Discussion Comment, *ICPUAE*, Geneva, Switzerland, 1958.
[4] B. Atefi, *An Evaluation of the Breed/Burn Fast Reactor Concept*, in *Department of Nuclear Engineering*, MIT Nuclear engineering publisher, Massachusetts Institute of Technology, USA, 1979.
[5] G.J. Fischer, R.J. Cerbone, *The fast-mixed spectrum reactor Initial feasibility study*, Brookhaven National Laboratory, USA, 1979.
[6] L.P. Feoktistov, An analysis of a concept of a physically safe reactor, *Preprint IAE-4605/4*, Russia, 1-9, 1988.
[7] E. Teller, M. Ishikawa, L. Wood, Completely automated nuclear reactors for long term operation, *The American association of physics teachers Texas meeting*, Lubbock, Texas, 12, 1996.
[8] G.I. Toshinsky, *LMFBR Operation in the Nuclear Cycle without Fuel Reprocessing*, in Advanced reactors safety, American Nuclear Society, Pittsburgh, 1997.
[9] H. Sekimoto, K. Ryu, *A new reactor burnup concept CANDLE*, in Physor, American Nuclear Society, Pittsburgh, 2000.
[10] M. Driscoll, P. Hejzlar, P. Yarsky et al., *Engineering and Physics Optimization of Breed and Burn Fast Reactor Systems*, MIT, Nuclear engineering publisher, Massachusetts Institute of Technology, USA, 2005.
[11] R.W. Schleicher, H. Choi, J. Rawls, Energy Multiplier Module: Advancing the Nuclear Fuel Cycle through Technology Innovations, *Nucl. Technol.* 184: 169-180, 2013.
[12] H. Florent, Maximum Fuel Utilization in Advanced Fast Reactors without Actinides Separation, *PhD Thesis,* University of California, Berkeley, 2010.
[13] C. Di Sanzo, Increasing Fuel Utilization of Breed and Burn Reactors, *PhD Thesis*, University of California, Berkeley, 2014.
[14] H. Sekimoto, *Light a CANDLE*, Tokyo Institute of technology, Japan, 2010.
[15] H. Sekimoto, M. Yan, A design and Safety Features of Small CANDLE Fast Reactor, *Proc. ICAPP 08 Anheim*, CA USA, 8115, 2008.
[16] T. Obara, K. Kuwagaki, J. Nishiyama, *Feasibility of Burning Wave Fast Reactor Concept with Rotational Fuel Shuffling*, IAEA-CN245-051, 2017.
[17] K. Nagaya, K. Okumura, T. Sakurai et al., MVP/GMVP II: General Purpose Monte Carlo Codes for Neutron and Photon Transport Calculations Based on Continuous Energy and Multigroup Method, *JAERI-1348*, Japan Atomic Energy Research Institute, 2005.
[18] K. Shibata, T. Kawano, T. Nakagwa et al., JENDL-3.3: Japanese Evaluated Nuclear Data Library Version 3 Revision-3, *J. Nucl. Sci.Technol.* 39: 1125, 2002.

COMPARISON OF NEUTRON SPECTRUM MEASURED BY NUCLEAR PHOTO EMULSION METHOD WITH MONTE CARLO GEANT4 CODE

D. Otgonsuren*, R. Togoo, A. Tursukh

Institute of Physics and Technology, Mongolian Academy of Sciences, Mongolia
**E-mail:otgonsurenhep@yahoo.com*

Abstract

In the present paper, we have compared neutron energy spectrum measured by nuclear photo emulsion method in the "Energy Plus Transmutation" collaboration at JINR, Russia, with that produced by of Monte Carlo simulation used Geant4 toolkit. Agreement between the results of the two methods is in reasonable.

Keywords: Photoemulsion, Simulation, GEANT4, Neutron energy spectrum, Nuclear transmutation.

1. Introduction

The fuel resources in the world's nuclear power industry, detoxification of used fuels faced with to solve the accelerated driven system is an important problem. In detoxification of radioactive waste and the energy, production process researches the determining the spectra of a neutron energy spectrum in the device is an important part of its improvements. The neutron energy spectrum is traditionally determined by the calorimeter. The second experiment took place on a world-wide test replication of the calorimeter. The objective is to explain the experimental results in a theoretical way, based on the principle of experimental conditions and the design of the experimental designs to simulate the results and to optimize the timing of the above problems.

2. Experimental tools and methods

On the set of lead-uranium (Pb/U) blanket facility with 4 sections (Fig. 1), there were placed photo-emulsion spectrometer (plate) on the top of the first intermediate section [1]. The kinetic energy of fast neutrons generated by the radiation by a proton on the lead target transferred elastically to protons of the photo-emulsion plate leaving tracks by lengths of them there was established the neutron energy distribution [2]. When neutron nucleus falls to the photo-emulsion plate, it interacts with the protons inside, especially with the hydrogen nucleus, and it accepted that most of kinetic energy transfers elastically. The photoemulsion detector is placed on top between the section 1 and 2 of the lead-uranium (Pb/U) facility. There were measured scattering angle θ of proton tracks on the photo-emulsion plates by microscope. Proton energy T_p were determined by their track length R in the photoemulsion measured up to 60 micron and depending the track length approximated by formula [3].

$$T_p = 0.145 * R^{-0.0152 * \log(R) + 0.76} \quad (1)$$

Then the neutron energy is determined by the formula

$$T_n = T_p \, (cos\, \theta_{\widehat{np}})^{-2} \quad (2)$$

where $\theta_{\widehat{np}}$ is the scattering angle between the neutron and the proton.

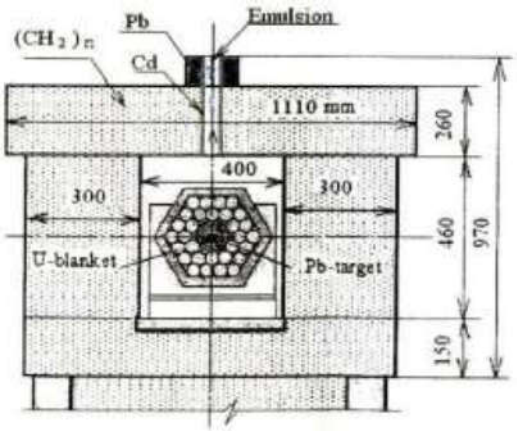

Figure 1. Photoemulsion plate location on the lead-uranium (Pb/U) blanket facility [2].

The incident proton with energy E_p=1.5 GeV is received from Nuclotron accelerator.

3. Physical process simulation

We used GEANT4.10.01 for intra-nuclear cascade simulation when interaction of high energy incident particle with target's particles and G4NDL4.5 cross-section database of processes under 20 MeV by neutron to simulate repeating 1.5 million cases [4,5].

The GEANT4 package has up to 10 GeV energy incident particles simulation packages like Liege (INCL++), Bertini, Binary for physical processes and we used these 3 models.

- The Bertini model is a classic cascade model. It does not use scattering matrix in interaction of incedent particle with matter particles, calculate Bolzman equation of motion. The target nuclears has constant densities up to 3 shells and residual nuclears decomposition happen through its pre-equilibrium and equilibrium states. Prime energy is allowed up to 10 GeV.
- Binary model does calculation of time-dependent process and colitions of hardron-nuleuses are consider disintegration resonances depending on theirs quantum numbers. Incident particles are p, n, pions allowed. This model regards impulses of individual nucleons inside particle and moves along curved trajectories under a nucleon potential.
- Liege model is also make time-depend calculations and use Woods-Saxon or harmonic oscillators potential. It works in 150 MeV–3 GeV energy region for *p, n,* π*, K, d, t,* ^{3}*He,*^{4}*He* particles and 11< A <239 mass numbers of target nucleus. For deexcitation process it combine ablation model (ABLA). This model used in radiation processes successfully.

4. Results and discussions

Simulation is made for the energy spectral distribution of neutrons falling into the photoemulsion plate volume and compared to the value of the experimental data, the high-energy interactions berween the prime incident protons and the target nucleuses as well as the secondary neutrons spatial distribution has been derived from nuclear radiation reactions.

The shown in the Fig.1 the Energy+Transmutation device on which the photoemulsion plates placed on there was measured the proton track lengths which receives energy elastically from coming neutrons as well as their scattering vertical angles and then the protons kinetic energies are calculated by the formula (1) after subtracting backgrounds. In addition, the neutron energies are calculated by the formula (2) and shown on the Fig.2 by the black dots.

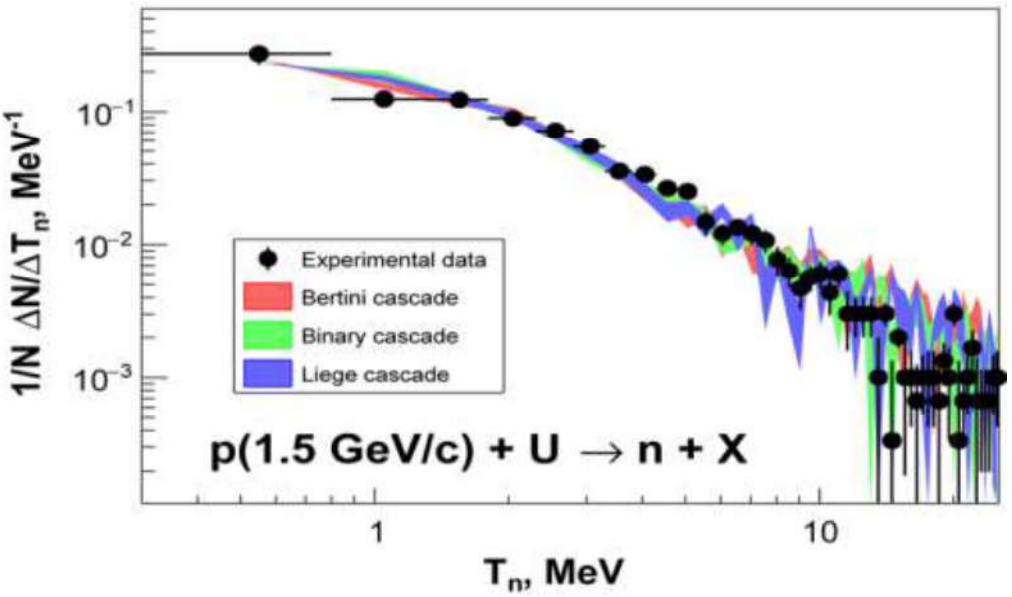

Figure 2. Normalized distributions of neutron energy.

Here are the theoretical distributions performed by Bertini, Binari, and Liege cascade models shown respectively in red, green and blue colors, as well as their statistical errors. As mentioned above 1.5 million repeats of calculation were made and within kinetic energy 3 MeV < T_n < 23 MeV there are Bertini cascade 2954, Binari - 2075 and Liege - 1799 cases respectively. From these 3 models are different by neutron cross-section and has same spectra distribution.

5. Conclusions

Energy distribution spectra is constructed after removing backgrounds for neutrons generated by 1.5 GeV energy proton ray collision with lead-uranium blanket inside the Energy+Transmutation facility which were detected on the photoemulsion plate place in a certain special environment. The form of the neutron energy spectra graphics is similar with the spectra given in [6] measured by another method.

With help of the photoemulsion method shows that it can be used for construting neutron energy distribution in different parts inside of such type of facilities like Energy+Transmutation.

The constructed neutron spectra of the experimental data is compared with the GEANT4 Bertini, Binary and Liege cascade models which does use the G4NDL4.5 neuron reaction cross-section database**.** It shows good agreement between the results of the two methods.

References

[1] M.I. Krivopustov, D. Chultem. I. Adam, et al., On the first experiments on the calorimetry of the uranium blanket using the model of the U/Pb Electro-Nuclear Assembly "Energy plus transmutation" on a 1.5 GeV proton beam of the dubna synchrophasotron, *JINR Preprint,* P1-2000-168, Dubna, 2000.

[2] D. Chultem, M.I. Krivopustov, Yu. A. Batusov, et al., Studies of fast neutron spectra in the uranium blanket of the installation "Energy Plus Transmutation" using proton beam from the JINR Nuclotron at 1.5 GeV, *JINR Preprint*, P1-2003-59, Dubna, 2003.

[3] C.F. Powell, P.H. Fowler, D.H. Perkins, *The study of elementary particles by the photographic method*, Moscow press, 669: 1962.

[4] S. Agostinelli, J. Allison, K. Amako, et al., GEANT4-A simulation toolkit, *Nucl. Instr. Meth. Phys. A*, 506: 250-303, 2003.

[5] A. Krasa, F. Krizek, V. Wagner, et al., Neutron production in spallation reactions of 0.9 and 1.5 GeV protons on a thick lead target. Comparison between experimental data and Monte-Carlo simulations, *JINR Preprint*, E1-2005-46, Dubna, 2005.

[6] L.Stewart, Leakage Neutron Spectrum from a Bare ^{239}Pu Critical Assembly. *Nucl. Sci. Eng.* 8: 595-597, 1960.

SUBCRITICAL ASSEMBLY FOR NEUTRON MULTIPLICATION

D. Baatarkhuu[1], S. Odmaa[1,2]*, Ch. Saikhanbayar[1], Ts. Zolbadral[1]

[1]*Nuclear Research Center, National University of Mongolia, Ulaanbaatar, Mongolia.*
[2]*Department of Chemical and Biological Engineering, School of Engineering and Applied Sciences, National University of Mongolia, Ulaanbaatar, Mongolia.*
**E-mail: odmaa@seas.num.edu.mn*

Abstract

A subcritical assembly is an equipment where the nuclear-fission chain reaction is initiated and maintained using an external neutron source. It is a valuable educational and research tool where in a safe way many reactor parameters can be measured. In the frame of the Mongolian state policy on usage of radioactive minerals and nuclear energy, and IAEA-TC project for establishing and developing of subcritical assembly for enhancing national nuclear research and education capabilities will be likely implemented in coming years. For these reasons, we strive to provide more information about working principle, structure and applications of a subcritical assembly through this work.

1. Introduction

The gamma and neutron beams from nuclear reactors, particle accelerators and radioisotope sources are generally used for fundamental and applied nuclear physics research. Recently, subcritical assembly, in which the neutron beam from uranium fission is multiplied at subcritical condition, is commonly used for nuclear researches. The first subcritical assembly was designed in Russia [1] and since then it has been developed and operated in over 20 countries (table 1).

The basic working principle of the subassembly is the same as the neutron multiplication in critical nuclear reactor. Therefore, it is suitable to study nuclear reactor operations and critical condition for neutron multiplication at safe situation using subcritical assembly [2].

Table 1: Several subcritical assemblies.

country, name of assembly	effective multiplication factor, K_{eff}	neutron flux [$n \cdot cm^{-2} \cdot s^{-1}$]	neutron source	neutron energy
Ukraine	>0.98	~2.4×10^{10}	electron accelerator	thermal, cold
Belarus, "Yalina-thermal"	>0.98	~$1,5\times 10^{11}$	^{252}Cf, neutron generator	thermal
Belarus, "Yalina-fast"	>0.96	~1.5×10^{11}	Pu-Be, ^{252}Cf, neutron generator	thermal, fast
China, "Venus-1"	0.90÷0,98	~10^9	^{241}Am-Be, ^{252}Cf	thermal
France, "Masurca"	0.95÷1,00	~10^{10}	^{252}Cf, electron accelerator	thermal, fast
Belgium, "Quinevere"	0.96÷0,98	~10^{11}	proton accelerator	fast
Mexico, "Zacatecas"	~0.82	~10^9	Pu-Be	thermal, fast
Jordan	0.94÷0.95	~1.4×10^9	Pu-Be	thermal, fast
Netherland	~0.92	~10^{10}	^{252}Cf, electron accelerator	fast, thermal
Russia, Dubna	>0.97	~$10^9\div10^{10}$	proton accelerator	fast, thermal
Russia, Moscow	>0.98	~10^{11}	^{52}Cf, electron accelerator	fast, thermal

Ghana	~0.95	~10^9	^{228}Ra-Be	thermal
Canada, (future)	>0.98	~10^{11}	100÷200 MeV electron accelerator	fast, thermal

Recently, a subcritical assembly with accelerator source in a safe operation is used for research on nuclear reactor neutron, transmutation for long-lived radioisotopes in high level radioactive waste and energy generation [3].

2. Objective of the subcritical assembly

In the frame of the Mongolian state policy on usage of radioactive minerals and nuclear energy, the plan of establishing the center for nuclear science and technology in cooperation with ROSATOM is currently being pursued and the IAEA-TC project for establishing and developing of subcritical assembly for enhancing national nuclear research and education capabilities will be likely implemented, subject to government funding and commitment, in coming years. These actions give us the following several opportunities:

- To establish experimental facility for basic and applied research on nuclear reactor physics and nuclear energy,
- To strengthen the fundamental and applied research and educational activities on neutron physics,
- To enhance research and development on nuclear energy utilization and to do feasibility study related to this issue,
- To continuously train and develop nuclear human resource domestically and to increase on-the-job training.

The objective of the present paper is to explain the structure of the subassembly and its effective usage for research on nuclear reactor and neutron physics.

3. The principle of neutron multiplication in the subcritical assembly

The structural and operational principle of the subcritical assembly is the same with these in nuclear reactor and it is a compound, heterogeneous system including neutron source, moderator, reflector and nuclear fuel. The neutron source is placed in the center of the subcritical assembly and hexagonal fuel elements with ^{235}U and moderators are located in surrounding the neutron source. The uranium nuclides make a fission by the source neutron and induce more neutrons. These new neutrons are slowing-down in the moderator and produce more neutrons as in nuclear chain reaction. This is the neutron multiplication process in the subcritical assembly [4].

4. Subcritical condition of the subcritical assembly

If the number of next generation neutrons in a chain reaction is less than that in the preceding generation, it is called "subcritical condition". The condition for non-self-sustaining uranium fission reaction in the subcritical assembly is determined by fuel element structure, amount of fuel elements and subcritical mass of fuel element. The effective neutron multiplication factor, k_{eff} (which is the ratio of neutron numbers in next generation to the previous one) is less than one in subcritical condition. This is the defining condition for subcritical assembly operation. The main requirements for the subcritical assembly are not only to operate safely, but also to provide high neutron flux for various researches. The neutron multiplication is not uniform throughout its core depending on the structure so that k_{eff} is calculated as the average over its spatial dependency. k_{eff} of early subcritical assemblies with radioactive isotope source for neutron were 0.95÷0.96, and more recently it reached to 0.98÷0.99 in the case of MASURKA, France. For YALINA-FAST, TERMAL, Belarus k_{eff} even reaches to nearly 1 at the center of the assembly core [5].

5. Type of the subcritical assembly

Subcritical assemblies are classified by several different characteristics including neutron source, neutron energy and operational conditions as follows.

***A. By neutron source*:**

- Radioactive isotope neutron source such as ^{239}*Pu-Be,* ^{240}*Am-Be,* ^{252}*Cf,* ^{235}*Pu-Be*,
- Nuclear particle accelerator (for transmutation of long-lived radioactive nuclides in high level waste, fission of actinide nuclides, and energy generation)
  - Electron accelerator
  - Neutron generator using *(D,D)*, *(D,T)* reactions
  - Proton accelerator
- Coupled both sources.

B. By neutron energy and research purpose:

- Thermal neutron ,
- Fast neutron ,
- Intermediate energy neutron.

C. By operating condition:

- Continuous (radioactive isotope neutron source),
- Pulse.

6. Structure of the subcritical assembly

Main structure of the common subcritical assembly consists of the following systems:

- Control system,
- Facility for inducing initial neutron- target,
- Accelerator, beam transferring system,
- Neutron multiplication and fuel system,
- Moderator and reflector,
- Neutron field for research ,
- Shielding and cooling system.

In Fig. 1, structure of Jordan subcritical assembly is shown as an example. Jordan subcritical assembly is uranium fueled light water moderated and reflected small nuclear reactor facility, designed for the purpose of education, training, and experimental research. JSA is designed to never reach criticality; while being capable of sustaining nuclear chain reaction in the presence of an extraneous neutron source, criticality safety is maintained at all times by its design with a large reactivity margin compared to a critical system [6].

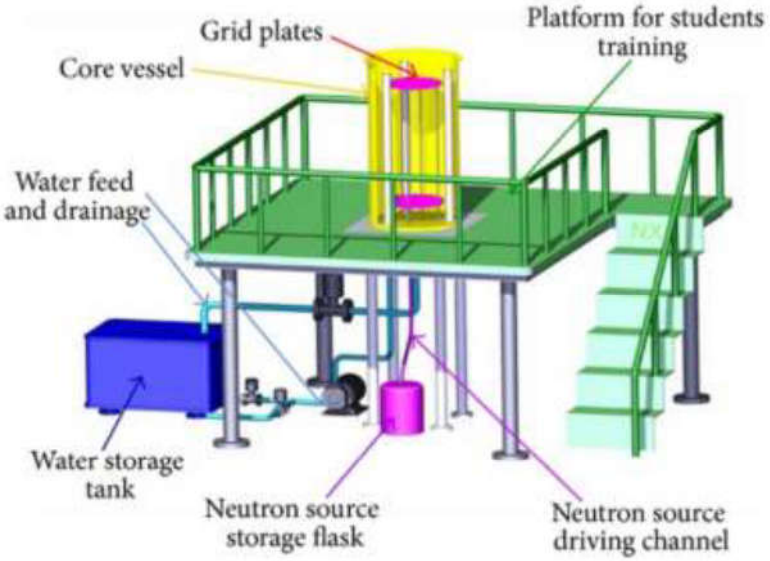

Figure 1: Jordan subcritical assembly [6].

6.1. Some feature of subcritical assembly with accelerator

The neutron multiplying feature of the subassembly and initial neutron flux depends on the uranium enrichment, uranium amount and design of moderator-reflector. The radionuclide source as *Cf-252* and *Pu-Be* is commonly used as the initial neutron source. However, sometimes accelerators are used instead of external neutron sources to enhance the neutron flux and neutron energy, because of this, its operating condition becomes close to critical state. The disadvantage of the accelerator system is higher in expense and cost. There are several special systems, which facilitate the accelerated particles to reach to the neutron converting target with higher neutron flux in case of subcritical assembly with accelerator.

In subcritical assemblies with an electron accelerator, the initial neutrons are induced by photo-nuclear reactions *(γ,2n), (γ,n)* in uranium and heavy elements in which photon beams are produced by bremsstrahlung of relativistic electrons. When the number of neutron per accelerated electron is about ~0.1 in average, the neutron yield is ~10^{17}n/c for a subcritical assembly with accelerator of 10-20 mA of electron current [2].

The cost of proton accelerators is higher compared to that of electron accelerators. If the proton energy is more than 300 MeV, the yield of spallation neutrons is improved by several (p,n) reactions in heavy target. If the target is *Pb* or *W*, the neutron yield per 600 MeV proton is about 10÷12, and it reaches ~ 25 for *U* target. Therefore, the efficiency and neutron flux of the assembly could be higher for high proton flux with energy between 1÷1.7 GeV [5]. Hence, the specification and neutron multiplying feature of the subcritical assembly depend on its design, structure, and the system for initial neutron (type of accelerated particle, target, accelerator parameters).

6.2. Example 1: Yalina-fast, thermal, Belarus

The core layout of YALINA assembly is shown in Fig. 2 [7]. Here, neutron sources were radioactive isotopes as *Pu-Be* and ^{252}Cf and neutron generator using *D(d,n)^{3}He*; *T(D,n)^{4}He* (neutron yield of 10^{10} n/s, 1.5×10^{12} n/s and neutron energy of 2.5 MeV and 14.0 MeV, and pulse generator with the frequency of 1Hz-10 kHz).

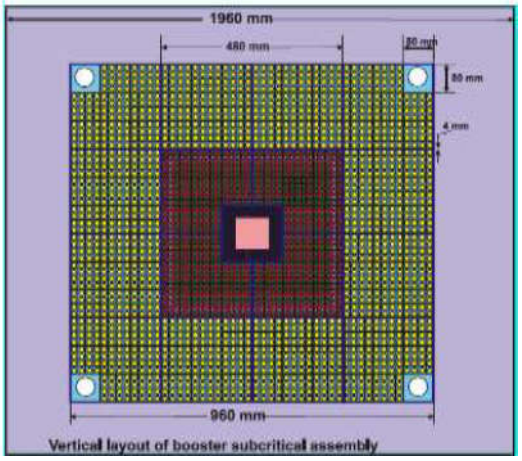

Figure 1. Core layout of "YALINA" assembly

- *Fast neutron zone-I (Umetal=90%),*
- *Fast neutron zone –II (UO_2=36%),*
- *Thermal neutron polyethylene zone,*
- *Graphite*

Figure 2: Core layout of "Yalina" assembly.

The neutron zones consist of different uranium content in fuel elements, and different design for research purpose and is shielded by reflector.

Both fast neutron zones have 132 and 575 fuel rods with 90% and 36 % in content, correspondingly. Intermediate absorber zone has 224 fuel rods, and thermal neutron zone has fuel rods with 7-10% in content. Therefore, the assembly has about 1140-1180 fuel rods in total.

The neutron reflector and intermediate neutron zone are made of graphite and polyethylene with boron. The neutron leakage is reduced by help of reflector and zones and neutron distribution is higher at center of the core.

The pulse operation is suitable for transmutation of long-lived radioactive nuclide in radioactive waste and kinetic characteristics of the system.

6.3. Example 2: Neutron distribution of "UAZSNR" subcritical assembly, Mexico

The total neutron fluence distribution in the middle plane of UAZSNR shown in Fig. 3 can be a representative one for other subassemblies. As shown in Fig. 2, the sharp peak are observed in the center of the core which is decreased 1-2 times in fast neutron zones 2-3 times in intermediate zone, 3-4 times in thermal neutron zone and sudden drop of the flux is occurred in shielding outside the reflector.

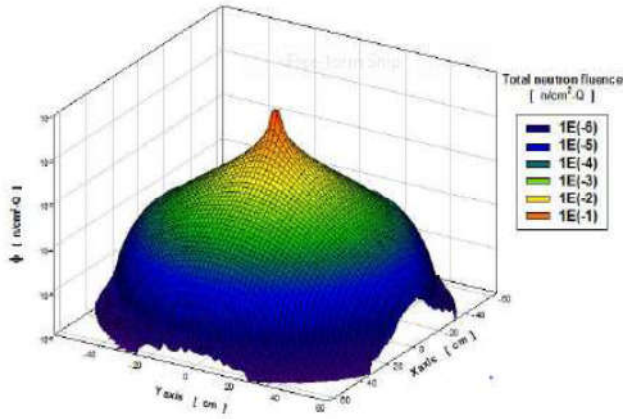

Figure 3: Spatial distribution of neutrons in "UAZSNR" middle plane with 1350 fuel slugs.

7. Application of the subcritical assembly, main research results

a) To study the processes at nuclear reactor in safe and subcritical condition.
- To calculate and measure neutron multiplication and flux depending upon assembly design,
- To calculate and measure the spatial dependence of neutron multiplication factor,
- To determine the fast, intermediate and thermal neutron flux in reactor zones and to study neutron slowing-down.

b) To study on dynamic phenomena of neutron multiplication depending on type of fuel element and moderator.
- To determime pulsed neutron parameters (neutron yield, neutron slowing-down, pulse length) depending on time.

c) To do experiment on fundamental and applied research using fast and thermal neutrons.

d) To use the subcritical assembly for nuclear reactor engineering, nuclear technology and nuclear engineering educational programs.

e) To study on transmutation of long-lived radionuclides in high level radioactive waste.

f) To use for diagnosis and medical treatment.
- To produce radioactive isotopes
- Neutron capture and absorption exposure.

7.1. Example 1: Application on "Yalina" subcritical assembly

In case without-fuel and -absorber (only with neutron source):
- ❑ Neutron background, flux distribution, neutron spectrum and fission rate ratio of ^{235}U / ^{232}Th, ^{235}U / ^{238}U of the subcritical assembly
- ❑ Dependence of neutron distribution direction, location of neutron zones, structure of neutron zones and content of B_4C.
- ❑ Reflector effect on neutron flux and energy at the zones

In case with fuel and absorber:
- ❑ To measure neutron multiplication and critical mass of fuel element in the subcritical assembly
- ❑ To define effective neutron multiplication factor depending on zone shape and dimension determination of neutron flux at $k_{eff} \sim 0.98$
- ❑ To calculate reactivity depending on fuel element

- ❑ To measure the fast and thermal neutron spectra /by fission of ^{232}Th,^{238}U (their threshold energy are 1.2 MeV and 0.9 MeV, respectively) and ^{235}U/
- ❑ To measure radial thermal neutron flux by ^{115}In (n,γ)^{116}In
- ❑ To transmute some actinide nuclides in spent nuclear fuel of nuclear power plant
- ❑ To calculate and measure the threshold reaction rate by thermal and fast neutrons
- ❑ To measure total neutron yield produced at neutron multiplication target
- ❑ To calculate self-shielding effect of boron in polyethylene.

7.2. Example 2: Applications on subcritical assembly of Ukraine

Table 2 lists the medical radioactive isotopes produced at subcritical assembly, Kharkov Institute of Physics and Technology, Ukraine.

Table 2: Medical radioactive isotopes produced at subcritical assembly.

medical radioactive isotopes	Half-life, $T_{1/2}$	nuclear reaction
^{188}Re	17.0 h.	$^{187}Re\ (n,\gamma)$
		$^{102}Pd\ (n,\gamma)$
^{103}Pd	16.9 h.	$^{104}Pd\ (n,2n)$
^{99}Mo	66.0 h.	$^{98}Mo\ (n,\gamma)$
		$^{100}Mo\ (\gamma,n)$
^{99m}Tc	6.06 yrs	$^{235}U\ (n,f)$
^{192}Ir	74.02 yrs	$^{191}Ir\ (n,\gamma)$

Conclusions

1. The structure, working principle of the subcritical assembly and its applications and research fields were discussed in the present paper.
2. It is important to establish and install the subcritical assembly to study the physics processes in nuclear reactor and nuclear reactor operation at safe condition for countries like Mongolia who has no experience to operate nuclear power plant.
3. The broad opportunities of usage of the subcritical assembly to enhance the content and the level of nuclear education program and nuclear research directions was described here.

References

[1] N. Arkhangelskiy, Nuclear Research Facilities in Russia for innovative nuclear development, ROSATOM, IAEA Consultancy Meeting, 10-12 June 2013.
[2] Y. Rugama, J.L. Kloosterman, A.Winkelman, Experimental Results from Noise Measurements in a Source Driven Subcritical Fast Reactor, *Prog. Nucl. Energy* 44: 1-12, 2004.
[3] V.O. Babenko, V.I. Gulik, V.M. Pavlovych, The new research subcritical reactor driven by a high-intensity neutron generator for transmutation of the nuclear waste, *NPAE-2010 – Proceedings*, 509-511, 2010.
[4] H.R. Vega-Carrillo, Subcritical nuclear assembly, *ISSSD-2014 – Proceedings*, 29-41, 2014.
[5] V.V. Gunn, J.S. Hook, A. Dovbnya, et al., Recycling "SALO" – the basis for the establishment of model podkrytycheskoho reactor controlled by accelerator, Visn. Hark. Nat. Univ. Avg. nat. "Nuclei, Particles, Fields", 721, 19-30, 2006.
[6] N. Xoubi, Design, development and installation of Jordan subcritical assembly, *Sci. Tech. Nucl. Inst.,* 197502, 1-5, 2013.
[7] V. Bournos, C.Routkovskaia, I. Serafimovich, et al., Experimental investigations on ADS at sub-critical facilities of Joint Institute for Power and Nuclear Research-SOSNY of the National Academy of Sciences of Belarus, IAEA-RC-1003.1: 24-42, 2005.

ALPHA-CLUSTERING IN (n,α) REACTIONS

B. Batchimeg*, G. Khuukhenkhuu, J. Munkhsaikhan,

Nuclear Research Center, National University of Mongolia, Ulaanbaatar, Mongolia
**E-mail:batchimeg.tr@gmail.com*

Abstract

Alpha-clustering in nuclei has always been one of the important subjects for nuclear structure and reaction study. This effect has been investigated by many authors using the different methods and theoretical approaches for a long time. However, solid theoretical explanation of the α-clustering in nuclei has not formed yet. In this work we estimate α-clustering probabilities and frequencies for slow, intermediate and fast neutrons induced (n, α) reactions using the statistical model and knock-on mechanism.

1. Introduction

From the very beginnings of nuclear physics, it was known that α-particles often emerge in decay processes of heavy nuclei. The fact that α-particles take part in the creation of nuclei and they appear as a result of radioactive decays of nuclei suggests a possibility that α-particle exists inside these nuclei. Therefore the α-particle or the α-cluster, the most stable cluster yet to be known, has been one of the important subjects for contemporary nuclear structure theory [1] and reaction study for a long time. Many attempts to investigate this phenomenon have been made and one of those is the evaluation of the α-cluster formation probability. The α-cluster formation probability or the factor ϕ_α was successfully studied by many scientists using different methods. Bonnetti and Milazzo-Colli [2] found the cluster formation factor using the so called preformed alpha particle model, while Xu et al. [3] studied the clustering probability using the half-lives of some nuclei, obtained by the density dependent cluster model. Zhang, Royer and Li [4,5] obtained the α-particle preformation probability using the semiclassical approach for frequency of the α-cluster motion inside mother nuclei for α-decay of some heavy nuclei. Unfortunately, a consistent and common opinion for theoretical explanation of the α-clustering in nuclei has not been fully formulated thus far. Study of α-cluster formation probability ϕ_α in the *(n,α)* reaction cross sections is of interest for the nuclear energy application and for understanding some basic nuclear physics problems. For instance, it is important to estimate helium production, nuclear heating, transmutations in the structural materials of fission/fusion reactors and useful to clarify the nuclear structure. In this work, we estimate α-clustering probability for resonance, intermediate and fast neutron induced *(n,α)* reactions using the statistical model and knock-on mechanism. In our study, the α-cluster is imagined to moves back and forth inside the nucleus with a certain frequency, and this frequency is considered to be one of the important factors. For this reason, we have also obtained the α-cluster frequency for *(n,α)* reactions. We compared our results with values obtained by other authors.

2. Theoretical bases of study and results

2.1. The resonance neutron induced (n,α) reaction

Using the statistical model and taking into account the α-clustering in the compound nucleus, Weisskopf's formula [6] for the average width of a level can be written in the following form:

$$\langle \Gamma_\alpha(J) \rangle = \frac{D(J)}{2\pi} T_\alpha \phi_\alpha, \tag{1}$$

where *D(J)* is the average level spacing for given J. T_α is the transmission factor of an α particle through the potential barrier of the daughter nucleus. ϕ_α is the α -clustering factor.
From Eq. (1), the α-clustering factor can be found as:

$$\phi_\alpha = 2\pi \frac{\langle \Gamma_\alpha(J) \rangle}{D(J) T_\alpha}. \tag{2}$$

To simplify the calculations, the angular momentum dependence of the transmission factor is neglected in Eq. (2). Then we apply the resulting equation to some isotopes in order to estimate the α-clustering factor for the

(n,α) reaction induced by resonance neutrons, which is shown in Table 1. Experimental data on the average α widths Γ_α(exp) were taken from Ref. [7]. We use the average level spacing for s-resonances from Ref. [8] in our calculation. The transmission factors, T_α, were calculated using Rasmussen's formula [9] for zero angular momentum, $l_\alpha = 0$, of α particles.

Table 1: The α-clustering factors calculated using Eq. (2) for resonance neutrons ($E_n \leq 5$ keV).

Isotopes	Γ_α(exp) [μeV]	D_o[eV]	T_α	ϕ_α
^{64}Zn	12	2940	8.63×10^{-8}	0.30
^{67}Zn	580±340	367	2.75×10^{-5}	0.21
^{95}Mo	26±18	81	1.58×10^{-6}	0.53
^{123}Te	7.3±3.7 (3.0±2.0)*	25.1	2.32×10^{-7}	1.97 (0.81)*
^{143}Nd	21±8	37.6	4.12×10^{-6}	0.37
^{145}Nd	0.32±0.19	17.8	1.41×10^{-7}	0.35
^{147}Sm	2.3±0.6	5.7	4.67×10^{-6}	0.24
^{149}Sm	0.21±0.06	2.2	5.12×10^{-7}	0.52

*Data from [10]

2.2. The intermediate neutron induced (n,α) reaction

In the framework of the statistical model, the average *(n,α)* cross section can be expressed as [11, 12]

$$\langle\sigma(n,\alpha)\rangle = 2\pi^2\left(\frac{\lambda_n}{2\pi}\right)^2 \sum_l \sum_J \frac{g(J)}{D(J)} \frac{\langle\Gamma_n(J,l)\rangle\langle\Gamma_\alpha(J,l)\rangle}{\langle\Gamma(J,l)\rangle} F_l. \quad (3)$$

Here λ_n is the wave length of the incident neutron. $\langle\Gamma_n(J,l)\rangle\langle\Gamma_\alpha(J,l)\rangle$ and $\langle\Gamma(J,l)\rangle$ are the average neutron, alpha and total level widths, respectively. F_l is the level width fluctuation factor comprised within the range of 0.6–1.0.

For the intermediate neutrons, one may usually assume $\Gamma_n \gg \Gamma_\gamma \gg \Gamma_\alpha$, so that the total level width is given by $\langle\Gamma(J,l)\rangle \approx \langle\Gamma_n(J,l)\rangle$ *a*pproximation. In addition, if we neglect the angular momentum and spin dependence of the total (n,α) cross section averaged over the wide neutron energy range, and assume $F_l \approx 1$, one can obtain from Eq. (3) the following simple formula for the *α*-clustering factor

$$\phi_\alpha \approx \frac{\langle\sigma(n,\alpha)\rangle}{\pi\left(\frac{\lambda_n}{2\pi}\right)^2 T_\alpha}. \quad (4)$$

Eq. (4) is then used to estimate the α-clustering factor for 24–30 keV neutron-induced (n,α) reactions, which is shown in Table 2. The experimental data on the (n,α) cross sections were taken from Ref. [7].

Table 2: The α-clustering factors for intermediate neutrons of 24-30 keV.

Target Nuclei	E_n [keV]	$\sigma(n,\alpha)$ [μbarn]	T_α ($l_\alpha = 0$)	ϕ_α
^{95}Mo	30	20±4	1.75 x10^{-6}	0.53
^{123}Te	24	2.8±0.7	2.48 x10^{-7}	0.52
^{143}Nd	30	20±3	4.50 x10^{-6}	0.20
^{147}Sm	30	28±5	5.14 x10^{-6}	0.25

2.3. The fast neutron induced *(n,α)* reaction

2.3.1. Normalization of the theoretical *(n,α)* cross section to experimental data

In the framework of the statistical model, where the compound mechanism of fast neutron induced *(n,α)* reaction cross section can be expressed as follows [13]:

$$\sigma^{th}(n,\alpha) = C\pi(R+\lambda_n)^2 \exp\left(-K\frac{N-Z+0.5}{A}\right). \quad (5)$$

To obtain Eq. (5), we use Weisskopf-Ewing evaporation model [14], constant nuclear temperature approximation [6] and Weizsaker's formula for binding energy [15]. However, as shown in Figure 1, one can see that the theoretical *(n,α)* cross sections calculated by statistical model formulae was higher than the experimental one. We assume these discrepancies in *(n,α)* cross sections are possibly caused by α-clustering effect which was not considered in Eq. (5)

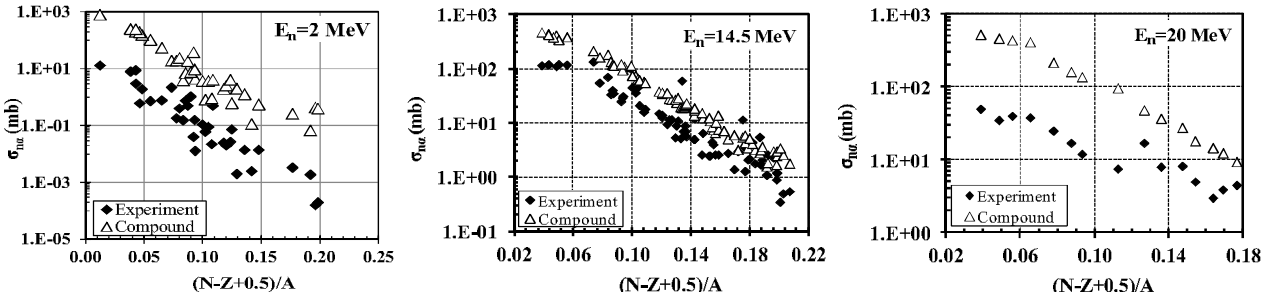

Figure 1: Comparison of experimental data with theoretical (n,α) cross sections at E_n of 2, 14.5 and 20 MeV.

Therefore, if the clustering effect is taken into account in *(n,α)* cross section formula, Eq. (5) can be rewritten in the following form

$$\sigma^{th}(n,\alpha)\cdot\phi_\alpha = C\pi(R+\lambda_n)^2\phi_\alpha \exp\left(-K\frac{N-Z+0.5}{A}\right) = \sigma^{exp}(n,\alpha). \quad (6)$$

From Eq. (6) we can find α-cluster formation probability by ratio of the experimental cross section to theoretical (n,α) one as

$$\phi_\alpha = \frac{\sigma^{exp}(n,\alpha)}{\sigma^{th}(n,\alpha)}. \quad (7)$$

By taking into account the alpha cluster formation probability into the *(n,α)* cross section and normalizing theoretical *(n,α)* cross section to experimental data, we have determined ϕ_α . The result is shown in Figure 2.

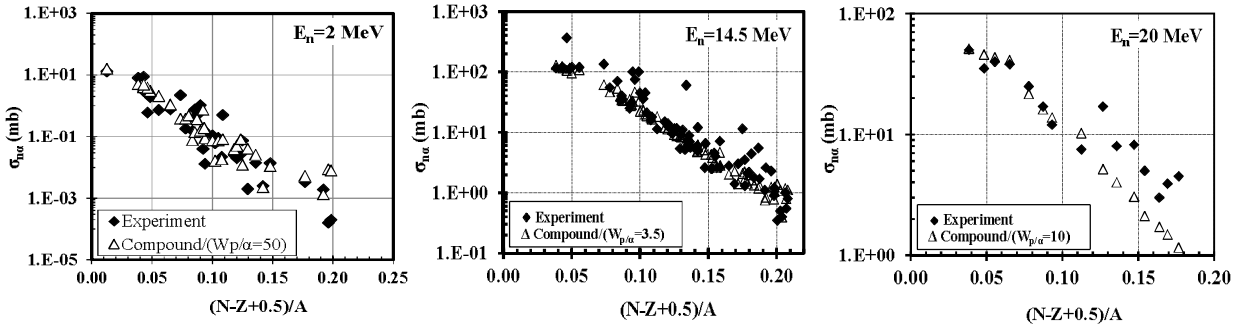

Figure 2: Comparison of theoretical (n,α) cross sections, taking into account of cluster formation probability, with experimental data at neutron energies of 2, 14.5 and 20 MeV.

Some discrepancy in Fig. 2 between theoretical and experimental cross sections at 20MeV for asymmetry parameter *(N-Z+0.5)/A>0.12* is, perhaps, caused by contributions from the pre-equilibrium and direct

mechanisms to the *(n, α)* cross sections. The values of the α-clustering factor ϕ_α obtained by the normalization theoretical to the experimental ones are given in table 3 for neutron energy of 2 to 20 MeV.

Table 3: The α-clustering factor for fast neutrons, calculated in the framework of compound mechanism.

E_n [MeV]	2	4	4.5	5	5.5	6	6.5	8	10	13	14.5	16	18	20
$\langle\phi_\alpha\rangle$	0.02	0.22	0.22	0.25	0.28	0.28	0.28	0.33	0.33	0.33	0.28	0.22	0.18	0.10

2.3.2. Calculation of α-clustering probability using the (n,α) cross sections and total neutron cross sections for the ^{4}He.

The next method we suggest is based on the knock-on mechanism. By analogy of the compound model, we assume the *(n,α)* cross section can be expressed as two stages process

$$\sigma(n,\alpha) = \phi_\alpha \sigma_n^{tot}(^4\mathrm{He}). \quad (8)$$

Here the *(n,α)* cross section can be defined by the multiplication of alpha cluster formation probability on the surface of nuclei and total neutron cross section of ^{4}He.
Thus from Eq. (8) we can find the α-cluster formation factor as

$$\phi_\alpha = \frac{\sigma^{exp}(n,\alpha)}{\sigma_n^{tot}(^4\mathrm{He})}. \quad (9)$$

For the evaluation of the alpha cluster formation factor, the *(n,α)* cross section and total neutron cross section of *^{4}He* data were extracted from the EXFOR [16].
We have calculated the ϕ_α alpha cluster formation probability for a few heavy nuclei depending on the energy range of E_n=4÷6 MeV. The results are shown in Table 4. We note that as the neutron energy increase the *α*-clustering probability is usually increased for the target nuclei.

Table 4: The α-clustering factor of some isotopes, calculated using a method based on knock-on mechanism.

Isotopes	E_n	$\sigma(n,\alpha)$ [mbarn]	$\Delta\sigma(n,\alpha)$ [mbarn]	ϕ_α	$\Delta\phi_\alpha$
^{95}Mo	4	0.700	0.070	2.79 x10^{-4}	2.79 x10^{-5}
	5	1.220	0.120	0.001	5.53 x10^{-5}
	6	1.700	0.170	0.001	8.30 x10^{-5}
^{143}Nd	4	0.120	0.012	4.781 x10^{-5}	4.781 x10^{-6}
	5	0.210	0.021	9.633 x10^{-5}	9.673 x10^{-6}
	6	0.310	0.031	1.512 x10^{-4}	1.513 x10^{-5}
^{147}Sm	5	0.230	0.023	1.055 x10^{-4}	1.059 x10^{-5}
	6	0.290	0.029	1.415 x10^{-4}	1.415 x10^{-5}

2.4. Alpha-clustering frequency in (n,α) reactions

The *α* decay theory was firstly developed in 1928 by G. Gamow and others [17, 18]. It describes the *α* radioactivity as a quantum tunneling through the potential barrier separating the mother nucleus energy and the total energy of the separated α particle and daughter nucleus. Later on, cluster-like [19-21] and fission-like [22–25] theories have been used to explain the *α* emission process.

In the α-cluster model, one of the many attempts of *α*-decay study, the decay constant λ is the product of three terms: the frequency f_α, the barrier penetrability *P* and the α preformation probability ϕ_α. Often the frequency, one of the important factors for alpha cluster and decay study, is calculated supposing that the *α* particle moves classically back and forth inside the nucleus and is even sometimes taken as a constant.

Contrary to this fact, we have assumed that α-particle motion frequency is the motion inside the nucleus and have found that it does depend on the target nuclei threshold energy, the energy that is needed for the formation of α-cluster on the surface of the daughter nuclei.
For the nucleus with the positive threshold energy of α-break up, the α-clusters can't be formed on the surface of the daughter nuclei until a sufficient energy is given from the outside. However from the Heisenberg uncertainty principle, we assume that it is possible for a very brief moment of time Δt enough energy ΔE could be produced in the nuclei, sufficient to form a cluster on a surface of a daughter nuclei. In this case, we assume that the α-particle motion frequency in target isotope with positive threshold energy of α-break up can be calculated by

$$f_\alpha = \frac{\phi_\alpha}{\Delta t}. \quad (10)$$

As for the target isotope with negative threshold energy of α-break up, f_α has been determined using following formula:

$$f_\alpha = \frac{1}{R}\sqrt{\frac{E_\alpha}{2m_\alpha}}. \quad (11)$$

We have found the α-particle motion frequency of a few heavy nucleus for a slow, intermediate and slow neutron induced *(n,α)* reactions, which are shown in a Table 5.

Table 5: The α-particle motion frequency of some isotopes.

Reaction mechanism / Target	Compound			Knock-on
	Resonance (E_n≤5keV)	**Intermediate (E_n=30keV)**	**Fast (E_n=6MeV)**	**Fast (E_n=6MeV)**
^{95}Mo	2.220x10^{21}	2.245 x10^{21}	5.615 x10^{21}	3.402 x10^{18}
^{143}Nd	6.935 x10^{20}	6.989 x10^{20}	1.412 x10^{21}	3.639 x10^{20}
^{147}Sm	7.017 x10^{20}	7.069 x10^{20}	1.407 x10^{21}	7.581 x10^{20}

3. Discussion

The α-clustering factors for *(n,α)* reactions induced by resonance and intermediate neutrons, shown in Tables 1 and 2, vary from 0.20 to 0.53 for all isotopes except for ^{123}Te, which for the new value Γ_α (exp) = 7.3 ± 3.7 μeV gives a not possible α-clustering factor of ϕ_α = 1.97 (value larger than 1). In contrast, the Γ_α (exp) = 3.0 ± 2.0 μeV measured previously in the $^{123}Te(n,\alpha)^{120}Sn$ reaction yields an α–clustering factor of ϕ_α= 0.81. We observe from Tables 1 and 2 that the α-clustering factors for each isotope are almost the same for the resonance and intermediate neutrons. For the fast neutrons, the values obtained in the framework of the statistical model were in a range of ϕ_α=0.02÷0.33, while the results obtained by the knock-out mechanism for a few heavy isotopes were in a range of ϕ_α=4.8x10^{-5} ÷ 0.001. The results we have obtained in current work were close to the values of several authors including Bonetti and Milazzo-Colli[2], S.M. Ahmed [26], S.Q. Guo et al.[27], while they differed from the values calculated by Kadmensky and Furman[28].
From the α-particle motion frequency results, we have observed that the frequency rises as the neutron energy increase. As for the incremental differences between the results for fast neutron induced *(n,α)* reaction, they may have been caused by the different reaction mechanisms. Our results were close to the values of Zhang et al.[4,5]. To obtain more detailed information about α-clusterization further investigations are desired.

4. Conclusions

1. The α-clustering factors for *(n,α)* reactions induced by slow, intermediate and fast neutrons were obtained for some isotopes using the statistical model and knock-on mechanism of nuclear reactions:
   - In the case of resonance neutron, the α-clustering factor varied in the range of ϕ_α=0.21÷0.53. And for intermediate neutron induced *(n,α)* reactions clusters were found in the range of ϕ_α=0.20÷0.53.

- In the case of fast neutron, the α-clustering factor, calculated in the framework of statistical model, varied from ϕ_α=0.02÷0.33 in the region of E_n=2÷20MeV. On the other hand the α-clustering factor obtained using a method based on knock-on mechanism varied from ϕ_α=4.8x10^{-5} ÷ 0.001 for a few heavy isotopes. Our values of the α-clustering factor for slow, intermediate and fast neutrons induced *(n,α)* reactions are satisfactorily in a broad agreement with different evaluations by other authors.

2. The α-clustering frequency for *(n, α)* reactions induced by slow, intermediate and fast neutrons were obtained for some isotopes. From these results, it was observed that the α-clustering frequency increases with the neutron energy. However further investigation has to be done for more detailed information.

References

[1] W.C. Price, S.S. Chissick, *The Uncertainty Principle and Foundations of Quantum Mechanics*, Chapter 23, New York, John Wiley press, 485, 1977.

[2] R. Bonetti, L. Milazzo-Colli, Spontaneous α-decay: A statistical interpretation, *Phys. Lett. B* 49: 17-19, 1974.

[3] C. Xu, Z.Z. Ren, Global calculation of α-decay half-lives with a deformed density-dependent cluster model, *Phys. Rev. C* 74: 014304, 2006.

[4] H.F. Zhang, G. Royer, α particle preformation in heavy nuclei and penetration probability, *Phys. Rev. C* 77: 054318, 2008.

[5] H.F. Zhang, G. Royer, J.Q. Li, Assault frequency and preformation probability of the α emission process, *Phys. Rev. C* 84: 027303, 2011.

[6] J.M. Blatt, V.F. Weisskopf, *Theoretical Nuclear Physics*, New York, Springer-Verlag, 875, 1979.

[7] N.P. Balabanov, V.A. Vtyurin, Yu.M. Gledenov et al., Investigation of Alpha-Widths of compound nuclei, *PEPAN* 21: 317-364, 1990.

[8] S.F. Mughabghab, *Atlas of Neutron Resonances: Resonance parameters and thermal cross sections*, Amsterdam, Elsevier press, 153, 2006.

[9] J.O. Rasmussen, Alpha-decay barrier penetrabilities with an exponential nuclear potential: even-even nuclei, *Phys. Rev.* 113: 1593-1598, 1959.

[10] Yu.P. Popov, The (n,α) Reaction on Resonance Neutrons, *JINR R-3-8140*, Dubna, 1974.

[11] A.M. Lane, J.E. Lynn, Fast neutron capture below 1 MeV : The Cross Sections for ^{238}U and ^{232}Th, *Proc. Phys. Soc. A* 70: 557-570, 1957.

[12] Yu.P. Popov V.I. Salatskii, G. Khuukhenkhuu, Averaged cross sections of (n,α) reactions on ^{147}Sm, ^{143}Nd, ^{149}Sm nuclei induced by 30 keV neutrons, *Sov. J. Nucl. Phys*. 32: 893, 1980.

[13] G. Khuukhenkhuu, Yu.M. Gledenov, M.V. Sedysheva et al., Systematical analysis of (n,α) reaction cross sections for 6-20 MeV neutrons, *Phys. Elem. Part. Atom. Nucl. Lett.* 11: 1159-1168, 2014.

[14] V.F. Weisskopf, D.H. Ewing, On the yield of nuclear reactions with heavy elements, *Phys. Rev.* 57: 472-485, 1940.

[15] C.F. Weizsaker, Zur Theorie der Kernmassen, *Z. Phys.* 96: 431-458, 1935.

[16] http://www-nds.iaea.org/exfor/

[17] G. Gamow, Zur Quantentheorie des Atomkernes, *Z. Phys*. 51: 204-212, 1928.

[18] E. U. Condon, R. W. Gurney, Quantum Mechanics and Radioactive Disintegration, *Nature* 122: 439, 1928.

[19] S.S. Malik, R. K. Gupta, Theory of cluster radioactive decay and of cluster formation in nuclei, *Phys. Rev. C* 39: 1992-2000, 1989.

[20] A. Ludu, A. Sandulescu, W. Greiner, A new large amplitude collective motion in nuclei: Clusters as solitons on the nuclear surface, *Int. J. Mod. Phys. E* 1: 169-200, 1992.

[21] J.C. Pei, F.R. Xu, Z.J. Lin et al., α-decay calculations of heavy and superheavy nuclei using effective mean-field potentials, *Phys. Rev. C* 76: 044326, 2007.

[22] D.N. Poenaru, M. Ivascu, A. Sndulescu et al., Atomic nuclei decay modes by spontaneous emission of heavy ions, *Phys. Rev. C* 32: 572-581, 1985

[23] D.N. Poenaru, I.H. Plonski, W. Greiner, α-decay half-lives of superheavy nuclei, *Phys. Rev. C* 74: 014312, 2006.

[24] G. Royer, Alpha emission and spontaneous fission through quasi-molecular shapes, *J. Phys. G*: *Nucl. Part. Phys.* 26: 1149-1170, 2000.

[25] P. R. Chowdhury, C. Samanta, D.N. Basu, α decay half-lives of new superheavy elements, *Phys. Rev. C* 73: 014612, 2006.

[26] V.Yu. Denisov, A.A. Khudenko, α–decay half-life, α–capture, and α–nucleus potential, *At. Data Nucl. Data Tables* 95: 815-835, 2009.

[27] S.M. Saleh Ahmed, Alpha-cluster preformation factor within cluster-formation model for odd-a and odd–odd heavy nuclei, *Nucl. Phys. A* 962, 103-121, 2017. (Submitted)

[28] S.Q. Guo, X. Bao, Y. Gao et al., The nuclear deformation and preformation factor in the α-decay of heavy and superheavy nuclei, *Nucl. Phys. A* 934: 110-120, 2015.

[29] S.G. Kadmensky, V.I. Furman, α-decay of spherical nuclei, *PEPAN* 6: 469-514, 1975.

ELEMENTAL AND MOLECULAR IMAGING WITH X-RAYS FOR BIOMEDICAL APPLICATIONS: CALCIUM MAPPING IN HUMAN HAIR FOR POSSIBLE EARLY DETECTION OF BREAST CANCER

A. Ito

Tokai University, 4-1-1 Kitakaname, Hiratsuka, Kanagawa 259-1292
E-mail: aeito@keyaki.cc.u-tokai.ac.jp

Abstract

X-ray fluorescence mapping and soft X-ray microscopy have been applied to obtain Ca and oxidative damage distributions in female hair from breast cancer patients, in expecting the early detection of breast cancer, based on an interesting study by Chikawa et al. on Ca increase in advance to the development of breast cancer. Ca increase in the central part of hair, medulla, was suggested to result from Ca content in blood, while hair oxidative damage mainly increases Ca content in the outer areas, cuticle and cortex. From these results, Ca measurement in medulla may be effective for the detection of early breast cancer. In addition, for the purpose of breast cancer screening, a laboratory type apparatus for X-ray fluorescence analysis using microbeam X-rays from a hair root to a tip is applicable to the identification of the position with extensive accumulation of Ca in medulla.

1. Introduction

One of the unique characteristics of X-ray imaging is the mapping of constituent elements and molecules at high spatial resolution [1]. For elemental mapping, X-ray fluorescence imaging, the resolution of which is determined by the size of irradiated microbeam X-rays, has been widely used, while for molecular mapping, spectromicroscopy, where images are captured at X-ray energies corresponding to molecular or chemical bond specific resonance peaks in NEXAFS (Near Edge X-ray Absorption Fine Structure), has attracted much attention in chemical and biological fields [2-6]. We have been applying X-ray spectromicroscopy and X-ray fluorescence imaging to biomedical specimens such as chromosomes [7], mammalian cells [8, 9] and human tissues [10].

Our recent interest is in the application of Ca distribution in human hair in hoping to provide the very early diagnostic method of breast cancer, based on an interesting finding where Ca content in hair of patients suffering from breast cancer was increased around one year in advance of cancer development by using X-ray fluorescence analysis, in spite of returning to the normal Ca level at the time of diagnosis of breast cancer [11]. Since human hair root has elemental information in blood circulating around it and grows about 1cm per month, it is expected that the hair position with a certain distance from the hair root has the elemental information that the position had at the hair root in the past. For example, the position of 10cm from a hair root has elemental information of blood about 10 months ago. In other words, human hair works as a memory tissue to hold past elemental contents.

However since many factors affect Ca content in human hair such as oxidative damage [12], we measured detailed distribution of Ca in the cross-section samples of hair using X-ray fluorescence mapping, and suggested that hair Ca originated from Ca in blood circulated at the site of hair root is preferentially accumulated in medulla, a central part of hair [13]. Based on these preceding studies, we constructed a high-resolution X-ray imaging system for Ca distribution in addition to oxidative damage mapping of cross-section samples of human hair [10]. In this report, we summarize a measurement procedure for Ca and oxidative damage by combining several X-ray imaging methods, and present recent results obtained for hair specimens kindly supplied from breast cancer patients and from healthy females in collaboration with Tokai University Hospital.

2. Procedure of X-ray analysis of hair

Human hair specimens were obtained from breast cancer patients and from normal females for medical examination who visited Department of Breast and Endocrine Surgery, Tokai University Hospital.

X-ray analyses for the content and distribution of Ca and for the distribution of oxidative damage were conducted as the following steps:

1) Measurement of Ca content from hair root to tip:

X-ray fluorescence analysis using polychromatic X-ray microbeam with a diameter of 0.1mm is carried out every 1 or 3 cm from hair root to tip using X-ray analytical microscope (XGT2700, HORIBA Ltd.). Since the diameter of human hair is about 0.1mm, the microbeam can just cover hair thickness. The most critical feature of XGT2700 is that it fits usual laboratory in its size, which may enable efficient screening of Ca contents in hair from root to tip to survey abnormal Ca content. We call this apparatus laboratory type XRF(X-ray Fluorescence) in this report. At the positions of concern, the hair is cut with a thickness of about 20 μm using a slicer (HS-1, JASCO Corp., Japan) to proceed to the examination of Ca and oxidative damage distribution in hair cross section.

2) Ca mapping of hair cross section:

We employed two types of devices to measure local Ca content with X-ray fluorescence analysis similar to the above-mentioned XGT2700, but the microbeam sizes to scan a sample are much smaller in the range of a few microns to obtain a fine map of Ca in a hair cross section. One device uses monochromatic X-ray excitation which is installed at synchrotron radiation facility, beamline BL-4A of Photon Factory, Tsukuba, Japan. It provides X-ray microbeam with 4-5 μm diameter. We abbreviate this method as SR-μ-XRF (Synchrotron Radiation micro X-ray Fluorescence). Another one, termed PIXE (Particle Induced X-ray Emission), uses proton excitation in this experiment which is installed at National Institute of Radiological Science, Chiba, Japan. It provides proton microbeam with 2 μm diameter.

3) Mapping of oxidative damage of hair cross section:

Since hair is composed of sulfur rich proteins containing cystine, we measure the distribution of cysteic acid, an oxidation product of cysteine, as an index of hair oxidation. Using the difference in NEXAFS profiles of cystine and cysteic acid at the sulfur K absorption edge [14], we obtained the distributions of both compounds in human hair with X-ray contact microscopy in combination with an electronic zooming tube as a two dimensional detector [10], which is set up at beamline BL-11B, Photon Factory every beam time. It provides about 0.5μm spatial resolution. If we take images at the Ca-K absorption edge, Ca map can also be obtained with higher resolution than the X-ray fluorescence method, although the sensitivity is considerably lower than that method.

In Figure 1 typical images of hair cross sections on Ca and oxidative damage distributions are listed for normal and bleached hair specimens. Bleached hair had significant oxidation in cuticle (surface of hair) and cortex (inner part of hair) in contrast to normal hair (the 2nd column). Ca increase seems to be closely correlated with oxidative damage as seen from images of bleached hair (lower row). Considering that Ca accumulation in medulla was observed in normal hair, Ca content in medulla may not depend on external oxidative damage. These results suggest that Ca content in medulla reflect that in blood.

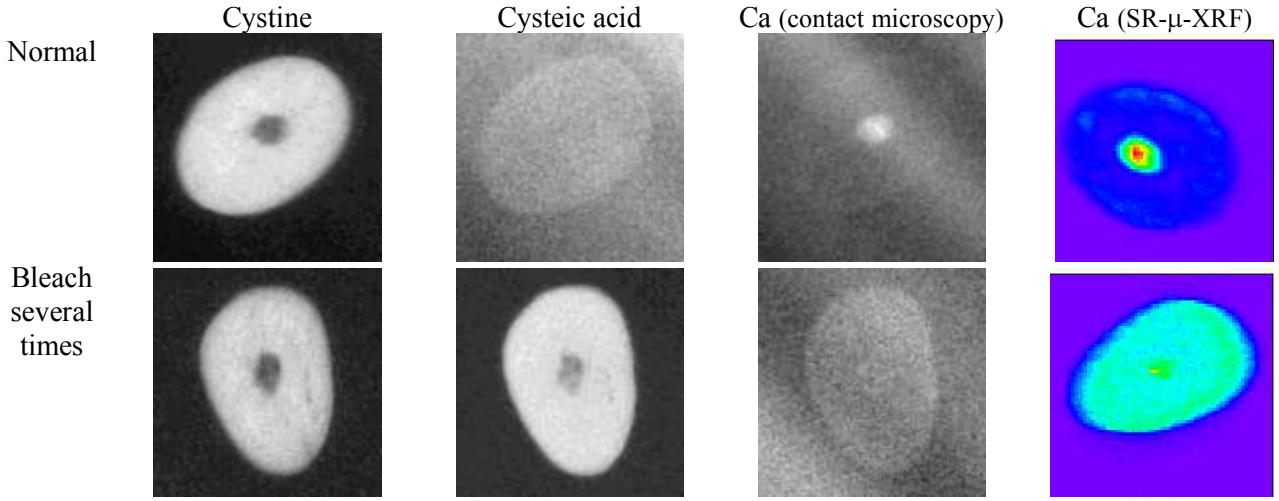

Figure 1: Distributions of oxidative damage (cysteic acid) and Ca in a cross section of human hair. Ca maps are obtained with two methods, contact microscopy and SR-μ-XRF. Maps by SR-μ-XRF are displayed with rainbow pseudo color. Upper row images are from normal hair without any experience of bleach or perm treatment. Lower row images are from hair with bleach treatment of several times.

Using these X-ray analytical and imaging systems, our main interests are as follows:

1) Possible different change of Ca content from hair root to tip using laboratory type XRF in hair specimens of normal females and breast cancer patients

2) The correlation between abnormal Ca content found by XGT2700 and Ca distribution in medulla measured by SR-μ-XRF, PIXE and X-ray contact microscopy.

3. Typical results for hair specimens from breast cancer patients and normal females

Although we have surveyed a few tens of hair specimens, we present here typical examples from both groups, cancer patients and normal females, to demonstrate the effectiveness of our X-ray analytical procedure.

3.1. Laboratory type XRF for Ca distribution from hair root to tip

Figure 2 plotted Ca content against distance from hair root measured by laboratory type XRF. The Ca content was normalized by S content to correct hair thickness. Ca content from a breast cancer patient tends to have larger variation depending on the distance from hair root compared with that from a normal female. Ca and oxidative damage distributions were examined at 25cm and 35cm in the hair from a cancer patient, and at 21cm in the hair from a normal female, respectively.

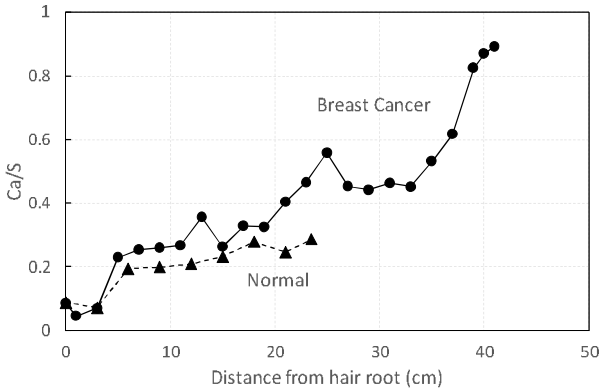

Figure 2: Ca content as a function of distance from hair root measured by laboratory type XRF. Ca content was normalized by S content to correct hair thickness. bold line: hair from a breast cancer patient, broken line: hair from normal female.

3.2. SR-μ-XRF, PIXE and contact microscopy for Ca imaging of hair cross section

Figure 3 shows Ca maps with three different imaging methods. XRF was found to be more sensitive than contact microscopy, although the resolution is lower. Images of PIXE were highly resolved compared with SR-μ-XRF.

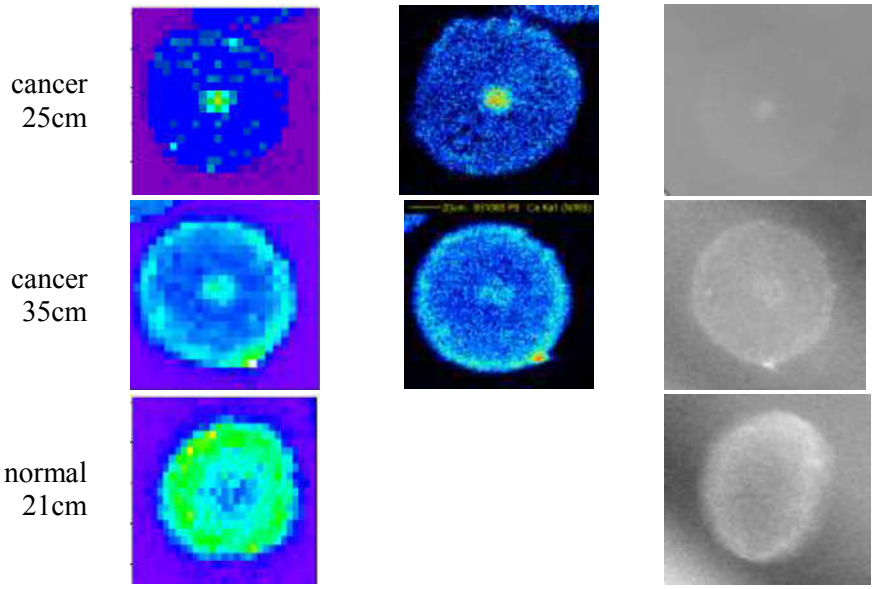

Figure 3: Ca mapping by three methods for hair cross sections from breast cancer patient and normal female. 1st column: Distance from hair root, 2nd column: SR-μ-XRF, 3rd column: PIXE, 4th column: Contact microscopy

Interestingly at the hair position, 25 cm, that gives a maximum Ca/S value in hair from a cancer patient, Ca seems to be accumulated significantly in medulla. At 35 cm Ca accumulation in cuticle area becomes

evident. On the other hand, normal hair had little Ca accumulation in medulla, although Ca was observed in cuticle and cortex. These findings suggest that Ca increase found by laboratory XRF reflects Ca accumulation in medulla. This may lead to a screening procedure to survey Ca accumulation in medulla by using laboratory XRF.

3.3. Contact microscopy for oxidative damage imaging of hair cross section

Cysteic acid maps, an index of hair oxidative damage, were shown in Figure 4 for the same positions as those in Figure 3. Furthermore the degree of oxidative damage was estimated for three areas in hair cross section, cuticle, cortex and medulla, as shown in the panel c. It was found that the degree of oxidative damage was increased monotonously with the distance from hair root in contrast to Ca accumulation in medulla, which suggests that Ca increase in medulla is not correlated with oxidative damage.

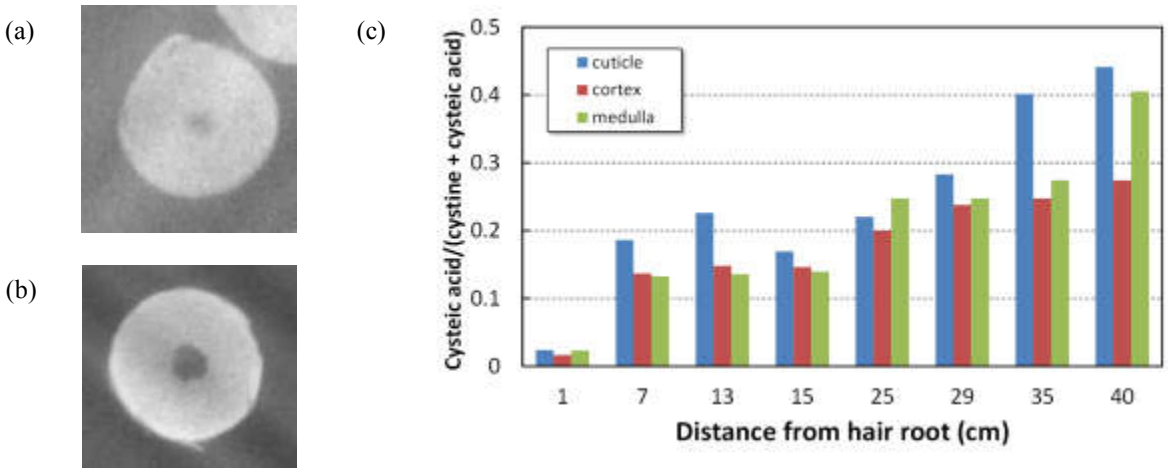

Figure 4: Oxidative damage in hair cross section from breast cancer patient. (a) Oxidative damage map at 25cm position, (b) Oxidative damage mat at 35cm, (c) Oxidative damage distributions at three areas of hair cross section.

4. Summary

1) In order to examine the correlation between Ca distribution in human hair and the incidence of breast cancer, various X-ray analytical systems are employed including XRF and X-ray contact microscopy to detect Ca and oxidative damage distributions.
2) Every hair suffers oxidative damage accompanied with Ca accumulation particularly in the outer area, cuticle, depending on the position from hair root to hair tip.
3) For hair samples from breast cancer patients, Ca seems to accumulate significantly in medulla at certain positions from hair root, in addition to the monotonous Ca accumulation in cuticle. The accumulation in medulla may be detected by a laboratory type XRF apparatus, which is expected as a possible future screening of early development of breast cancer.

Acknowledgements

The work was performed at the Photon Factory under the application number 2014G709 and 2016G543. The author thanks collaborators and students, Dr. K. Shinohara, Mr. T. Ariyama, Mr. F. Ouchi, Mr. M. Torigata at School of Engineering, Tokai University, Prof. Y. Tokuda, Dr. R. Oshitanai, Dr. K. Yokoyama and Prof. N. Niikura at School of Medicine, Tokai University, and Dr. T. Ohigashi at UVSOR Synchrotron facility, Institute for Molecular Science. The author also would like to thank the Photon Factory staff, Dr. Y. Kitajima and Dr. A. Iida. This work was partly supported by the Japan Society for the Promotion of Science (JSPS) KAKENHI, Grant-in-Aid for Scientific Research (C) (16K05021).

References

[1] J. Kirz, C. Jacobsen, M. Howells, Soft X-ray microscopes and their biological applications, *Q. Rev. Biophys.* 28: 33-130, 1995.

[2] H. Ade, X. Zhang, S. Cameron et al., Chemical contrast in X-ray microsocpy and spatially resolved XANES spectroscopy of organic specimens, *Science* 258: 972-975, 1992.

[3] X. Zhang, R. Balhorn, J. Mazrimas et al., Mapping and measuring DNA to protein ratios in mammalian sperm head by XANES imaging, *J. Struct. Biol.* 116: 335-344, 1996.

[4] A.P. Hitchcock, Soft X-ray spectromicroscopy of polymers and biopolymer interfaces, *J. Synchrotron Radiat.* 8: 66-71, 2001.

[5] J.R. Lawrence, G.D.W. Swerhone, G.G. Leppard et al., Scanning transmission X-ray, laser scanning, and transmission electron microscopy mapping of the exopolymeric matrix of microbial films, *Appl. Environ. Microbiol.* 69: 5543-5554, 2003.

[6] Z. Yangquanwei, S. Neethirajan, C. Karunakaran, Cytogentic analysis of quinoa chromosomes using nanoscale imaging and spectroscopy techniques, *Nanoscale Res. Lett.* 8: 1-7, 2013.

[7] K. Shinohara, T. Ohigashi, S. Toné et al., Quantitative analysis of mammalian chromosome by scanning transmission soft X-ray microscopy, *Ultramicroscopy* 194: 1-6, 2018.

[8] A. Ito, K. Shinohara, Y. Mizukami et al., X-ray contact microscopy system for spectromicroscopy of biological specimens, *J. Synchrotron Radiat*. 5: 1099-1101, 1998.

[9] K. Shinohara, A. Ito, T. Ohigashi et al., Discrimination of DNA and RNA distribution in a mammalian cell by scanning transmission soft X-ray microscopy, *J. X-Ray Sci. Technol.* 26: 877-884, 2018.

[10] T. Inoue, K. Takehara, N. Shimizu et al., Application of XANES profiles to X-ray spectromicroscopy for biomedical specimens: Part II. Mapping oxidation state of cysteine in human hair, *J. X-Ray Sci. Technol.* 19: 313-320, 2011.

[11] J. Chikawa, K. Yamada, T. Akimoto et al., The universal concentrations and cancer signs of trace elements in hair observed by X-ray fluorescence analysis, *J. X-Ray Sci. Technol.* 15: 109-129, 2007.

[12] K.E. Smart, M. Kilburn, M. Schroeder et al., Copper and calcium uptake in colored hair, *J. Cosmet. Sci.* 60: 337-345, 2009.

[13] A. Ito, T. Inoue, T. Kawai et al., Difference in the distributions between Ca content and the degree of oxidative damage in human hair determined by x-ray imaging, *AIP Conf. Proc.* 1696: 020021, 2016.

[14] A. Ito, T. Inoue, K. Takehara et al., Application of XANES profiles to X-ray spectromicroscopy for biomedical specimens: Part I. Discrimination of macromolecules with sulfur atoms, *J. X-Ray Sci. Technol.* 19: 249-260, 2011.

FINE STRUCTURES OF EUKARYOTIC CHROMOSOMES

Y. Kinjo

Tokai University, 4-1-1 Kitakaname, Hiratsuka, Kanagawa 259-1292, Japan

Abstract

The manner on the organization of chromosome/chromatin has long been one of the most important subjects of debate in chromosome research. To clarify the organization of a chromosome, we have long observed fine structures of chromosomes/chromatin prepared by surface spreading technique using various types of microscopies and cells. The results showed that globules with 30-120 nm in diameter composed of multiple nucleosomes are interconnected to generate chromatin fibers with heterogeneous thicknesses, suggesting that the basic structure of chromatin is different from the textbook view where a nucleosome fiber regularly coils or folds to generate a 30 nm-wide chromatin fiber.

1. Introduction

Since the discovery of chromosome by Nageli in 1842 [1], it has widely been found in eukaryotic cells and recognized later as a highly condensed structure of genetic substance composed of DNA and proteins. In addition to the importance of its number per cell and shapes as indicators of evolution, biological classification, clinical diagnosis and agriculture, much attention has been paid to the manner how double stranded DNA together with intranuclear proteins is packed and organized into a mitotic chromosome. To visualize its fine structures, electron microscope (EM) has played a great role since 1960s and numerous observations on interphase nuclei and mitotic chromosomes have been made by EM. Especially in 1974 and 1975, "beads on a string" structure was found in nuclease-digested interphase chromatin [2-4]. The structure, well known today as nucleosome fiber, was recognized later as the most basic fibrous structure of a chromosome where double stranded DNA is wrapped around octamers of four types of core histone proteins. The next stage of the investigation went on to the higher order forms of the fiber. In 1976, Finch and Clug proposed the 'solenoid' model where 11 nm wide nucleosome fiber regularly coils into 30 nm-wide chromatin fiber based on EM observation [5]. Although this 'solenoid model' was replaced with the lately emerged 'zigzag model [6]' in current textbooks, zigzag model was also a kind of regular 30nm fiber model and has long been supported and adopted in textbooks since then as the intermediate structure next to the nucleosome fiber [7-10]. Aside from regular 30 nm fibers, the existence of fibers formed by discontinuous globular clusters of nucleosomes (superbeads) was shown by EM observation [11-12]. However, the structure was not necessarily recognized as the universal higher–order structure of the nucleosome fiber *in vivo* due to the failure to find it ubiquitously [13].

Recently, a striking model where no 30 nm fiber exist both in interphase chromatin and metaphase chromosomes was proposed based on cryo-electron microscopic observation, electron spectroscopic imaging and low angle X-ray scattering analyses [14-15]. According to this model, nucleosome fibers are loosely organized by nucleosome-nucleosome interaction into globular structure called "chromatin domains" in interphase nuclei.

These domains are further assembled by 'scaffold' proteins of a chromosome including condensin and topoisomerase II, and finally organized into a mitotic chromosome. Similar evidence of such domains, namely, "clutches" proving the existence of globular clusters have recently been reported [16].

The authors have long observed fine structures of interphase chromatin and mitotic chromosomes of several cell types by various microscopies including EM, X-ray microscopy (XRM) and atomic force microscopy (AFM) using mainly "surface-spreading technique" as a specimen preparation technique. Especially by contact XRM, we succeeded for the first time in observing the fine structures of interphase chromatin and mitotic chromosomes in an aqueous environment [17]. The results including XRM data suggested that chromatin fibers having heterogeneous thicknesses are basically organized with tandemly aligned and interconnected globules composed of multiple nucleosomes [17-19].

In this article, our data obtained by various microscopic techniques mentioned above will be introduced and discussions will be made on the relationship between images of chromosomes/chromatin and specimen preparation techniques.

2. Materials and Methods

The experimental details were already described elsewhere [17-20] and is briefly described here as follows.
[Specimen preparation]

Cultured mouse lymphoma cell line (L5178Y), isolated rat thymocytes, cultured human B lymphocyte cell line (RPMI 1788), or cultured human multiple myeloma cell line (IM 9) were used as chromosomes/chromatin sources. The cultured cells lines arrested in mitotic phase by the treatment with 50 ng/ml colcemid for 5 hours or isolated rat thymocytes were precipitated after centrifugation at 1000 rpm for 5 min and placed onto a clean water surface. At the moment the cells burst by surface tension shock and intracellular materials containing chromosomes/chromatin were spread across the water surface as a thin film. The film was picked up with some substrate such as an EM specimen grid covered with a carbon evaporated film, a thin (about 400 nm in thickness) layer of X-ray resist (polymethyl methacrylate ; PMMA) supported by a silicon substrate or a silicon substrate alone.

For observation of the specimen in an aqueous condition, the substrate with attached chromosomes/chromatin was placed in a hydrated chamber (for X-ray contact microscopy; Fig.1) or in a wet cell (for AFM). In the case for observation in a dried condition, the substrate with the specimen was air-dried with or without fixation with Carnoy fixative (3:1 mixture of 100% methanol and glacial acetic acid).

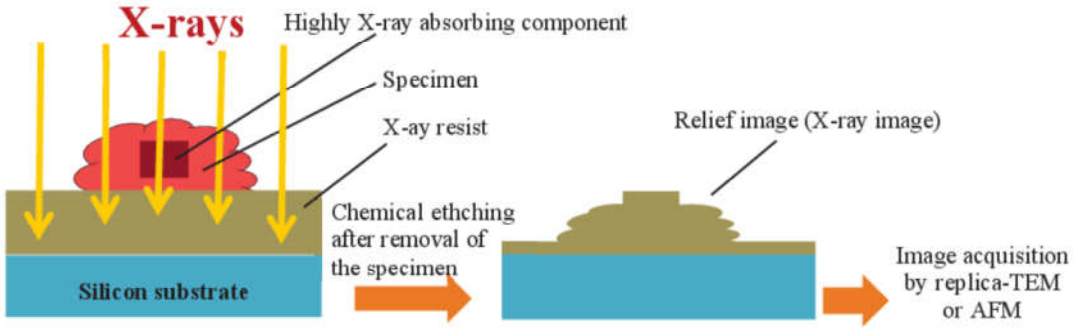

Fugure 1: Principle of X-ray contact microscopy.

[X-ray contact microscopy]
The resist with the specimen was placed in a specimen chamber and exposed to synchrotron X-rays at the wavelength of 2.98 nm or laser produced plasma X-rays (Fig.2). After exposure, the resist with the specimen was washed with 0.5% sodium hypochlorite solution to remove the specimen and etched with the mixture of methylisobutyl ketone and isopropanol to obtain an X-ray image.

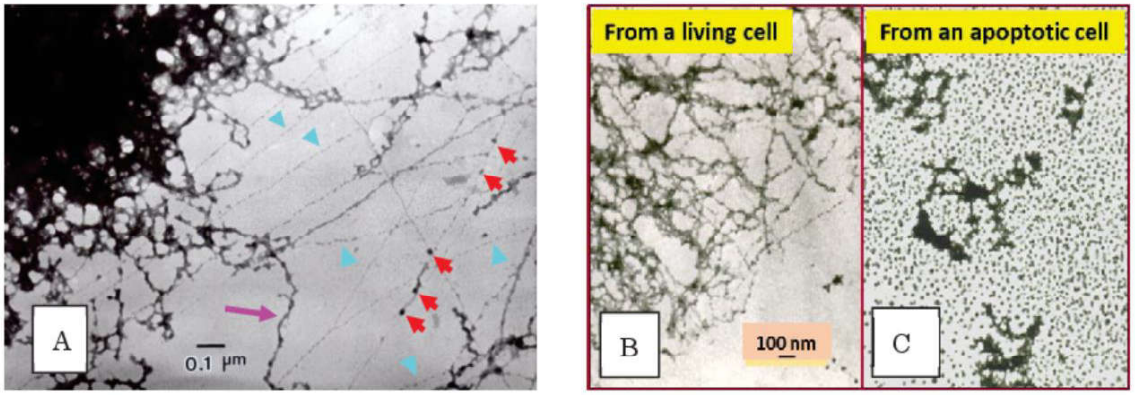

Figure 2: TEM image of chromatin from L5178Y cells (A), unirradiated (B) and γ-irradiated (C) rat thymocytes [21]. Note that globules larger than nucleosome size (ca. 11 nm in diameter) are seen in each picture.

[Image acquisition]
The X-ray images were readout earlier by TEM through replica films created by plasma-polymerization replica method [20] after etching the substrate and later directly by AFM without creation of replica films.

[Observation of specimens solely by AFM]
Either dried or hydrated specimens attached on substrates were directly observed by AFM (SPF 3700, SII Nanotechnologies, Japan) at a spring constant of 20N/m.

3. Results and Discussion

[TEM images]
Figure 2 shows images of chromatin from L5178Y cells (left image; A) and rat thymocytes (right images; B,C). For the image A, fibers of various unraveling extent including nucleosome fiber (arrowheads), nucleosome fiber partially having globules larger than nucleosomes (short arrows), and thicker and knobby fibers (long arrow) emanated from the condensed fiber region are seen.

Images B and C show chromatin from unirradiated- and gamma-irradiated rat thymocytes, respectively. In the image B, typical network of interphase chromatin is seen. On the other hand, such network is seen disrupted and numerous particles with the sizes 10-40 nm in diameter around fragmented and condensed chromatin are seen in the image C. These particles were judged as nucleosomes and their oligomers by simultaneously performed gel electrophoretic analyses [21].

[X-ray images by replica/TEM method]
Figure 3 (A) shows a X-ray image of dried mitotic chromosomes observed by a differential interference microscope (DIC: a kind of light microscope). Typical X- or V-shaped chromosomes are clearly discernible on this relief image. B and C are replica images of a mitotic chromosome and stretched chromatin fiber(s) observed by TEM, respectively. Knobby appearance of the fiber (s) including globular structures are evident especially in C.

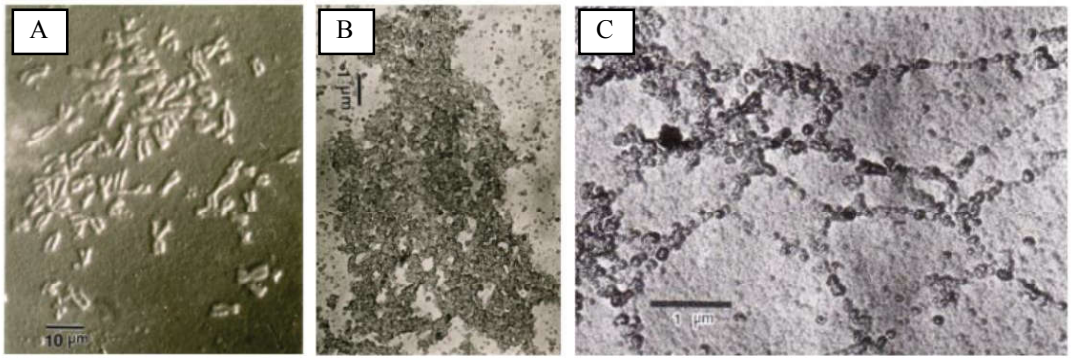

Figure 3: X-ray images of a group of mitotic chromosomes (A; DIC image), single mitotic chromosome (B; Replica/TEM image) and stretched chromatin fibers (C; Replica/TEM image) [18]. Especially in B, fibrous chromatin network composed of interconnected globules are evident. The specimens were all air-dried.

Figure 4 shows images of single mitotic chromosome (A) in an aqueous condition without any chemical fixation and its partially magnified view in the rectangle in A (B). The gross morphology of the chromosome seems to some extent to be disrupted presumably due to high pressure given during placing the specimen in a hydrated chamber.

However, portions which is considered tightly attached to the resist surface seems to keep their radical structure. Especially in the magnified view (B), spherical globules composed of nucleosome-sized particles can be seen.

Although high resolution imaging was expected for TEM observation, there existed one technical difficulty in the replica/TEM method. The difficulty was that ‘good’ images once marked by light microscopic observation were often lost by fragmentation of a replica film during removal of the film from the resist surface on a water surface. To circumvent this problem, observation by AFM of resist surfaces directly without creating replica films were tried.

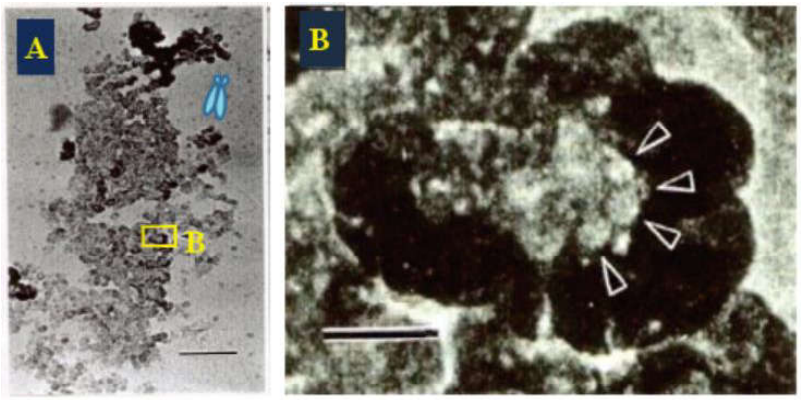

Figure 4: Replica/TEM X-ray images of a mitotic chromosome (A) [17]. Note assembled globules composed of nucleosome-sized particles in the magnified image (B). Bars indicate 1 μm (A) and 100 nm (B), respectively.

[X-ray images by AFM]
Figure 5 shows an image viewed by AFM of interphase chromatin also in an aqueous condition without fixative. Note the knobby appearance of the fiber (s) with various sizes of globules [22].

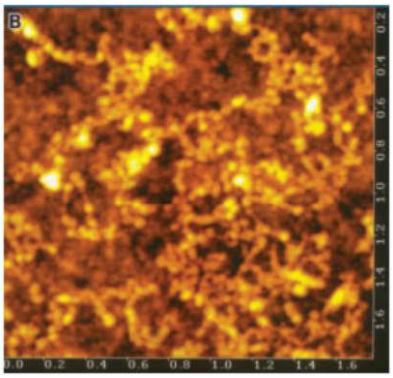

Figure 5: An X-ray image of interphase chromatin in an aqueous condition without any chemical treatment observed by AFM [22].

[AFM observation of mitotic chromosomes at different unravelling level]
Figure 6 shows AFM images of a mitotic chromosome (A) and its partially magnified view (B) in the rectangle in A prepared according to the standard light microscopic protocol, e.g. hypotonic treatment of cells with 75mM $CaCl_2$ or 0.6% sodium citrate followed by fixation with Carnoy fixative, deposition onto a substrate and air-drying.

Typical X-shaped morphology of a mitotic chromosome (A) and its globular surface (B) are clearly discernible in these images.

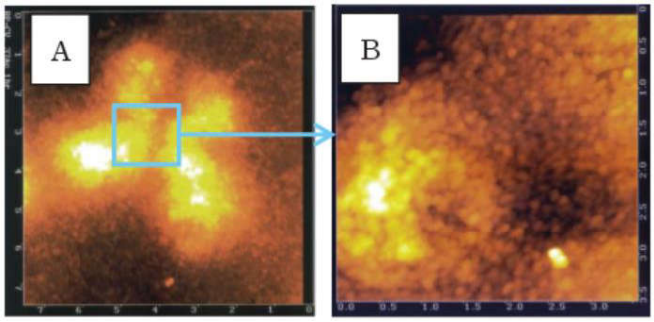

Figure 6: An AFM view of a mitotic chromosome (A) prepared by conventional light microscopic protocol and its partially magnified view (B).

On the other hand in Fig. 7, shown are single mitotic chromosome (A) prepared by surface spreading technique following hypotonic pretreatment with 75 mM KCl and fiber loops radially emanating from the central axis (B,C). In each loop, different sizes of globules with the sizes 40-120 nm in diameter are seen

aligned in tandem. A similar image had been taken in the past (Earnshaw & Laemmli, 1983) [23] by electron microscopic observation. In that case, however, globules on fiber loops were further unraveled into single nucleosomes presumably due to difference in specimen preparation protocol. This difference also suggests that that there exist globular structure higher than nucleosome level in chromatin.

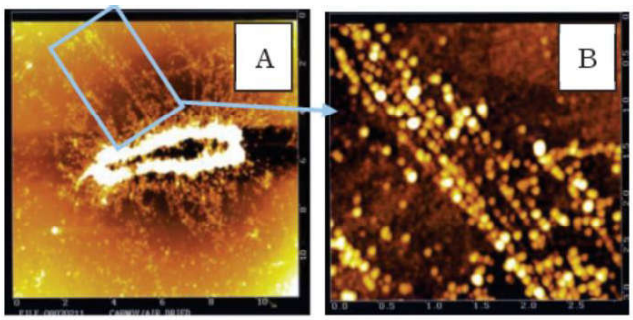

Figure 7: An AFM view of a surface-spread mitotic chromosome (A) and its partially magnified view (B). Clearly shown is that tandemly interconnected 40-120 nm wide globules form fibrous structure (B).

Chromatin/chromosomes are structurally quite unstable and their appearances are affected by various physicochemical factors such as ionic environment, temperature, humidity (wet or dry) and chemical treatments necessary for specimen preparation and observation. As a result, these factors may often play as artefacts for images obtained. In other words, there is no confidence that what we see under some microscope after various preparative processes are their real natural figures in vivo.

Among various types of specimen preparation techniques, the method we adopted was surface-spreading technique developed by J. Gall [24]. The technique is considered today of course fairly harsh for specimens to keep their radical morphology presumably due to strong surface tension shock given at the moment when cells burst and ionic environment far different from physiological condition. However as shown in the data, the technique enables one to observe various hierarchical structures of chromosomes/chromatin emanated from the dense central region to the well dispersed periphery such as naked DNA, nucleosome fiber, globules larger than nucleosomes, fibers thicker than nucleosome fibers composed of the globules and so on. In addition, their fine structures are assumed to keep to some extent their natural structures considering that specimens were attached to substrates just after spreading on water surfaces.

To clarify whether the above assumption is correct or not, it is necessary to observe chromosomes/chromatin in situ along the cell cycle progress where whole processes of unravelling and compaction of chromosomes/chromatin take place. X-ray microscopy is expected as one of candidates capable of accomplishing this aim.

Acknowledgements

The data used here are cited from articles made by collaborative works. Special thanks to Drs. M. Watanabe, K. Shinohara, T. Yamada, H. Ohyama, K. Yada, M. Richardson, Tanaka, A. Ito, H. Nakano, H. Daido and H. Fiedorowicz.

References

[1] Chromosome, *http://www.newworldencyclopedia.org/entry/Chromosome*
[2] A.L. Olins, D.E. Olins, Spheroid chromatin units (v bodies), *Science* 183: 330-332, 1974.
[3] R.D. Kornberg, Chromatin structure: a repeating unit of histones and DNA, *Science* 184: 868-871, 1974.
[4] P. Oudet, M. Gross-Bellard, P. Chambon, *Electron microscopic and biochemical evidence that chromatin structure is a repeating unit, Cell* 4: 281-300, 1975.
[5] J.T. Finch, A. Klug, Solenoidal Model for Superstructure in Chromatin, *Proc. Natl. Acad. USA* 73: 1897-1901, 1976.
[6] J. Bednar, R.A. Horowitz, S.A. Grigoryev et al., Nucleosomes, linker DNA, and linker histone form a unique structural motif that directs the higher-order folding and compaction of chromatin, *Proc. Natl. Acad. Sci. USA* 95: 14173-14178, 1998.
[7-10] B. Alberts, J. Alexander, L. Julian et al. ed., *Molecular Biology of the Cell (Garland Science)*, 3rd-6th Eds., 1994-2016.

[11] H. Zentgraf, W. Franke, Differences of supranucleosomal organization in different kinds of chromatin, *J. Cell Sci.* 99: 272-286, 1984.
[12] M. Watanabe, Y. Kinjo, K. Shinohara, *Observation of human chromosomes by X-ray microscopy in comparison with electron microscopy, X-ray Microscopy in Biology and Medicine,* ed. by K. Shinohara et al., Japan Sci. Soc. Press, Tokyo/Springer-Verlag, Berlin, 295-304, 1990.
[13] A. Wolffe, *CHROMATIN-Structure & Function,* 2nd Ed. Academic Press, 1995.
[14] M. Eltsov, K.M. Maclellan, K. Maeshima et al., Analysis of cryo-electron microscopy images does not support the existence of 30-nm chromatin fibers in mitotic chromosomes in situ, *Proc. Natl. Acad. Sci. USA* 105:19732-19737, 2008.
[15] Y. Joti, T. Hikita, Y. Nishino et al., Chromosomes without 30-nm chromatin fiber, *Nucleus* 3: 404-410, 2012.
[16] M.A. Ricci, C. Manzo, M.F. Garcia-Parajo et al., Chromatin fibers are formed by heterogeneous groups of nucleosomes in vivo, *Cell* 160: 1145-1158, 2015.
[17] Y. Kinjo, K. Shinohara, A. Ito et al., Direct imaging in a water layer of human chromosome fibres composed of nucleosomes and their higher-order structures by laser-plasma X-ray contact microscopy, *J. Microsc.* 176: 63-74, 1994.
[18] K. Shinohara, H. Nakano, Y. Kinjo et al., Fine structure of unstained human chromosome fibres dried with no fixative as observed by X-ray contact microscopy, *J. Microsc.* 158: 335-342, 1990
[19] Y. Kinjo, M. Shigeno, K. Shinohara et al., Studies on the fine structure of wet human chromosome fibers unstained with no fixative by atomic force microscopy in comparison with X-ray contact microscopy, *Cytologia* 61: 327-336, 1996.
[20] A. Tanaka, A new replica method for electron microscopic studies with plasma polymerization-film in a glow discharge, *Seikagaku* 55: 1212-1219, 1983 (in Japanese).
[21] T. Yamada, H. Ohyama, Y. Kinjo et al., Evidence for internucleosomal breakage of chromatin in rat thymocytes irradiated in vitro, *Radiat. Res.* 85: 544-553, 1981.
[22] Y. Kinjo, M. Watanabe, A. Ito et al., X-ray microscopyand chromosome research, *Proc. 8th Int. Conf. X-ray Microscopy IPAP Conf. Series* 7: 227-229, 2006.
[23] W. Earnshow, U. K. Laemmli, Architecture of metaphase chromosomes and chromosome scaffolds, *J Cell Biol.* 96: 84–93, 1983.
[24] J. Gall, Chromosome fibers from an interphase nucleus, *Science* 139: 120–121, 1963.

EVALUATION OF THE RADICAL-SCAVENGING ACTIVITY OF ANTIOXIDANTS IN WATER USING A WATER-SOLUBILIZED 2,2-DIPHENYL-1-PICRYLHYDRAZYL RADICAL

I. Nakanishi[1]*, K. Ohkubo[1,2], T. Ozawa[3], K. Matsumoto[1]

[1]*Quantitative RedOx Sensing Team (QRST), Department of Basic Medical Sciences for Radiation Damages, National Institute of Radiological Sciences (NIRS), National Institutes for Quantum and Radiological Science and Technology (QST), Inage-ku, Chiba 263-8555, Japan*

[2]*Institute for Advanced Co-Creation Studies, Open and Transdisciplinary Research Initiatives, Osaka University, Suita, Osaka 565-0871, Japan*

[3]*Nihon Pharmaceutical University, Kitaadachi-gun, Saitama 362-0806, Japan*

**E-mail: nakanishi.ikuo@qst.go.jp*

Abstract

A 2,2-diphenyl-1-picrylhydrazyl radical (DPPH•) is relatively stable at room temperature and has been used as a reactivity model of reactive oxygen species. However, the insolubility of DPPH• in water has precluded its use in aqueous media without organic cosolvents, such as ethanol. Recently, we have succeeded in solubilizing DPPH• in water using *β*-cyclodextrin (*β*-CD). This enables us to evaluate the radical-scavenging activity of water-soluble antioxidants in aqueous media, particularly in physiological concentrations of buffer solutions, with use of the same probe, DPPH•, as that has been used in organic solvents for 60 years.

1. Introduction

The kinetic evaluation of the activity of antioxidants has been of considerable importance, because antioxidants need to scavenge reactive oxygen species (ROS) and related radicals to prevent diseases caused by oxidative stress, before these reactive species oxidize bio-related molecules, such as proteins, lipids, enzymes, and nucleic acids. However, ROS and related radicals are generally unstable at room temperature and difficult to be dealt with for the evaluation of the activity of antioxidants. Thus, reactivity models of ROS, which are stable at room temperature and can react with antioxidants, have been widely used to evaluate the activity of antioxidants. Among them, 2,2-diphenyl-1-picrylhydrazyl radical (DPPH•) has been frequently used for 60 years [1–3]. However, the insolubility of DPPH• in water has precluded its use in aqueous media without organic cosolvents, such as ethanol. The pH of the reaction media of antioxidants is of great importance, because antioxidant molecules have one or more ionizable hydroxy groups and their ionization state largely influences the reactivity of antioxidants. However, the pH of the reaction media is not precisely controlled in the presence of the organic cosolvents. Recently, we have reported that DPPH• is successfully solubilized in water using *β*-cyclodextrin (*β*-CD) (Figure 1a) [4]. An optimized structure of the inclusion complex of DPPH• with *β*-CD (DPPH•/*β*-CD) calculated by the density functional theory (DFT) demonstrates that the picryl moiety of DPPH• is incorporated into *β*-CD and the >N–N•– moiety exists outside of the *β*-CD cavity as shown in Figure 1b [5]. We herein introduce a novel technique to evaluate the kinetic radical-scavenging activity of antioxidants using DPPH•/*β*-CD in physiological concentrations of buffer solutions.

2. Experimental

2.1. Materials

DPPH•, ascorbic acid ($AscH_2$), and phosphate buffer powder were commercially obtained from Wako Pure Chemical Ind. Ltd., Japan. *β*-CD was purchased from Tokyo Chemical Industry Co., Ltd., Japan, recrystallized from water and dried under vacuum at 313 K. Trolox was commercially obtained from Aldrich. Methanol (MeOH; spectral grade) was purchased from Nacalai Tesque, Inc., Japan and used as received. The water used in this study was freshly prepared with a Milli-Q system (Millipore Direct-Q UV 3). DPPH• was solubilized in water by *β*-CD and the concentrations of DPPH•/*β*-CD were determined according to the procedure reported in the literature [4].

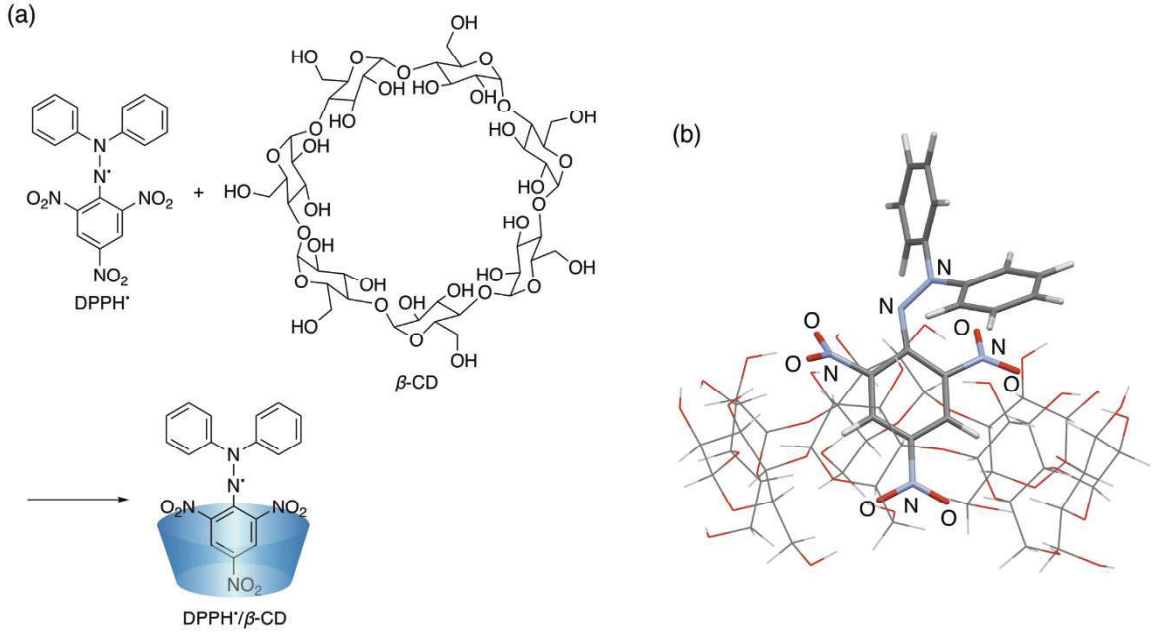

Figure 1: (a) Formation of the inclusion complex of DPPH• with β-CD. (b) Optimized structure of DPPH•/β-CD calculated using DFT (camB3LYP/6-318(d)/Def2TZV:C-PCM solvation model parameterized for water).

2.2. Spectral and kinetic measurements

The UV-vis spectra were recorded on an Agilent 8453 photodiode array spectrophotometer. The rates of the scavenging reaction of DPPH•/β-CD in a phosphate buffer (0.1 M, pH 7.4) by water-soluble antioxidants (i.e, Trolox and $AscH_2$) were determined by monitoring the absorbance change at 527 nm due to DPPH• after mixing of DPPH•/β-CD in water (Milli-Q) with a phosphate buffer solution (0.2 M, pH 7.4) containing the antioxidants (without β-CD) at a volumetric ratio of 1:1 using a stopped-flow technique on a UNISOKU RSP-1000-02NM spectrophotometer. Therefore, the final concentration of the phosphate buffer is 0.1 M. The pseudo-first-order rate constants (k_{obs}) were determined by a least-square curve fit using an Apple MacBook Pro personal computer. The first-order plots of $\ln(A - A_\infty)$ as a function of time (A and A_∞ are the absorbance at the reaction time and the final absorbance, respectively) were linear until three or more half-lives with a correlation coefficient $\rho > 0.999$.

3. Results and Discussion

When Trolox, a water-soluble analog of α-tocopherol (vitamin E), was added to the phosphate buffer solution (0.1 M, pH 7.4) of DPPH•/β-CD, the absorption band at 527 nm due to DPPH• disappeared immediately with clear isosbestic points at 320, 338, and 431 nm as shown in Figure 2a. Since the pK_a value of Trolox is reported to be 3.6 [6], the carboxy group in Trolox undergoes deprotonation in phosphate buffer solution (0.1 M, pH 7.4). Thus, this spectral change indicates that the anionic form of Trolox efficiently scavenged DPPH• (equation 1). Spectral titration shows the stoichiometry, the DPPH•/Trolox molar ratio being 2:1 (Figure 2b) (equation 1). The decay of the absorbance at 527 nm monitored by a stopped-flow technique obeyed pseud-first-order kinetics, when the concentration of Trolox ([Trolox]) was maintained at more than a 10-fold excess of DPPH• concentration (Figure 3a). In this case, all the DPPH• was consumed, before the corresponding phenoxyl radical of Trolox, generated by the reaction with DPPH•, reacts with the second DPPH• as shown in equation 2. The pseudo-first-order rate constant (k_{obs}) linearly increased with increasing [Trolox] (Figure 3b). From the slope of the linear plot, the second-order rate constant (k) for the DPPH•-scavenging reaction by Trolox was determined in a phosphate buffer (0.1 M, pH 7.4) to be 1.8×10^4 M^{-1} s^{-1}. This k value is about 80-fold larger than that for the reaction of Trolox with DPPH• in methanol (MeOH) ($k = 2.3 \times 10^2$ M^{-1} s^{-1}) (Figure 3b). Thus, the reaction media significantly affect the reactivity of antioxidants [7,8].

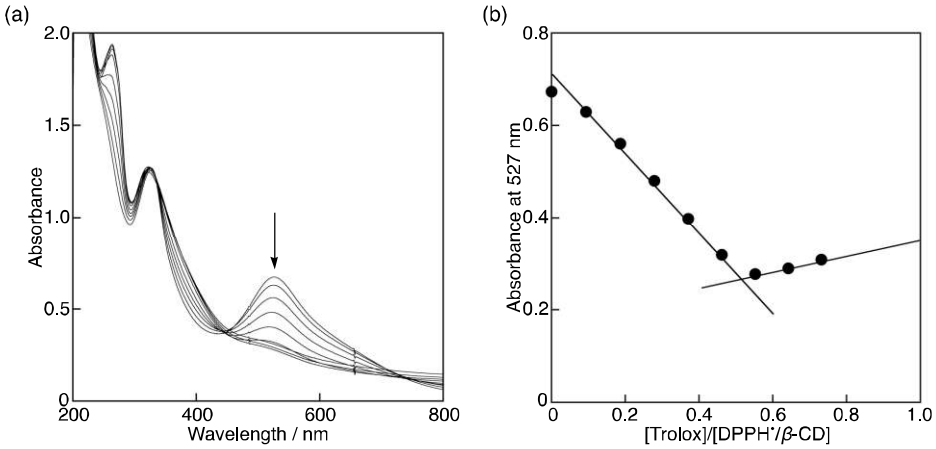

Figure 2: (a) Spectral change observed upon addition of Trolox (0–4.6 × 10^{-5} M) to DPPH•/β-CD (6.3 × 10^{-5} M) in phosphate buffer (0.1 M, pH 7.4). (b) Plot of the absorbance at 527 nm vs. [Trolox]/[DPPH•/β-CD].

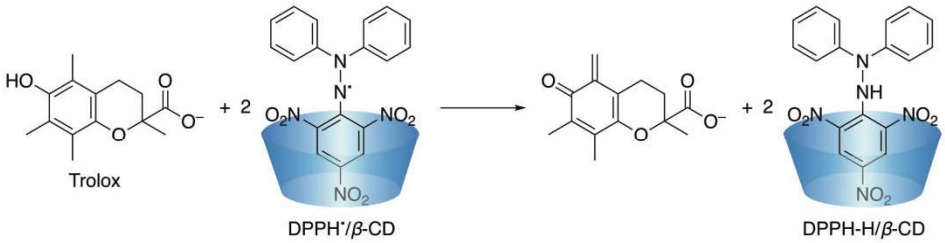

(1)

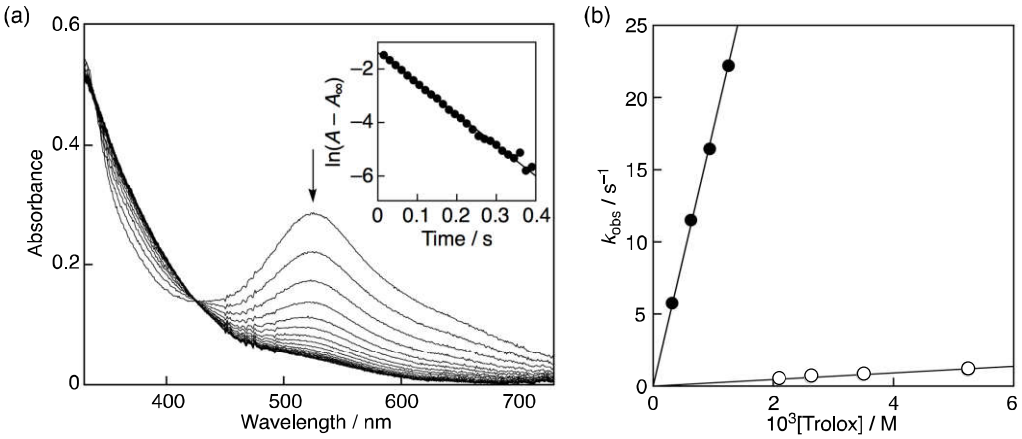

Figure 3: (a) Spectral change (interval: 25 ms) observed during the reaction of Trolox (6.3 × 10^{-4} M) with DPPH•/β-CD (3.0 × 10^{-5} M) in phosphate buffer (0.1 M, pH 7.4) at 298 K. Inset: the first-order plot of the absorbance at 527 nm. (b) Plots of k_{obs} vs. [Trolox] for the reactions of Trolox with DPPH•/β-CD in phosphate buffer (0.1 M, pH 7.4) (closed circles) and with DPPH• in MeOH (open circles).

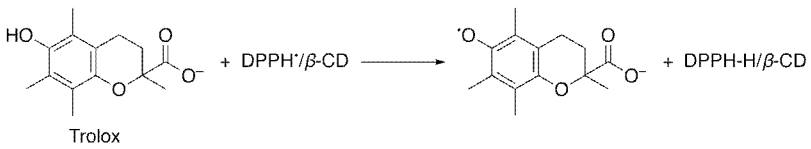

(2)

When Trolox was replaced by ascorbic acid ($AscH_2$), a representative water-soluble antioxidant, a similar spectral change was observed as shown in Figure 4a. $AscH_2$ having a pK_a value of 4.1 also undergoes deprotonation in phosphate buffer solution (0.1 M, pH 7.4) and exists in its anionic form [9], $AscH^-$. Thus, the actual species that scavenged DPPH• is $AscH^-$ (equation 3). Spectral titration showed that one $AscH^-$ can scavenge two molecules of DPPH• (Figure 4b) (equation 3). The *k* value for the reaction of excess $AscH_2$ with

DPPH•/β-CD (equation 4) was also determined in the same manner to be 7.2×10^3 M^{-1} s^{-1} (Figure 5). On the other hand, in MeOH, the k_{obs} values for the DPPH•-scavenging reaction by $AscH_2$ were much smaller than those in phosphate buffer solution (0.1 M, pH 7.4) and independent of changes in the $AscH_2$ concentration used in excess (Figure 5b). These results suggest that

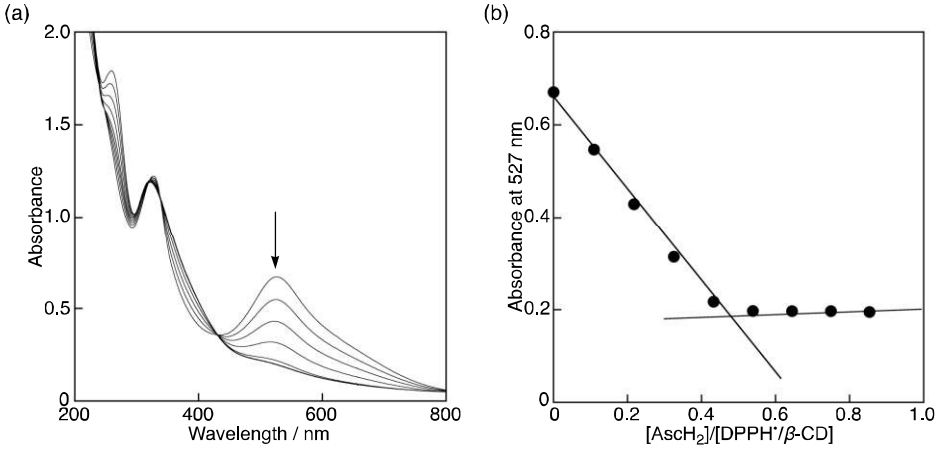

Figure 4: (a) Spectral change observed upon addition of $AscH_2$ (0–5.4 × 10^{-5} M) to DPPH•/β-CD (6.3 × 10^{-5} M) in phosphate buffer (0.1 M, pH 7.4). (b) Plot of the absorbance at 527 nm vs. [$AscH_2$]/[DPPH•/β-CD].

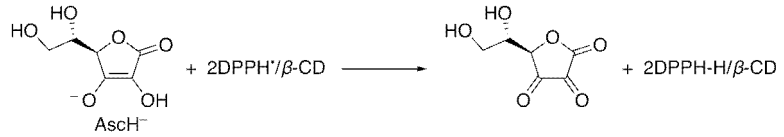

(3)

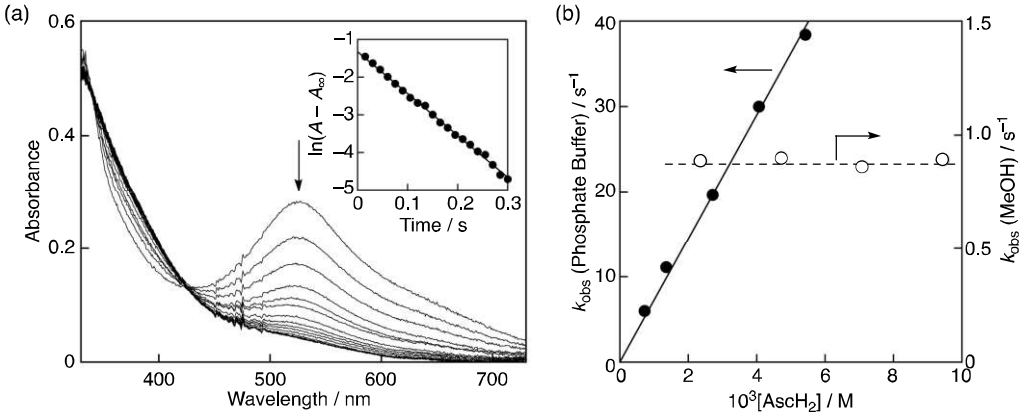

Figure 5: (a) Spectral change (interval: 25 ms) observed during the reaction of $AscH_2$ (1.4 × 10^{-3} M) with DPPH•/β-CD (3.0 × 10^{-5} M) in phosphate buffer (0.1 M, pH 7.4) at 298 K. Inset: the first-order plot of the absorbance at 527 nm. (b) Plots of k_{obs} vs. [$AscH_2$] for the reactions of $AscH_2$ with DPPH•/β-CD in phosphate buffer (0.1 M, pH 7.4) (closed circles) and with DPPH• in MeOH (open circles).

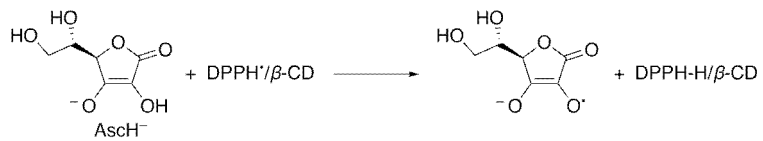

(4)

in MeOH, little $AscH_2$ may undergo deprotonation to give $AscH^-$, which efficiently scavenges DPPH• as shown in Scheme 1. Thus, the rate-determining step for the DPPH•-scavenging reaction by $AscH_2$ in MeOH may be the deprotonation of $AscH_2$. As in the case of Trolox, the solvent significantly affects the reactivity of antioxidants as well as the radical-scavenging mechanism [7,8].

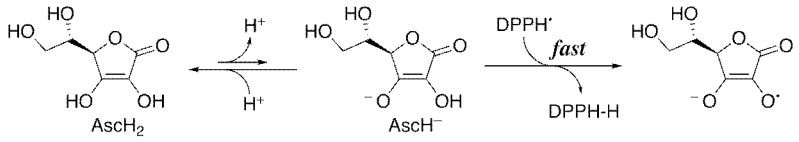

Scheme 1: Proposed mechanism of the DPPH•-scavenging reaction by $AscH_2$ in MeOH.

4. Conclusions

The solubilization of DPPH• in water by *β*-CD enables us to evaluate the radical-scavenging activity of antioxidants in aqueous media, particularly in physiological concentrations of buffer solutions [4,5,10], with use of the same probe, DPPH•, as that has been used in organic solvents for 60 years.

Acknowledgements

This work was partially supported by Grant-in-Aid (No. 18K06620) from the Ministry of Education, Culture, Sports, Science and Technology, Japan.

References

[1] M.S. Blois, Antioxidant determinations by the use of a stable free radical, *Nature* 181: 1199–1200, 1958

[2] M.C. Foti, Use and abuse of the DPPH• radical, *J. Agric. Food Chem.* 63: 8765–8776, 2015

[3] K. Pyrzynska, A. Pękal, Application of free radical diphenylpicrylhydrazyl (DPPH) to estimate the antioxidant capacity of food samples, *Anal. Methods* 5: 4288–4295, 2013

[4] I. Nakanishi, K. Ohkubo, K. Imai et al., Solubilisation of a 2,2-diphenyl-1-picrylhydrazyl radical in water by *β*-cyclodextrin to evaluate the radical-scavenging activity of antioxidants in aqueous media, *Chem. Commun.* 51: 8311–8314, 2015

[5] I. Nakanishi, K. Ohkubo, M. Kamibayashi et al., Reactivity of 2,2-diphenyl-1-picrylhydrazyl solubilized in water by *β*-cyclodextrin and its methylated derivative, *ChemistrySelect* 1: 3367–3370, 2016

[6] J. Małyszko, M. Mechanik, Anodic oxidation of Trolox in aqueous solutions, *Polish J. Chem.* 78: 1575–1582, 2004

[7] G. Litwinienko, K.U. Ingold, Solvent effects on the rates and mechanism of reaction of phenols with free radicals, *Acc. Chem. Res.* 40: 220–230, 2007

[8] I. Nakanishi, T. Kawashima, K. Ohkubo et al., Electron-transfer mechanism in radical-scavenging reactions by a vitamin E model in a protic medium, *Org. Biomol. Chem.* 3: 626–629, 2005

[9] C. Creutz, Complexities of ascorbate as a reducing agent, *Inorg. Chem.* 20: 4449–4452, 1981

[10] E. Sekine-Suzuki, I. Nakanishi, K. Imai et al., Efficient protective activity of a planar catechin analogue against radiation-induced apoptosis in rat thymocytes, *RSC Adv.* 8: 10158–10162, 2018

THE USE OF EINSTEIN–SMOLUCHOWSKI EQUATION TO STUDY THE CHEMICAL REACTION-DIFFUSIONS IN NEURONS INDUCED BY A CHARGED PARTICLE

T. Togtokhtur[1]*, O. Lkhagva[1], M. Batmunkh[2], L. Bayarchimeg[2], T. Lkhagvajav[1]

[1]*Department of Physics, National University of Mongolia, Ulaanbaatar 210646, Mongolia*
[2]*Laboratory of Radiation Biology, Joint Institute for Nuclear Research, Dubna 141980, Russia*
**E-mail: tudewdorj.togtokhtur@gmail.com*

Abstract

In this work we shall consider how to solve the Einstein-Smoluchowski equation of the chemical reaction and diffusion of the free radicals formed when a charged particle passes through the neural cells. This process is described by a system of the partial differential equation which is being solved by the finite-difference method. The results of numerical solution are found in good agreement with Monte Carlo simulation results obtained by microdosimetry calculations of the GEANT4-DNA code. The chemical reactions between the water radiolysis and the neuronal DNA after irradiation with low-energy electrons were also studied. Changes in the concentrations of these radicals, due to chemical reactions are described using numerical solutions of the Einstein-Smoluhowski equation.

1. Introduction

The diffusion-reaction process plays key role in the study of particle and radiation interactions with biological objects. Nowadays the problem of DNA damage by charged particles and radiations represent actuality due to essential necessity to ensure cosmonauts for future trip in space mission and many practical purposes, particularly, to work out new innovations, nuclear medicine including cancer therapy techniques.

The problem of chemical diffusion-reaction, caused by the DNA damage has considered in theoretical investigations [1, 2]. In these investigations, the Einstein-Smoluchowski diffusion equation is applied for describing the chemical reactions. At the same time, M. Batmunkh and L. Bayarchimeg have made micro-dosimetrical estimations using GEANT4-DNA code [3]. Diffusion of radicals and chemical reactions between them in neuronal DNA are described by solutions of the Einstein-Smoluchowski diffusion equation.

2. Theoretical and computational approach

2.1. Equation of the radical diffusion

The diffusion of the radicals is characterized by the following radial equation [1]:

$$\frac{\partial C(r,t)}{\partial t} = D\left[\frac{1}{r^2}\frac{\partial}{\partial r}\left(r^2 \cdot \frac{\partial C(r,t)}{\partial t}\right)\right]. \tag{1}$$

where, *C (r, t)* is the concentration of radical distribution. *D* is diffusion coefficient. When $t \to 0$ at concentration must be taken greater than zero.

The analytic solution of equation (1) is written as:

$$C(r,t) = \frac{N_0}{8(\pi Dt)^{3/2}} e^{-\frac{r^2}{4Dt}} \tag{2}$$

The formula (2) describes concentrations of radicals along definite direction when the distribution has spherical symmetry. Integrating (2) all-over spherical angles, we get:

$$\int C(r,t)d\Omega = \int C(r,t)\mathrm{r}^2 dr \int_0^{\pi} \sin(\theta)d\theta \int_0^{2\pi} d\phi = \int \frac{4\pi r^2}{8(\pi Dt)^{3/2}} e^{-\frac{r^2}{4Dt}} dr$$

Then the radial distribution can be written as

$$C(r,t) = \frac{4\pi r^2}{8(\pi D t)^{3/2}} e^{-\frac{r^2}{4Dt}} \quad . \tag{3}$$

By integrating equation (3), the initial concentration can be obtained as follows:

$$\int_0^\infty C(r,t=0)dr = C_0. \tag{4}$$

The equation (1) can be solved by finite difference method [4]. At first the SI system should be transferred to units: nanometer and nanosecond. Taking into account the unit shift diffusion coefficient can be written below:

$$D = 2.8 \cdot 10^{-9} \frac{m^2}{s}, \qquad D = 2.8 \cdot \frac{nm^2}{ns} \cdot \tag{5}$$

To perform numerically solution of the equation (1) it should to be written in finite difference form:

$$C_{i,j+1} = \beta_i C_{i-1,j} + \gamma_i C_{i,j} + \alpha C_{i+1,j} \quad . \tag{6}$$

Here, i define number along radius and j is number discrete moments of time.

$$\alpha = \frac{D \cdot \tau}{h^2}, \quad \beta_i = \alpha\left(1 - \frac{2}{i}\right), \quad \gamma_i = \alpha\left[\left(\frac{2}{i} - 2\right) - \frac{1}{\alpha}\right] \cdot \tag{7}$$

Alpha is unit less constant, τ is step of the time and h is step of the coordinates.

2.2. Diffusion chemical reaction of Einstein-Smoluchowski equation

Chemical radicals perform random motion. The ions might come into chemical reactions. Such processes are described with next scheme (8).

$$\begin{cases} e^- + nH_2O \xrightarrow[k_{e^- \to H_2O}]{} e^-_{aqua} \\ 2e^-_{aqua} + 2H_2O \xrightarrow[k_{e^-_{aqua} \to H_2O}]{} H_2 + 2OH^- \\ H_2O_2 + e^-_{aqua} \xrightarrow[k_{e^-_{aqua} \to H_2O_2}]{} OH^- + \bullet OH \end{cases} \tag{8}$$

Chemical reaction rates are as follows:

$$\begin{aligned} k_{e^- \to H_2O} &= 1.1 \cdot 10^{-10}\, mole^{-1} s^{-1} \\ k_{e^-_{aqua} \to H_2O} &= 0.5 \cdot 10^{-10}\, mole^{-1} s^{-1} \\ k_{e^- \to e^-_{aqua}} &= 3.35 \cdot 10^{-10}\, mole^{-1} s^{-1}. \end{aligned} \tag{9}$$

Diffusion-reaction process between radicals is described by solution of following coupled Einstein-Smoluchowski equation:

$$\frac{\partial C^m(r,t)}{\partial t} = D^m \left[\frac{1}{r^2}\frac{\partial}{\partial r}\left(r^2 \cdot \frac{\partial C^m(r,t)}{\partial t}\right)\right] - \sum_{n \neq m} k_{mn} C^n(r,t) C^m(r,t) + \sum_{M_m \in \{n,l\}} k_{nl} C^n(r,t) C^l(r,t). \tag{10}$$

This equation (10) defines the dynamic development of concentration due to diffusion and chemical reactions between radicals. $C^m(r, t)$ is the concentration of *m-th* ion at position r and moment t.
The radial distributions of ionized water and electrons produced in neuronal DNA obtained by means of microdosimetry technique built in GEANT4-DNA code (see Figure1).

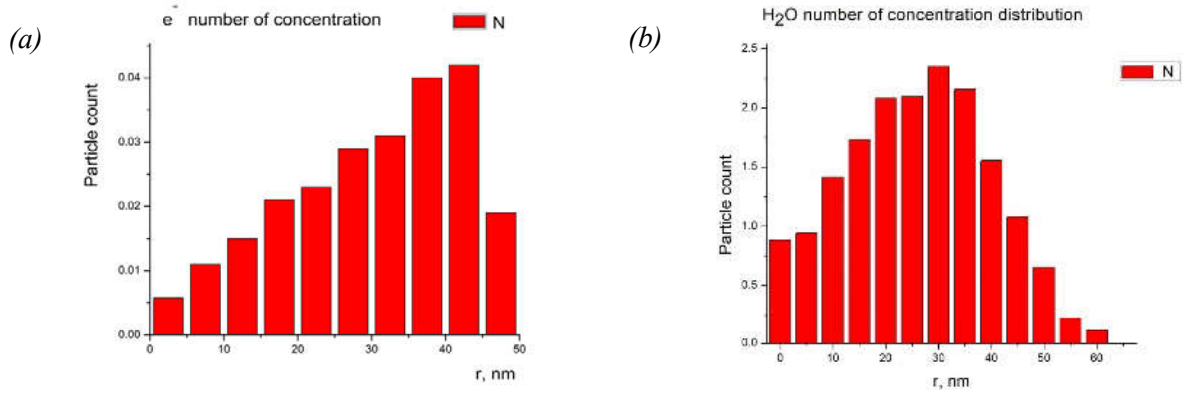

Figure 1: Radial distributions of ionized water (a) and electrons in nanometric cube volume at 1 ps (b).

To get estimation of radicals' distributions shown in scheme (8) and the equation (10) were to be transformed in finite difference form.
Here coupled diffusion equation:

$$\begin{cases} C_{i,j+1}^{H_2O} = \beta_i D^{H_2O} C_{i-1,j}^{H_2O} + \left\{ \gamma_i D^{H_2O} - k_{H_2O \to e^-} C_{i,j}^{e^-} - k_{H_2O \to e^-_{aqua}} C_{i,j}^{e^-_{aqua}} \right\} C_{i,j}^{H_2O} + \alpha D^{H_2O} C_{i+1,j}^{H_2O} + \cdots \\ + k_{e^- \to e^-_{aqua}} C_{i,j}^{e^-} C_{i,j}^{e^-_{aqua}} + k_{e^-_{aqua} \to e^-} C_{i,j}^{e^-_{aqua}} C_{i,j}^{e^-} \\ C_{i,j+1}^{e^-} = \beta_i D^{e^-} C_{i-1,j}^{e^-} + \left\{ \gamma_i D^{e^-} - k_{e^- \to H_2O} C_{i,j}^{H_2O} - k_{e^- \to e^-_{aqua}} C_{i,j}^{e^-_{aqua}} \right\} C_{i,j}^{e^-} + \alpha D^{e^-} C_{i+1,j}^{e^-} + \cdots \\ + k_{H_2O \to e^-_{aqua}} C_{i,j}^{H_2O} C_{i,j}^{e^-_{aqua}} + k_{e^-_{aqua} \to H_2O} C_{i,j}^{e^-_{aqua}} C_{i,j}^{H_2O} \\ C_{i,j+1}^{e^-_{aqua}} = \beta_i D^{e^-_{aqua}} C_{i-1,j}^{e^-_{aqua}} + \left\{ \gamma_i D^{e^-_{aqua}} - k_{e^-_{aqua} \to H_2O} C_{i,j}^{H_2O} - k_{e^-_{aqua} \to e^-} C_{i,j}^{e^-_{aqua}} \right\} C_{i,j}^{e^-_{aqua}} + \alpha D^{e^-_{aqua}} C_{i+1,j}^{e^-_{aqua}} + \cdots \\ + k_{H_2O \to e^-} C_{i,j}^{H_2O} C_{i,j}^{e^-} + k_{e^- \to H_2O} C_{i,j}^{e^-} C_{i,j}^{H_2O} \end{cases} \quad (11)$$

This system equation (11) describes changes of radical concentration in space-time. As initial conditions were we taken by the Figure1.

3. Numerical results and Monte Carlo simulations

In this work, microdosimetry distributions of hydroxide, arisen within the geometry of neuronal DNA exposed to charged particle beam has been investigated. At the same time, diffusion equation is converted into finite difference form. In numerical calculation, the corresponding values from analytic solution (2) were taken as boundary condition of equation (6).

The ion concentration distributions obtained using numerical solutions of the free radial diffusion equation are compared with microdosimetry estimates (see Figure2).

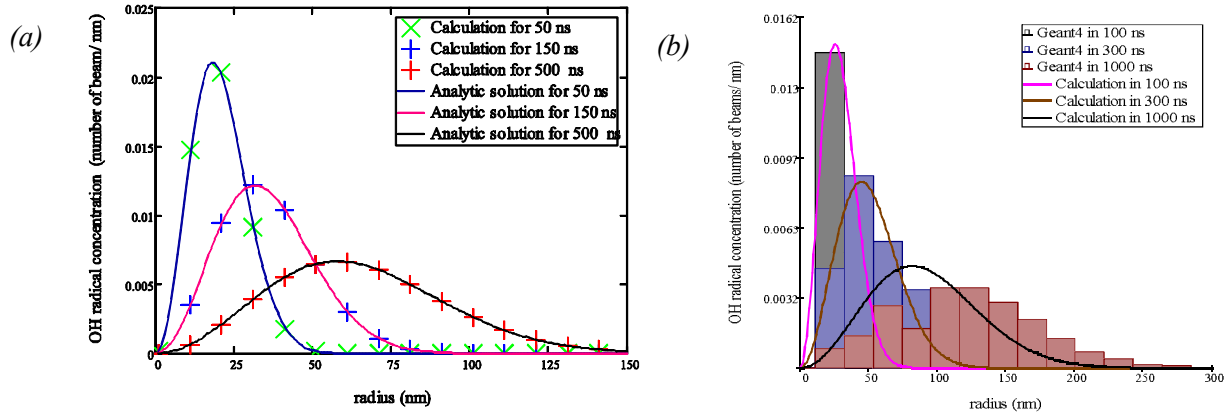

Figure 2: In the graphics, number of hydroxide different peaks in a radius have been at per moment are shown. The (a) shows the concentration curves marked "x" and "+" are in well coincidence with the exact solutions of equation (1). In (b), the histograms obtained using microdosimetry estimates are compared with the equation (1).

Figure 3 shows radius and time dependence of the aqua molecule concentration which is calculated by equation (11).

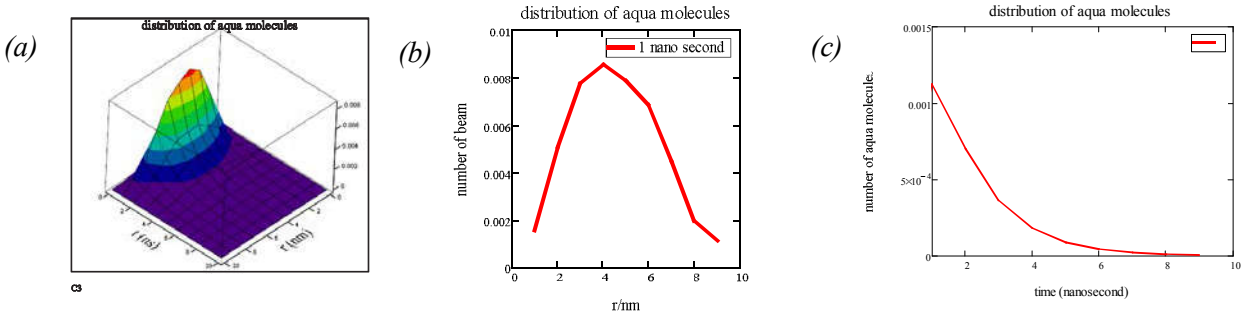

Figure 3: 3D surface plot are shown distribution of aqua molecules along to the space and the time (a). Red curve is the radial distribution at 1 nanosecond (b). Number of the aqua molecule decreases in during reaction time (c).

4. Conclusion

Numerical solutions calculated with finite difference algorithm are found in good agreement with analytic solutions of the free diffusion equation. The solutions of equation (6) describing the hydroxide concentration are consistent with microdosimetric histograms obtained using the GEANT4-DNA Monte Carlo toolkit.
A numerical algorithm has been developed for solving coupled diffusion equations for hydroxyl radicals, electrons, and water molecules. The space-time distribution of the aqua molecule concentration was calculated. Due to the lack of computing power, other radicals have not been included in the calculations. Complete consideration of diffusion chemical reactions will be done in the next work.

References

[1] M. Karamitros, S. Luan, M.A. Bernal et al., Diffusion-controlled reaction modeling in GEANT4-DNA, *J. Comput. Phys.* 274: 841-882, 2014.
[2] S. Kuckov´a, Mathematical modeling of radiobiological effect of oxygen, *WDS'05 Proc. Contribut. Papers,* Prague, Czech Republic, 185–189, 2005.
[3] M. Batmunkh, L. Bayarchimeg, O.V. Belov et al., Simulation radiation damage to neural cell with GEANT4-DNA, Euro. Phys. J. WoC 173: 05005, 2018.
[4] O. Lkhagva, M. Batmunkh, *Computational mathematica and physics,* Admonprint LTD, Ulaanbaatar, 2015. (in Mongolian)

COMPUTER MODELING OF RADIATION-INDUCED DAMAGE TO HIPPOCAMPAL CELLS

M. Batmunkh[1]*, A. N. Bugay[1], L. Bayarchimeg[1,2], S. V. Aksenova[1], T. Togtokhtur[3], O. Lkhagva[3]

[1]*Laboratory of Radiation Biology, Joint Institute for Nuclear Research, Dubna 141980, Russia*
[2] *Institute of Physics and Technology, Mongolian Academy of Sciences, Ulaanbaatar 13330, Mongolia*
[3]*Division of Natural Sciences, National University of Mongolia, Ulaanbaatar 210646, Mongolia*
**E-mail: batmunkh@jinr.ru*

Abstract

The development of measurement-based simulation approach of radiation-induced alterations in the nervous system (i.e. hippocampal cells) seems to be an extremely important task in the analysis of the neuro-radiobiological effects of accelerated charged particles and in the extrapolation of limited experimental data. For this purpose, the present work focuses at designing and considering a model of possible targets in the hippocampus with the aim of understanding the electrical properties of the neural networks after irradiation. The stochastic simulation of particle tracks and dynamics of action potential spikes in hippocampal cells were performed by using the Geant4 Monte Carlo radiation transport code and the NEURON simulation environment. The developed model of the rat hippocampus contains different types of neural cells - pyramidal and granule cells in the cornu ammonis (CA3/CA2/CA1) and the dentate gyrus (DG), heterogeneous populations of interneurons and neural stem cells, which are connected to each other by synapses. Track simulations were made for beams of heavy charged particles with different characteristics. The distribution of microscopic energy depositions and production of oxidative radical species were obtained and analyzed in critical structures of the hippocampal cells after the irradiation. Moreover, the dynamics of action potential and spike frequency on the membranes were calculated in the individual neurons and neural networks. As the result, we obtained the number of injured neurons in DG, which is observed larger than injured neurons in CA3/CA1 of hippocampus after irradiation.

1. Introduction

The study of evaluating radiation effects on the central nervous system (CNS) induced by accelerated charged particles is very complex and challenging task in modern radiation research, as well as radiotherapy and biophysics [1, 2]. Recent experimental studies at particle accelerators have shown that the radiation-induced brain injury leads to various behavioral changes and cognitive impairments, including dendritic spine morphogenesis, synaptic plasticity, neurogenesis, etc. [3-5]. The majority of these studies have focused on the hippocampus, which plays an important role in learning and memory consolidation, as well as the formation of new neurons. However, the molecular mechanism of radiation-induced cellular damage remains unclear and requires precise evaluation of molecular damages in the sensitive structures of neural cells, such as synaptic receptors (NMDA, AMPA and GABA) and genomic DNA (Deoxyribonucleic acid). A single neuron consists of a cell body (soma) containing the genomic DNA, complex dendritic trees with multiple branches, an axon and dendritic spines with synaptic receptors which are the substrates for memory storage and synaptic transmission.

The physical characteristics of radiation trajectory (tracks) play an important role in the biological effects at the molecular and cellular levels [6]. The initial track structure of heavy charged particles produces greatly different patterns of energy deposition compared to ionizing electromagnetic radiations (*X*- and γ-rays) when they penetrate into the brain cells [7]. According to this, radiation damage to the cell can be caused by the direct action of ionization events and indirect action of oxidative free-radicals produced in water medium surrounding the molecular target. With the use of Monte Carlo approach, it's possible to simulate the stochastic nature of energy deposition and water radiolysis in the tracks of charged particles [8]. An important aspect in this simulation is the geometrical description of the complicated neuron morphology from molecules to cell populations. In the present work we consider the model of the rat hippocampus to establish a basis for simulation of realistic large-scale neural networks followed by energy deposition in particle tracks. The track structures of energetic heavy ions and their secondary particles produced within hippocampal cells were scored and analyzed.

2. Materials and methods

We performed a Monte Carlo radiation transport simulation [9] to investigate the influence of particle track structures in the rat hippocampus at different levels of its organization (molecular, cellular, and tissue). The applied simulation technique provides the 'full set' of physics processes including nuclear and electromagnetic interactions, and chemical reactions initiated by water radiolysis up to ten microseconds after irradiation.

In particular, the Geant4-DNA [10] models are used inside the critical neuron structures and allow the transport of charged particles as well as of secondary electrons down to very low energies (7.4 eV). The simulation medium was filled with liquid water, which constitutes an approximation for biological material within complex geometries.

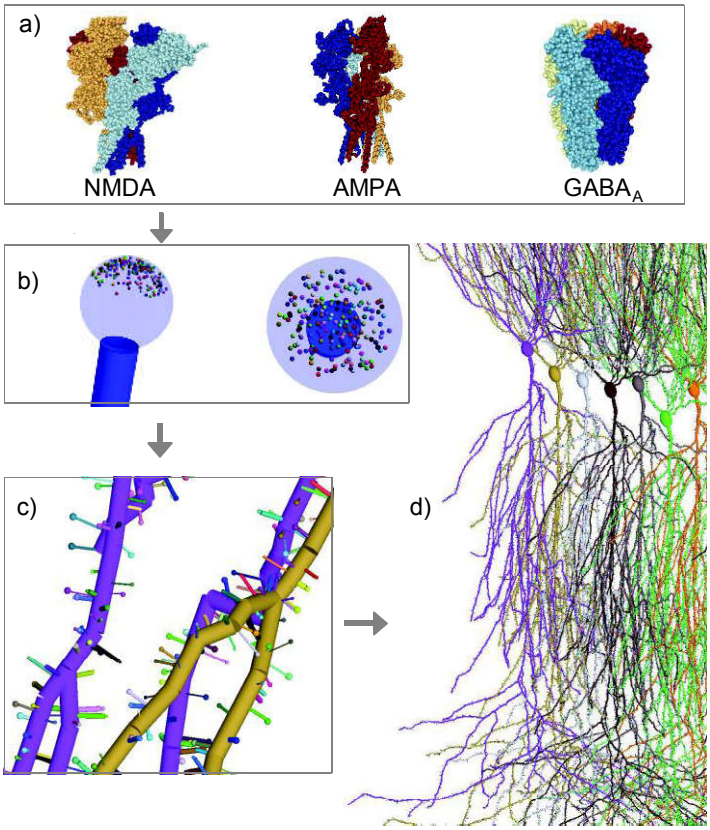

Figure 1: Organization of ionotropic receptors and spines on dendritic trees of neural cells: a) An atomistic model of NR1a/2b NMDA, GluA2/3 AMPA and GABA$_A$ receptor (β3 homopentamer). Atoms in different colors are used to represent the four and five subunits of glutamate (NMDA, AMPA) and GABA$_A$ receptor. b) A head of dendritic spine with receptors that are randomly placed within the PSD. c) A dendritic segment of individual neurons with spines and receptors. d) A snapshot of CA1 pyramidal neuron network in model of the rat hippocampus.

Sample 3D geometries of individual neurons with spines, receptors and genomic DNA are illustrated in Fig. 1 and Fig. 2. A single CA1 pyramidal neuron in the rat hippocampus is simulated with $1.5 \cdot 10^4$ spines, $1.9 \cdot 10^6$ receptors and 5439.67 Mbp (Mega base-pair), respectively. The complex morphology of dendritic trees was constructed from the microscopy-based data in the Claiborne archive at the neuromorpho.org repository. The molecular structure of receptors (NMDA, AMPA and GABA) and DNA segment can be extract from experimentally-determined databases in the rcsb.org archive with the explicit position of each atom in these structures. Corresponding van der Waals radius were used to represent each atom in three types of receptors (see Fig.1a). A single base-pair of DNA containing sugar (S) and phosphate (P) chains, and nucleotide base-pair of adenine-thymine (A-T) or guanine-cytosine (G-C) (see Fig.2g). A full description of the neuron geometry implementation in Geant4 is already available in our previously published works and Geant4 application [7, 11, 12].

The rat hippocampus model illustrated in Fig. 3 contains populations of 3840 CA1 pyramidal neurons, 2401 CA3/CA2 pyramidal neurons, 11960 DG granule cells, 496 mossy cells in hilus (HMC), 560 DG immature

neurons (IMN) and 110 neural stem cells (NSC) in the subgranular zone. The neurons are simulated in the hippocampal regions within the water box with overall dimensions of 4608×7106×1000−μm.

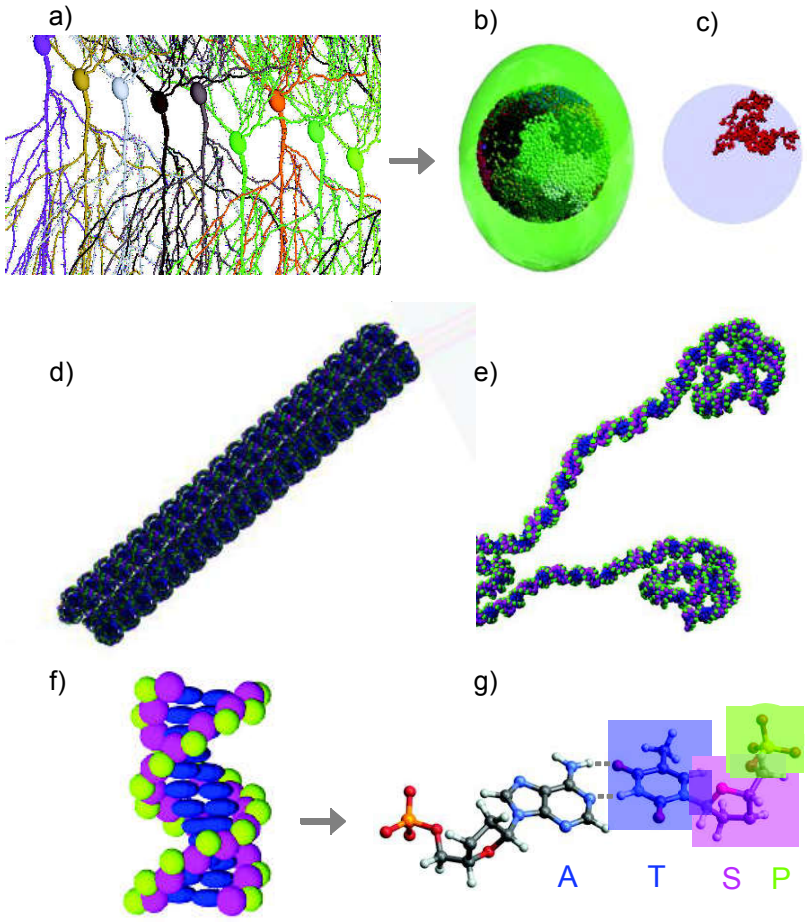

Figure 2: Organization of DNA in soma of neural cells: A screenshot of neuronal soma (a) each containing cell nucleus (b) with spherical chromatin domains representing the chromosome territories. c) An example of chromosome 10 with 110.63 Mbp. A segment of compacted (d) and extended (e) chromatin fibers representing the hetero- and eu-chromatins. f) A segment of 12bp DNA with the sequence of GGCAAAAAACGG. The position and volume of each molecule are calculated from the PDB file (pdb id: 1fzx), and represented by the union of all the atoms conforming a sugar, phosphate and bases. g) A single base-pair to construct a DNA double helix. The nucleotide bases (A-T or G-C), S and P molecules are represented as blue, magenta and green-yellow transparent ellipsoids.

The distributions of energy deposition events were computed for track of ^{56}Fe particles with energy of 600 MeV/u. Such particles are present in the spectra of galactic cosmic rays and several times higher biological efficiency that for other particle beams. As follows from previous calculations [13], the mean number of direct hits by physical interactions with non-zero energy depositions and indirect hits by chemical interactions of hydroxyl radicals (•OH) and solvated electrons (e^-_{aq}) calculated for the molecular targets at one nanosecond after irradiation. Modeling of the action potential generation and propagation on the membranes of neural cells was carried out in the NEURON (v.7.4) simulation environment [14].

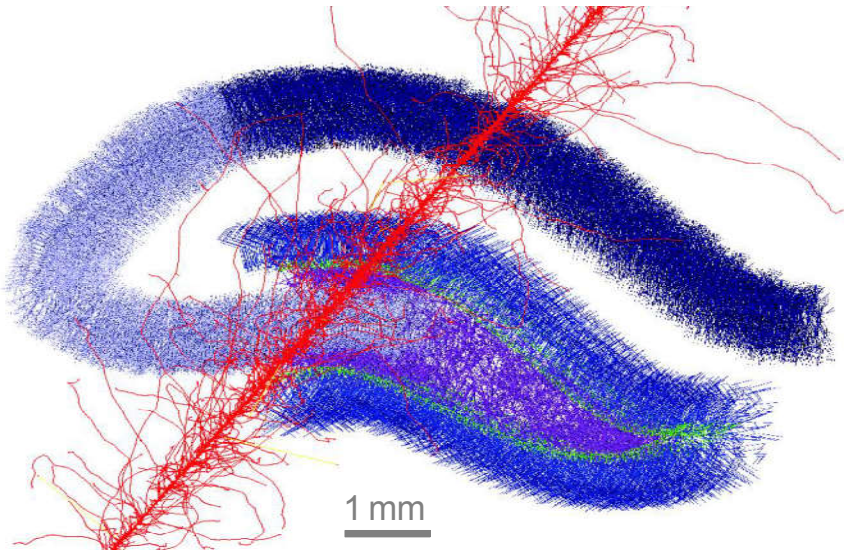

Figure 3: A sample three-dimensional representation of different neurons in the rat hippocampus which are traversed by single track of 600 MeV/u iron ion. The hippocampus model (dorsal view) contains the DG granule cells - blue, IMN and NSC in the subgranular zone - green, HMC in the hilus - purple, CA1 pyramidal neurons - dark blue, and CA3/CA2 pyramidal neurons - light blue. The energy deposition in track structure of iron ion is given in red.

3. Results and discussions

The mean number of irradiated neurons in the rat hippocampus by single track of 600 MeV/u iron particle is plotted in Fig. 4. It is shown that the largest number of irradiated neurons are found in the DG region of hippocampus, because a large number of DG granule cells are located in the DG region. On the other hand, the amount of energy deposition in neural stem cells is much smaller than other types of hippocampal neurons (see Fig. 4b). However, these numbers could be of great importance, because proliferating neural stem cells are the most radiosensitive in contrast to other more abundant neuron types throughout the hippocampus. Figure 5 presents detailed analysis of energy depositions and water radiolysis within molecular target of receptors (NMDA, AMPA and $GABA_A$ and 162 bp DNA nucleosome (pdb id: 1eqz + 1fzx) after irradiation with 600 MeV/u iron ion. The mean number of direct hits in $GABA_A$ receptor was higher than in NMDA and AMPA receptors. They also indicate that the mean number of indirect hits per track is larger in NMDA receptor than in AMPA and $GABA_A$ receptors (see Fig. 5a). The reported calculations are also in qualitative agreement with experimental findings, which reported that NMDA [15] and $GABA_A$ [16] receptors belong to the critical molecular targets in irradiated neural cells.

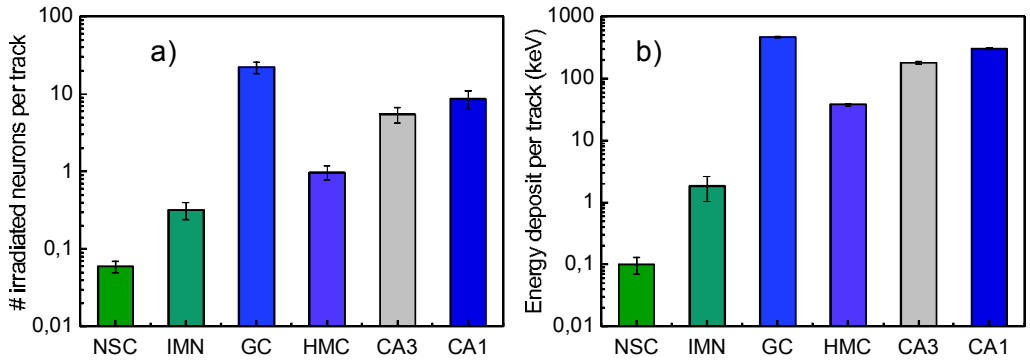

Figure 4: Mean number of irradiated neurons in different regions of the rat hippocampus following exposure to single iron ion with energy of 600 MeV/u (a). After irradiation, energy deposition in hippocampal neurons per track of iron ion (b).

In the case of DNA segment (Fig. 5b), the percentage of indirect damage produced by •OH and e^-_{aq} is higher than direct strand breaks. It is also shown that the percentage of base damage (BD), single strand break (SSB) and double strand break (DSB) per track of iron ion were 63%, 24% and 13%, respectively. For whole genome of hippocampal neurons, we obtained 11.6±1.2 and 31.8±4.6 clustered DSB per cell per gray of absorbed dose

after irradiation with Gamma rays and iron ions. Our results for Gamma rays are consistent with the experimental results in the rat hippocampal cells and Purkinje neurons [4, 17]. In fact, clustered DSB is responsible for very slow repair or not repairable. If DNA damage is not repaired or DNA repair is not correctly performed, it might lead to genome instability, gene mutation, cell cancer or cell death, etc.

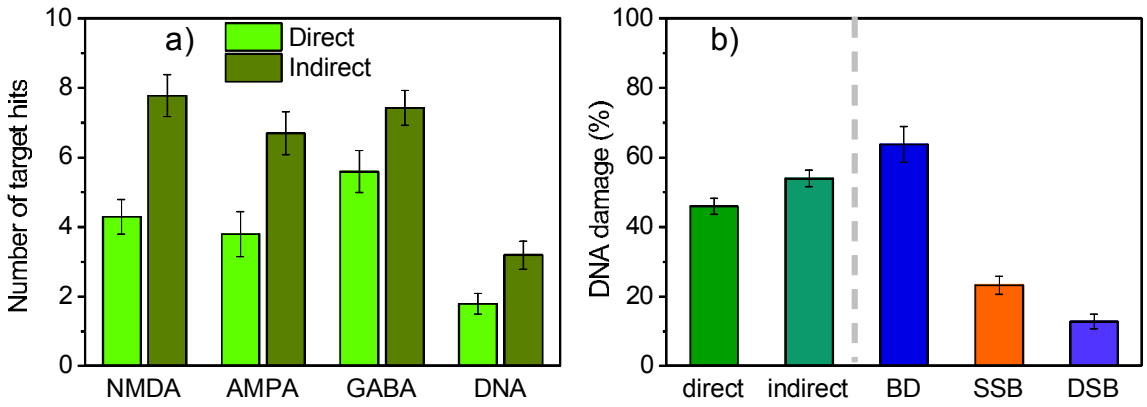

Figure 5: Mean number of direct and indirect hits in molecular targets of receptors (NMDA, AMPA and $GABA_A$ and DNA nucleosome (162 bp) following exposure to single iron ion with energy of 600 MeV/u (a). After irradiation, the percentage of DNA damage including direct and indirect strand breaks, BD, SSB and DSB per track of iron ion (b).

Previous calculations [13, 18] suggest that the synapses (receptors) seem to be more sensitive targets, than membrane ionic channels. Recently, we have shown [4] that several mutations in genes controlling synthesis of NMDA receptor will cause improper function of neural cells. For the test purpose, simulation of action potential generation in single neuron and typical example of neural network activity after irradiation are depicted in Fig. 6 and Fig. 7. It is demonstrated, that radiation-induced alterations in the properties of synaptic receptors cause loss of stability for specific patterns of neural network activity [18].

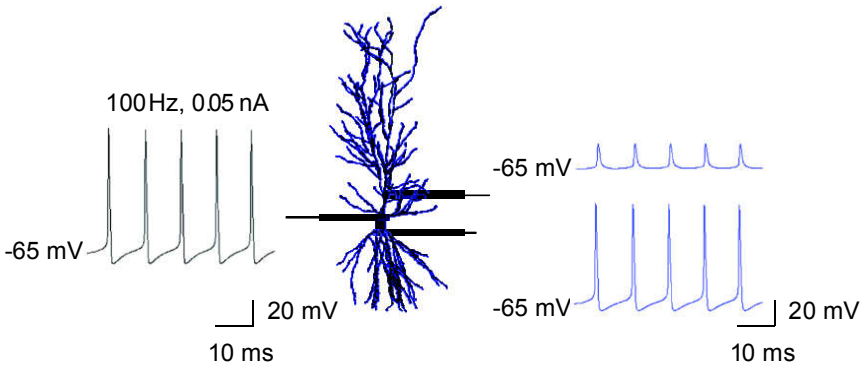

Figure 6: Action potential generation in CA1 pyramidal neuron after stimulation. The action potential is shown in soma and at points distant from the soma (left) by 50 μm (right-down) and 240 μm (right-up) of basal and apical dendrites. Individual spike frequency and membrane current are indicated for soma potential generation.

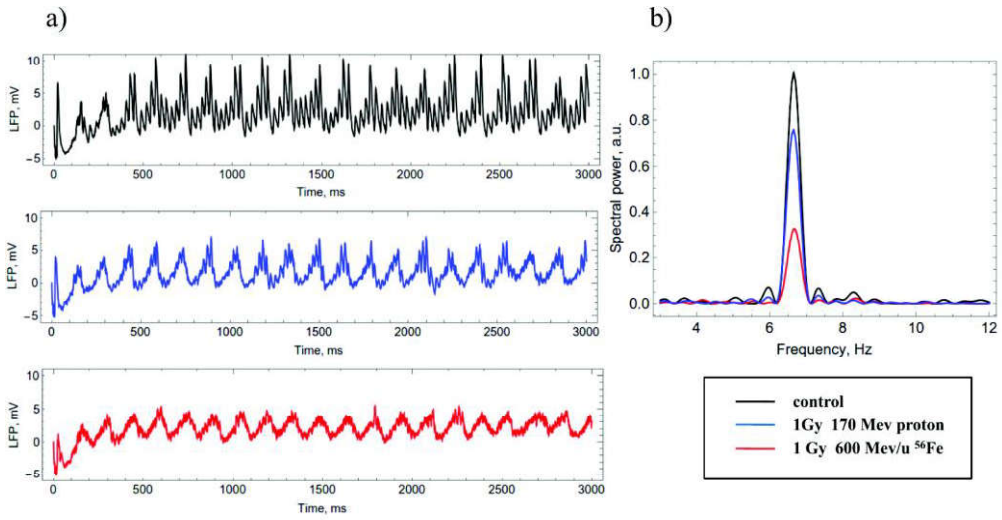

Figure 7: Local field potential (a) generated by neural network under normal conditions (black) and after irradiation of 600 MeV/u ^{56}Fe ions (red) and 170 MeV protons (blue) with doses of 1 Gy. Corresponding EEG spectra (b) are presented in low frequency band.

4. Conclusions

In the first part of this study, we simulated the rat hippocampal neurons from molecular targets to cell populations (see Fig. 1-3) with use of the Geant4/Geant4-DNA Monte Carlo radiation transport codes. Thus, we should emphasize that simulating complex geometry of biological targets with multiple elements could naively require huge amount of physical memory on modern computers. For full simulation including physical and chemical events, it would take up to several hundred gigabytes of RAM and a few hours/weeks of CPU time, that depends on the particle characteristics.

Computed energy deposition in irradiated hippocampal neurons following a track of iron ion suggests that most of the energy is accumulated by DG granular cells. Obtained quantities at the level of molecular targets also suggest that NMDA and GABA receptors belong to the most probable targets in irradiated neural cells. A sample agreement with experiment was observed for DNA DSB yields in neural cells, however, simulation results depend on many factors: 1) physical cross section of low-energy electrons in biological media; 2) chemical reaction rates and reaction radius of radicals; 3) end of radical diffusion time; 4) type of oxidative free radicals; 5) threshold values of secondary species interaction with the molecular targets; 6) geometrical description of targets, cell types, etc. Proposed simulation approach provides an insight on how can new knowledge and data from molecular, cellular and tissue models of CNS adverse changes are used to estimate CNS risks to astronauts from galactic cosmic rays during the interplanetary flight.

Acknowledgements

This work was conducted as a part of the joint research between the Laboratory of Radiation Biology of Joint Institute for Nuclear Research and the National University of Mongolia. The authors acknowledge the support from the Russian Foundation for Basic Research (grant No.17-29-01007).

References

[1] M. Durante, New challenges in high-energy particle radiobiology, *Br. J. Radiol.* 87: 0626, 2014.
[2] A. Grigor'ev, E.A Krasavin, M.A Ostrovsky, The problem of the radiation barrier during piloted interplanetary flights, *Her. Russ. Acad. Sci.* 87: 63-66, 2017.
[3] V.K. Parihar, J. Pasha, K. Katherine et al., Persistent changes in neuronal structure and synaptic plasticity caused by proton irradiation, *Brain Struct. Funct.* 220: 1161-1171, 2015.
[4] A.V. Boreyko, A.N. Bugay, T.S. Bulanova et al., Clustered DNA Double-Strand Breaks and Neuroradiobiological Effects of Accelerated Charged Particles, *Phys. Part. Nucl. Lett.* 15: 551-561, 2018.
[5] B.P. Tseng E. Giedzinski, A. Izadi et al., Functional Consequences of Radiation-Induced Oxidative Stress in Cultured Neural Stem Cells and the Brain Exposed to Charged Particle Irradiation, *Antioxid Redox Signal* 20: 1410-1422, 2014.

[6] M. Batmunkh, L. Bayarchimeg, O. Lkhagva et al., Cluster Analysis of HZE Particle Tracks as Applied to Space Radiobiology Problems, *Phys. Part. Nucl. Lett.* 10: 854-859, 2013.
[7] M. Batmunkh, O.V. Belov, L. Bayarchimeg et al., Estimation of the spatial energy deposition in CA1 pyramidal neurons under exposure to 12C and 56Fe ion beams, *J. Radiat. Res. Appl. Sci.* 8: 498-507, 2015.
[8] I.El. Naqa, P. Pater, J. Seuntjens, Monte Carlo role in radiobiological modeling of radiotherapy outcomes, *Phys. Med. Biol.* 57: R75-R97, 2012.
[9] J. Allison, K. Amako, J. Apostolakis et al., Recent developments in GEANT4, *Nuc. Inst. and Methods A* 835: 186-225, 2016.
[10] S. Incerti, I. Kyriakou, M.A. Bernal et al., Geant4-DNA example applications for track structure simulations in liquid water: a report from the Geant4-DNA Project, *Med. Phys.* 45: e722-e739, 2018.
[11] O. Belov, M. Batmunkh, S. Incerti et al., Radiation damage to neuronal cells: Simulating the energy deposition and water radiolysis in a small neural network, *Phys. Med.* 32: 1510-1520, 2016.
[12] L. Bayarchimeg, M. Batmunkh, O. Belov, et al., Simulation of radiation damage to neural cells with Geant4-DNA, *EPJ. WoC.* 173: 05005, 2018.
[13] L. Bayarchimeg, M. Batmunkh, A.N. Bugay et al., Evaluation of radiation-induced effects in membrane ion channels and receptors, *Phys. Part. Nucl. Lett.* 16: 54-62, 2019.
[14] N.T. Carnevale, M.L Hines, *The NEURON book.* New York: Cambridge University Press, p. 720, 2005.
[15] M. Machida, G. Lonart, R.A. Britten, Low (60 cGy) doses of 56Fe HZE-particle radiation lead to a persistent reduction in the glutamatergic readily releasable pool in rat hippocampal synaptosomes, *Radiat. Res.* 174: 618-623, 2010.
[16] R.A. Britten, L.K. Davis, J.S. Jewell et al., Exposure to mission relevant doses of 1 GeV/n 56Fe particles leads to impairment of attentional set-shifting performance in socially mature rats, *Radiat. Res.* 182: 292-298, 2014.
[17] R.A. Kozhina, V.N. Chausov, E.A. Kuzmina et al., Induction and repair of DNA double-strand breaks in hippocampal neurons of mice of different age after exposure to 60Co γ-rays, *EPJ WoC* 177: 06001, 2018.
[18] A.N. Bugay, Radiation induced dysfunction in the working memory performance studied by neural network modeling, *Proc. BelBI2016*, Belgrade, Serbia, 1, 18-28, 2016.

STUDY OF WHEAT BIOTIC STRESS

D. Bolormaa[1]*, S. Nansalmaa[2], S. Oyungerel[3], D. Undarmaa[4]

[1] School of Livestock and Biotechnology, MULS, Ulaanbaatar, Mongolia
[2]School of Engineering and Technology, MULS, Ulaanbaatar Mongolia
[3]School of Engineering and Applied Sciences, NUM, Ulaanbaatar Mongolia
[4]School of Agro-Ecology, MULS, Ulaanbaatar Mongolia
*E-mail: d.bolormaa@muls.edu.mn

Abstract

The current study was conducted between Jan 1st of 2017 and Jul 30th of 2018, focusing on 8 sorts of wheat (*Triticum aestivum*) commonly planted in Mongolia. *Alternaria alternata* (syn. *A.tenius*) fungus which causes black points in seed was isolated from infected seeds and grown on PDA media at 25^0C for 7 days. Spore suspensions ($1x10^4$ and $2x10^4$) were prepared from the pure culture and inoculated into leaf of the wheat. After the inoculation, the wheats were examined on day 7, 14 and 21. The leaf area, disease and aspect ratio were measured by leaf area meter (v2.3), chlorophyll index was measured by SPAD, and adaptation to Ft, QY light and dark phase was analyzed by FluorPen. As well as, seed borne disease was studied and correlation was calculated.

1. Introduction

Wheat is the main crop of the population's food strategy and some year the reduction reach for 10%-20% because of biotic stress. *Ustilago, Fusarium* and *Alternaria* are the fungus which is most influence to disease. Therefore these funguses emit very toxic proteins such as *Type A trichothecenes, Type B trichothecenes, Zearalenone, Fumonisins* and *Alternaria mycotoxins* [1].

The scientists defined that these fungus affects for human health bad, such as inhibit the immune system, create mutations, make gastrointestinal bleeding, and poison the sensory cells, also create disease such as liver cancer, brain edema and congenital defects [2]. In our country, we are conducting experimental testing on diseases of the varieties and varieties of wheat germs [1]. Therefore, it is imperative to study and diagnose cure pathogens with advanced methods and diagnosis.

2. Material and methods

Sampling: It conducted a survey on the 8-wheat-grounded, abundant and cultivated farms in the cultivated region of the Plant and Agricultural Research Institute in Darkhan-Uul aimag.
Laboratory analysis: The quality of the seed depends on 1000 seed weight, purity and germination capacity, and the quality of the seed is treated according to MNS 0246: 2010 standard. Inoculation of samples from the disease should be grown in the dark for 25 degrees in the thermostat for 7 days in a dark condition and obtained from pure culture from primary culture. The colonies and spores of the pathogen were observed by microscopes and compared with the sources of the press. Artificial infections in wheat leafs were performed by Priyanka Giri [3]. The spore solution was prepared in 1 ml of $1x10^4$ and $2x10^4$ spores, and observations were carried out for 7, 14 and 21 days. After the distillation, the chlorophyll index was measured by SPAD, Ft, QY-light and the adjustment criteria for FluorPen. The additional subsystem of the software program Data analysis identifies the parameters of the mathematical average, standard error, correlation, and statistical commands.

3. Results

Seed quality: Compared with the quality of seed varieties of the 8 varieties, Darkhan-Uul 74, Darkhan 34, Darkhan 181 and Darkhan 131 varieties - 94-90%, Orkhon, Darkhan 144 and Arvin Khalkh Rivers 1 - 89-82%. Compared to 48 hours later, compared to 48 hours after the disease, Darkhan-Uul, Darkhan-Uul 74, Darkhan-Uul, Orkhon, 72-55%, Arvin, Khalkhin-Gol 1, Darkhan-144 and Darkhan-181 -40% (Figure 1).

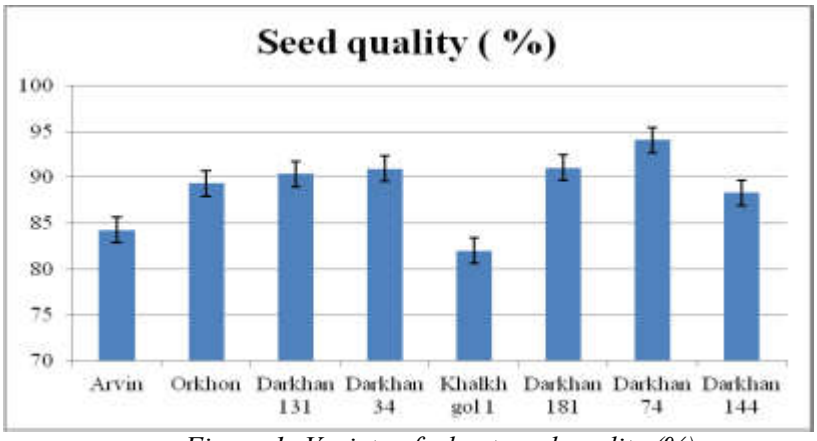

Figure 1: Variety of wheat seed quality (%).

Wheat seed borne disease and fungus: A fungus colony is a yellow-green, yellowish-yellow, fluffy, 80-90 mm diameter, fungus-shaped, sparse sponges, 6-8 chains (Figure 2, 3).

Figure 2: Wheat seed borne disease and fungus culture.

Figure 3: Alternaria`s spore.

Inoculation and wheat physiological parameters: As a result of artificial infections, Arvin, Darkhan 34, Darkhan 131 and Darkhan 181 have been infected with $1x10^4$ spores, and the symptoms have increased with time and duration. According to the leaf chlorophyll index, Khalkh rivers 1, Darkhan 144, Orkhon, Darkhan 131, Darkhan 181 varieties are 34.08-30.00, Darkhan 74, Arvin and Darkhan 34 are 27,44-24,28, while Khalkh gol major varieties are 34,00, Darkhan 144 variety 22,56-20,86, Orkhon variety 34,08-25.90, Darkhan 131 variety 17,62-14.30, Darkhan 181 variety 17,62-14.30, In Darkhan 74 variety 23,14-20,82, Arvin variety 24,70-23,68, Darkhan 34 variety 28,68-24,24. Criteria for adaptation of wheat leaf (Ft) were 1862, 20-1544,80 in control leaves and reduced to 1789,60-1375,00 in infectious leaves. The criteria for light adaptation, or QY, have been reduced to 0.75-0.72 for infecting leaves from 0.76 to 0.72 and for infected leaves (Figure 4, Table 1).

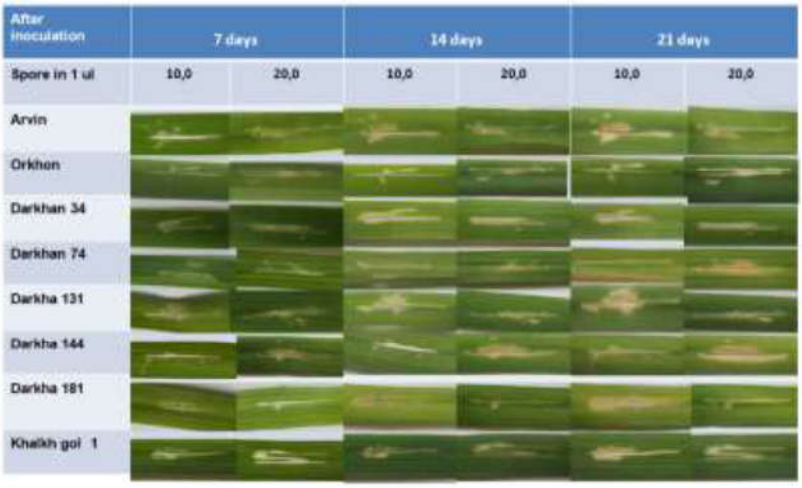

Figure 4: Inoculation after 7, 14 and 21days.

Table1: Physiological parameters of after inoculation.

№	Variety of wheat	Spore in 1 ul	Light		Dark		*Chl index*
			FT	QY	FT	QY	
			Early crop				
		Control	1650.60	0.74	1511.00	0.73	34.08
1	Khalkh gol 1	$1x10^4$	1375.00	0.75	1496.00	0.75	34.38
		$2x10^4$	1300.00	0.72	1513.00	0.73	34.38
		Control	1653.80	0.74	1722.00	0.74	30.00
2	Darkhan 131	$1x10^4$	1440.40	0.73	1395.20	0.74	17.30
		$2x10^4$	1363.20	0.74	1671.40	0.74	15.62
			Medium				
		Control	1714.60	0.76	1475.20	0.74	31.28
3	Orkhon	$1x10^4$	1321.60	0.75	1788.00	0.75	25.90
		$2x10^4$	1330.60	0.73	1331.20	0.75	34.48
		Control	1876.60	0.73	1945.20	0.74	24.28
4	Darkhan 34	$1x10^4$	2510.60	0.70	1743.20	0.70	24.24
		$2x10^4$	1638.40	0.72	1980.00	0.73	28.68
		Control	1544.80	0.75	1765.40	0.74	27.44
5	Darkhan 74	$1x10^4$	1716.60	0.71	1559.40	0.66	20.82
		$2x10^4$	1636.20	0.72	1965.40	0.73	23.14
		Control	1971.60	0.72	1791.20	0.72	25.44
6	Arvin	$1x10^4$	1829.00	0.72	1648.00	0.73	23.68
		$2x10^4$	2022.20	0.72	2027.20	0.73	24.70
			Medium late				
7	Darkhan 144	Control	1862.20	0.74	2072.40	0.72	32.50
		$1x10^4$	2668.60	0.69	2278.20	0.67	22.56
		$2x10^4$	1728.60	0.75	1769.80	0.75	20.86
		Control	1807.60	0.73	1667.60	0.73	30.00
8	Darkhan 181	$1x10^4$	1789.20	0.65	2138.00	0.67	14.30
		$2x10^4$	2871.60	0.66	3149.00	0.61	17.62

4. Discussion

1. Results of the seed quality study were "The Best Varieties of Food and Agriculture" [4] in 1000 seedlings of Darkhan, which is the highest in 74 samples, which is the result of our study. The seed laboratory's germination was the highest in Darkhan 74, Darkhan 34 and Darkhan 131.
2. Results of the disease were recorded in 7 different types of fungal diseases in the central agricultural region of our country and our study found that the *Alternaria* fungal illness was discovered [5]. The "Best Varieties of Food and Agriculture Plant" [4] and our studies have shown that Darkhan 144 and Khalkh rivers 1 variety have low illnesses with *Alternaria*.

3. The results of *Alternaria alternate= A. tenius* found in wheat seeds are comparable to the comparison of the disease pathologist morphology of Susana [6] and Pastor [7].
4. In our study, the quality of Darkhan 74 varieties was good, but the quality of the seeds of Darkhan 181 variety was high and the disease was low and resistant. Doctor of Science, Professor S. Ganbaatar [8] recorded infected by *Alternaria tenuis* seeds have overweighted.

5. Conclusions

1. Seed quality was good in Darkhan 34, Darkhan 74, Darkhan 131 and Darkhan 181 varieties, and seed disease was detected in all varieties, and Arvin, Khalkh Rivers 1, Darkhan 144 and Darkhan 181 varieties were low seed disease. Infected seeds are large and have good rates.
2. An *Alternaria* fungal morphology found in the wheat seeds was compared with the article Susana (2015) and Pastor (2015) *A.alternate = A. tenuis*.
3. Spore concentration is low, but the symptoms of the disease are rapidly deteriorating and as the symptoms increase, over time, the pathogenic fungus is aggressive, aggressive and viral.
4. The genus Arvin, Darkhan 34, Darkhan 131 and Darkhan 181 have been evaluated as vulnerable species of laryngeal disease. After the infiltration of the chlorophyll index of the plant photosynthesis process, after the infiltration index, Arvin, Darkhan 74, Darkhan 131, Darkhan 144 and Darkhan 181, the criteria for dark adaptation, or Ft, have been identified after Khalkh Gol 1, Orkhon and Darkhan 131 was reduced to Darkhan 181. As these indicators decline, plants are exposed to stress and depletion of the metabolism.

Acknowledgements

We would like to thank the Plant Science and Agricultural Institute of Mongolian University of Life sciences and Laboratory of Plant physiology in National University of Mongolia for their participation who supported our work and helped me get results of better quality.

References

[1] J. Hajslova, M. Zachariasova, T. Cajka, Analysis of Multiple Mycotoxins in Food, *Methic. Mol. Biol*. 747: 233-258, 2014.

[2] R. Köppen, M. Koch, D. Siegel, S. Merkel, R. Maul, I. Nehls, Determination of mycotoxins in foods: current state of analytical methods and limitations, *Appl. Microbiol. Biotechnol*. 86: 1595-1612, 2010.

[3] P. Giri, G. Taj, A. Kumar, Comparison of artificial inoculation methods for studying pathogenesis of Alternaria brassicae on Brassica juncea, *African J. Biotechnol.* 12: 2422-2426, 2013.

[4] *Best varieties of food and agriculture*, Ministry of Industry and Agriculture, Darkhan-Uul, Mongolia, 2013. (in Mongolian).

[5] T. Dejidmaa, B. Dondov, D. Undarmaa et al., Research on prevalence of seed cereals and seed disease, *conf. proc. Technology for Growing Crops*, Ulaanbaatar, Mongolia, 39-44, 2011. (in Mongolian)

[6] S. Brás, R. Sabino, A. Laureano et al., Cutaneous infection by different Alternaria species in a liver transplant recipient, *Medic. Mycol. Case Reports* 8: 1–4, 2015.

[7] F.J. Pastor, J. Guarro, Alternaria infections: laboratory diagnosis and relevant clinical features *Eur. J. Clin. Microbiol. Infect.* 14: 734-746, 2008.

[8] Ganbaatar S. *Wheat* Book, Published by Jargalant Harvest Co. Ltd., Mongolia, Ulaanbaatar, 2016, (in Mongolian).

PHOTO-CHEMICAL ACTIVITY IN AQUEOUS SOLUTION OF HUMAN SERUM ALBUMIN

B. Duurenbuyan*, E. Jamsranjav, D. Naidan, R. Khoroljav

Department of Biophysics, Institute of Physics and Technology, MAS, Ulaanbaatar, Mongolia
**E-mail: duurenbuyanb@mas.ac.mn*

Abstract

There are needs to know detailed mechanisms of influence of the ultra violet radiation (UV) to bio-organism and to develop effective technologies to protect from the UV due to the depletion of the ozone layer in the earth atmosphere, and increase of applications of UV sources for medical therapy and agricultural treatment etc. In this study, we focused on the basic mechanism of the influence of UV, and studied the photochemical activity induced in aqueous solution of human serum albumin (HSA) by UV irradiation. An UV source constricted with high-pressure mercury-vapor lamp (Lyumam-DRSh-250-3) and UV filter of 300-400 nm (Maximum value: 357 nm) was applied. A human serum albumin (Reanal, 01092) was chosen as the object protein based on its high probability to be influenced by UV because it propagates in whole parts of human body. An experimental method of photo-chemiluminescence was applied to explore the biochemical activities of the free radicals. At first, we explored an optimal concentration of the aqueous solution which the highest biochemical activity (the highest intensity of photo-chemiluminescence) can be observed, that is about 25%. The intensity was decreased as an exponential relation with time after irradiation, and became 10 times lower than the initial value in about 330-350 seconds after irradiation.

1. Introduction

In recent years, amount of ultraviolet radiation (UV) in human environment has been increasing due to the depletion of the ozone layer in the earth atmosphere and increase of applications of UV sources etc [1,2]. Therefore, it is essential to study the influence of UV on human health and to create effective technologies to protect human health from UV. In this study, we focused on the basic mechanism of the influence of UV, and studied the photochemical activity induced in aqueous solution of human serum albumin (HSA) by UV irradiation. Especially, we evaluated the optimal concentration of the aqueous solution which the highest photochemical activity can be observed, and analyzed structure parts of the HSA with high photochemical activities by using a photo-chemiluminescence method which is widely used to detect photochemical activity in biomaterials [3-5].

2. Materials and method

Human serum albumin (Reanal, 01092) was applied as an object, due to its high probability to be influenced by UV because it propagates in whole parts of human body [6]. In this experiment, we prepared HSA aqueous solutions with 8 different concentrations from 1% to 300%. We also added Eosin-dye (Reanal, 03056) as a UV sensitizer and it`s concentration was adjusted to 5% [7].

Then we have irradiated HSA aqueous solutions after photo-chemiluminescence spectrum detected by photofluerometer. The photofluerometer was installed at Institute of Physics and Technology, Mongolian Academy of Science by D. Naidan (Sc.D) and R. Khoroljav (Ph.D). A scheme of photofluerometer is shown in Fig 1.

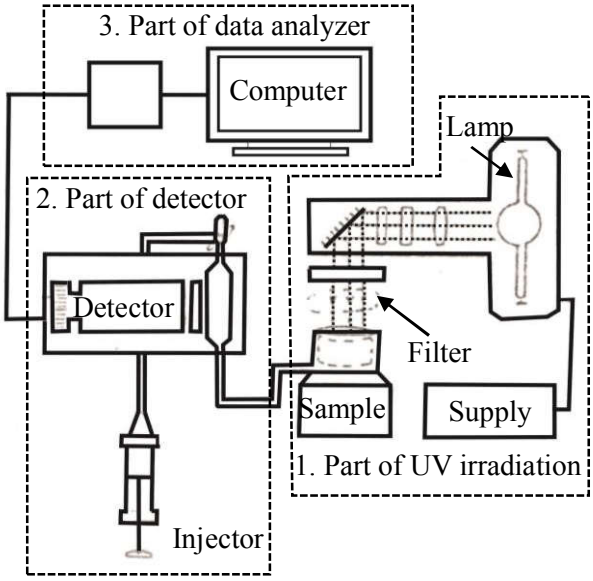

Figure 1: Scheme of photofluerometer. 1.Part of UV irradiation 2. Part of detector 3. Part of data analyzer.

We used high-pressure mercury-vapor lamp for UV and visible light in wavelength region of 200-700 nm. The UV was separated by UF-8 filter of which transmittance is in a UV with wavelength of 300-400 nm. The transmittance spectrum is shown in Fig 2.

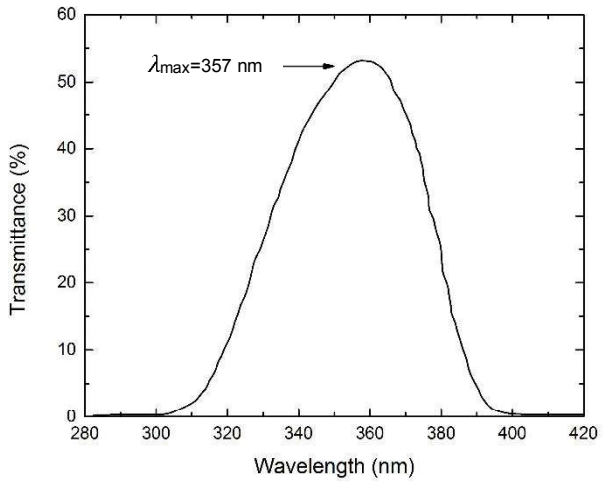

Figure 2: Transmittance of UF-8 filter.

The horizontal and vertical axes of the Fig 2 are wavelength (nm) and transmittance (%) of UV, respectively. Maximum value of the transmittance was at a wavelength of 357 nm.

Irradiation was performed for 30 seconds for all of the samples. The irradiated samples were injected to detector (Photo-electron multiplier M11 FVS300) and the photo-chemiluminescense spectrum was detected as a relation between luminescence intensity and elapsed time after irradiation.

3. Results and discussion

In the beginning, we compared the photo-chemiluminescence intensities of the HSA aqueous solutions with 8 different concentrations from 1% to 300 %. A result is shown in Fig 3 as a relation between the concentration and the intensity.

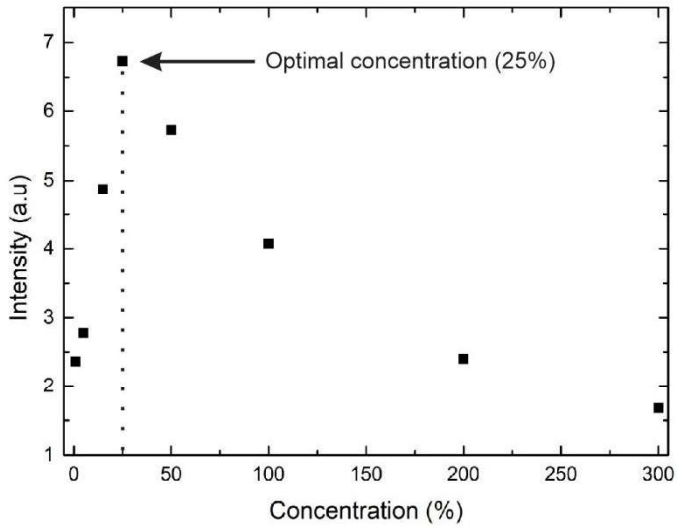

Figure 3: Relation between maximum intensity in photo-chemiluminescence spectrum and concentration of HSA aqueous solutions with 8 different concentrations.

At low concentration, the intensity is rapidly increased when the concentration increases. However, the intensity is slowly decreased at high concentration which is higher than 25%. In otherwise, the highest value of photo-chemiluminescence of the HSA was observed at a concentration of 25% (optimal concentration).

After that, we analyzed a photo-chemiluminescence spectrum of the HSA aqueous solution with a concentration of 25%. The spectrum is shown in Fig 4.

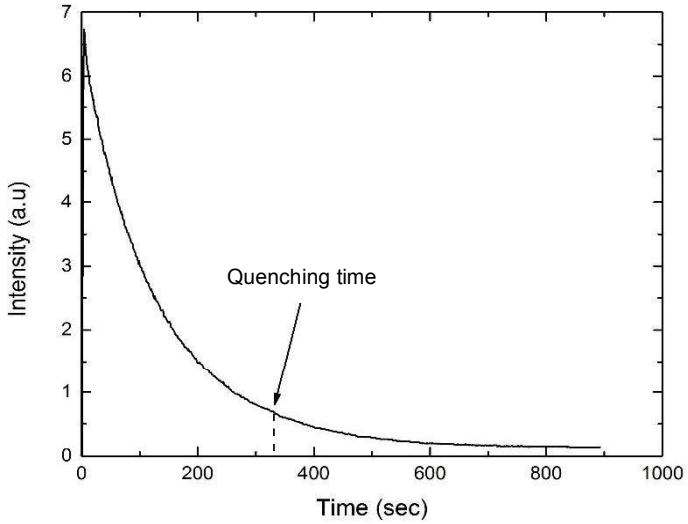

Figure 4: Photo-chemiluminescence spectrum of aqueous solution of HSA.

In Fig 4, horizontal axis is time and vertical axis is intensity of photo-chemiluminescence. Intensity of photo-chemiluminescence was decreased as an exponential relation with time after irradiation. A result of logarithm anamorphosis analyses [8] showed that the relation is expressed as sum of 2 exponential functions. Graphics of the functions are illustrated in Fig 5. The quenching time which the intensity becomes 10 times lower than its initial value, was also evaluated by using the data of 3 experiments. The result showed that is 330-350 seconds.

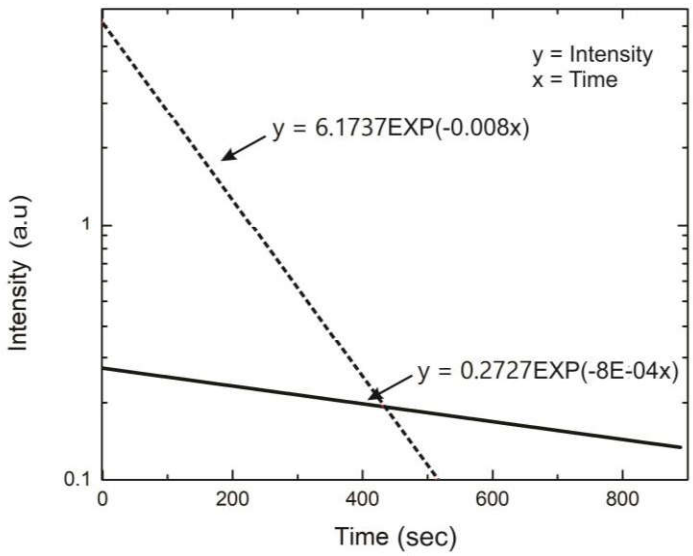

Figure 5: Logarithm anamorphosis analysis for photo-chemiluminescence spectrum of HSA.

The broken line and solid line were drawn with the fast decreasing and slow decreasing functions, respectively. This fast decreasing function was same with that of the tryptophan amino-acid which is existed in the HSA structure [8]. Therefore, it is considered that this luminescence spectrum is illuminated from a new product resulted with interaction between the tryptophan amino-acid and free radicals. The slow decreasing function of the HSA was also same with that of the bovine serum albumin (BSA) [8]. However, which product illuminates this spectrum, is still unknown.

4. Conclusions

We analyzed photo-chemiluminescence spectrum of HSA aqueous solutions with 8 different concentrations from 1% to 300%. At low concentration, intensity of the photo-chemiluminescence spectrum was rapidly increased when the concentration increases. However, the intensity was slowly decreased at high concentration which is higher than 25%. The intensity of photo-chemiluminescence was also decreased as an exponential relation with time after irradiation and became 10 times lower than initial value at 330-350 second. The relation was described as a sum of fast and slow decreasing exponential functions. The fast decreasing function was same with that of the tryptophan amino-acid. However, which product illuminates slow decreasing spectrum, is still unknown. It will be next task of our study.

References

[1] WMO: Scientific Assessment of Ozone Depletion - 2010, *Report* 52: 438, 2011.

[2] M. Shih, Emerging applications for UV leds drive broad interest, *LED's magazine* 83: 19-22, 2015.

[3] Z. Wang, Z. Song, D. Chen, Study on the binding behavior of bovine serum albumin with cephalosporin analogues by chemiluminescence method, *Talanta* 83: 312-319, 2010.

[4] X. Tan, Z. Song, D. Chen et al., Study of the chemiluminescence behavior of bovine serum albumin with luminol and its analytical application, *Spectrochim Acta A* 79: 232-235, 2011.

[5] D. Naidan, I. Sapenzhinskii, Photochemoluminescence of tryptophan-containing peptides and proteins during photooxidation. VII. Mechanism of sensitization by eosin of the photochemiluminescence of human serum albumin solutions, *Biofizika* 22: 571-575, 1977.

[6] P. Lee and W. Xiaoyang, Modifications of Human Serum Albumin and Their binding Effec*, Curr. Pharm. Des*. 21: 1862-1865, 2015.

[7] R. Khoroljav, D. Naidan, J. Erdenetogtokh., Sonochemiluminescence of Protein and Dyes in Ozone or Argon Envaironment, *Proc. of Annual Meeting of the Mongolian Academy of Sciences* 35: 71-78, 2008. (in Mongolian)

[8] D.Naidan, *Study of sensitized photochemiluminescence of peptide and protein solution*, Science doctoral dissertation, Ulaanbaatar, Mongolia 2001. (in Russian and Mongolian)

HYDROGEN ATOM IONIZATION IN FEMTOSECOND LASER FIELD: NUMERICAL SOLUTION OF THE TDSE USING CWFDVR METHOD

Ch. Aldarmaa*, L. Khenmedekh, G. Zorigt

Physics Department, School of Applied Sciences, University of Sciences and Technology (MUST), Mongolia
**E-mail: aldaraa2004@yahoo.com*

Abstract

We present an discrete variable representation for solving the time-dependent Schrodinger equation for an atomic system interacting with an intense laser pulse. Instead of the usual finite difference (FD) method, the radial coordinate is discretized using the discrete variable representation (DVR) constructed from Coulomb wave functions. Our results are in excellent agreement with other accurate theoretical calculations using different methods.

1. Introduction

The study multiphoton ionization of atom by femtosecond laser pulse is a subject of interest for both experiments and theory. One way to describe such process is numerical solution of the time dependent Schrodinger equation (TDSE). "Exact" solution of TDSE with minimal computational effort still remain challenge for researchers. Different numerical methods for solution of TDSE are tested and give promising results. Among them should be emphasized the generalized pseudospectral method (GPSM) of Shih I Chu and coworkers [1-3], and matrix- iterative method of Grum Grzhimailo et al [4]. The former method based on Crank-Nicholson approximation of TDSE, gives most accurate results for ejected electron spectrum. The GPSM attractive in that, it uses the "exact" integration of TDSE by split operator method, discretizing differential operators on the pseudospectral Legendre basis, not only avoiding the Coulomb singularity, but also uses several times less, non uniform radial grid nodes, which make this method computationally more effective. The limitation of this method is the Legendre basis doesn't possess correct asymptotic behavior. Peng and Starace[5] developed Coulomb wave function disrete variable representation method (CWFDVR) for solution of TDSE for an atom in intense laser field. In comparision with the GPSM, the basis has correct Coulomb wave asymptotic form. In this paper, we propose Coulomb wave function discrete variable representation method to solve the TDSE.

2. Theory

We solved the time-dependent Schrodinger equation (TDSE) for atomic hydrogen in an intense laser field to calculate electron energy spectra with the hydrogen atom initially in the ground state. The Schrodinger equation for atomic hydrogen in the presence of linearly polarized fields $\vec{E}(t)$ can be written as (in atomic units)

$$i\frac{\partial\Psi(\vec{r},t)}{\partial t} = \hat{H}\Psi(\vec{r},t) = \left[\hat{H}_0 + \hat{V}(\vec{r},t)\right]\Psi(\vec{r},t). \quad (1)$$

Here $\hat{H}_0$ is the unperturbed H atom Hamiltonian and $\hat{V}$ is the atom-field interaction:

$$\hat{H}_0 = -\frac{1}{2}\frac{d^2}{dr^2} + \frac{\hat{L}^2}{2r^2} - \frac{1}{r} \quad \text{and} \quad V(\vec{r},t) = \vec{p}\cdot\vec{A}(t). \quad (2)$$

A linearly polarized laser field is used in the calculation. One can choose pulse shape either for $\vec{A}(t)$ or for $\vec{E}(t)$. Grum Grzhimailo et al pointed out that the photoelectron spectrum depends on, which of these two vectors have a sin^2 pulse shape. If we choose for example

$$\vec{E}(t) = E_0 sin(\omega t + \varphi) sin^2\left(\frac{\pi t}{\tau}\right), \qquad 0 \le t \le \tau, \quad (3)$$

the shape of the $A(t)$ determined by integration:

$$A(t) = -\int_0^t E(t)dt = \frac{1}{4}E_0\left(-\frac{2\cos[\phi 0]\cos[\omega t]}{\omega} + \frac{\tau\cos\left[\frac{2\pi t}{\tau}-\phi 0-\omega t\right]}{-2\pi+\tau\omega} + \frac{\tau\cos\left[\frac{2\pi t}{\tau}+\phi 0+\omega t\right]}{2\pi+\tau\omega} + \frac{2\sin[\phi 0]\sin[\omega t]}{\omega}\right) \quad (4)$$

Otherwise, we can choose

$$A(t) = A_0 cos(\omega t + \varphi) sin^2\left(\frac{\pi t}{\tau}\right) \quad (5)$$

We shall extend the second-order split-operator technique in spherical coordinates for the time propagation of the Schrodinger equation:

$$\Psi(\vec{r}, t+\Delta t) \cong \exp\left(-i\hat{V}(\vec{r}, t+\Delta t)\frac{\Delta t}{2}\right) \times exp\left(i\hat{H}_0\Delta t\right) \times exp\left(-i\hat{V}(\vec{r}, t)\frac{\Delta t}{2}\right)\Psi(\vec{r}, t) + O(t^3) \quad (6)$$

To pursue the time propagation, we expand the total wavefunction $\Psi(\vec{r}, t)$ in Legendre polynominals:

$$\Psi(r_i, \theta_j, t) = \sum_{l=0}^{l_{max}} g_l(r_i)\, P_l(cos\theta_j) \quad (7)$$

where the P_l s are the normalized Legendre polynomails. $g_l(r_i, t)$ can determined accurately by the Gauss-Legendre quadrature

$$g_l(r_i) = \sum_{k=1}^{l_{max}} w_k\, P_l(cos\theta_k)\Psi(r_i, \theta_k, t) \quad (8)$$

Where $(cos\theta_k)$ are the L+1 zeros of the Legendre polynomial $P_{L+1}(cos\theta_k)$ and w_k are the corresponding quadrature weights. The present method discretizes the radial coordinate using the discrete variable representation CWFDVR constructed from the positive energy Coulomb wave function.

3. Results and discussions

TDSE for hydrogen atom in femtosecond laser field solved wth the CWFDVR in three cases: A. 2-cycle laser pulse with the peak intensity I = $10^{15} W/cm^2$ and central frequency of $\omega = 0.2$, (first column of Fig.1) B. 4-cycle laser pulse with the peak intensity I = $10^{15} W/cm^2$ and central frequency of $\omega = 0.3$ (second column of Fig.1),C. 20-cycle laser pulse with the peak intensity I = $10^{14} W/cm^2$ and central frequency of $\omega = 0.114\,3$ (third column of Fig.1). As seen from the Fig.1, in the first two cases (A and B), the pulse shape given by (4), doesn't fit not only envelope but also carrier shape of (5), so the corresponding electron spectrums are different from each other. But in the case C, formular (4) and (5) give nearly same shape for *A(t)*. Our results B and C in agreement with the [2].

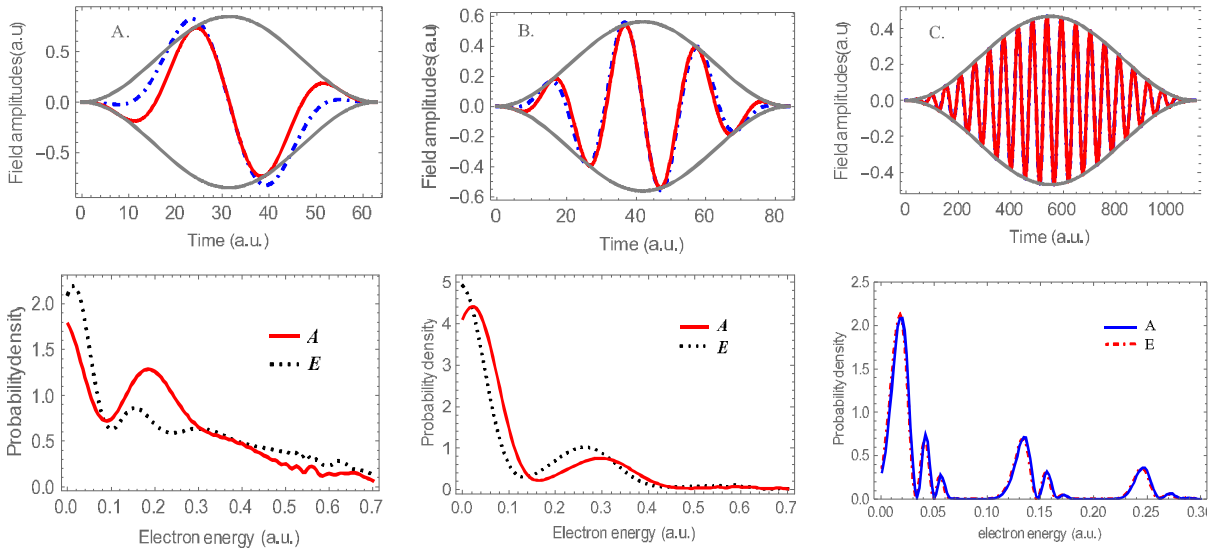

*Figure 1. First row Laser pulse with a sin² envelope. Second row Ionization of atomic hydrogen in **A**. 2 cycle, a peak intensity of* $10^{15}W/cm^2$*, and central frequency of 0.2 a.u, corresponding to a wavelength of 227.75 nm. **B**. 4 cycle laser pulse with a sin² envelope, a peak intensity of* $10^{15}W/cm^2$*, and central frequency of 0.3 a.u, corresponding to a wavelength of 151.84 nm. **C**. 20 cycle laser pulse with a sin² envelope for the electric field, a peak intensity of* $10^{14}W/cm^2$*, and central frequency of 0.114a.u, corresponding to a wavelength of 399.57nm. The calculations were performed with angular momenta up to* $l = 10$ *in the velocity form of the electric dipole operator.*

4. Conclusions

We apply the CWFDVR method to the ionization of atomic hydrogen by an intense laser field. In the case of central frequency of 0.3 and 0.114, our results are in excellent agreement with other accurate theoretical calculations using different methods. The choice of sin² envelope for *E(t)* gives an *A(t)* which is different in shape from *A(t)* with sin² envelope, especially for short pulses.

References

[1] X.M. Tong, S.I. Chu, Theoretical study of multiple high order harmonic generation by intense ultrashort pulsed laser fields: A new generalized pseudospectral time–dependent method, *Chem. Phys*, 217, 119-130, 1997

[2] D.A. Telnov, S.I. Chu, Above-threshold-ionzation spectra from the core region of time-dependent wave packet: An *ab* initio time dependent approach, *Phys. Rev.,* 79, 043421, 2009

[3] Q. Li, X.M. Tong, T. Morishita, et al., Fine structures in the intensity dependence of excitation and ionization probabilities of hydrogen atoms in intense 800 nm laser pulses, *Phys. Rev.,* 89, 023421, 2014

[4] A.N. Grum-Grzhimailo, B. Abeln, K. Barschat et al., Ionization of atomic hydrogen in strong infrared laser field, *Phys. Rev*., 81, 043408, 2010

[5] L.Y. Peng, A.F. Starace, Application of Coulomb wave function discrete variable representation to atomic systems in strong laser fields, *J. Chem. Phys.,* 125, 154311, 2006

STUDY OF CRYSTAL STRUCTURE OF NATURAL QUARTZ

B. Khongorzul*, S. Tengis, S. Saran, D. Sangaa

Institute of Physics and Technology, Mongolian Academy of Science, Ulaanbaatar – 13330, Mongolia
**E-mail: hongoroob72@gmail.com*

Abstract

In this study, three different natural quartz samples (rock quartz, smoky and mixed quartz) have been investigated using the first-principles method within the framework density functioanal theory (DFT) with on site correction for Coulumb interaction (GGA+U+J_0). We have investigated crystal structure and structure distortion of quartz samples using the X-ray diffraction method. Crystalize size, crystal lattice parameters and micro-strain were calculated using Fullprof-suite program within the framework Rietveld method. The differences observed in different quartz samples are presumably due to the nature of defects. Then we have performed SEM and FT-IR measurements of natural quartz samples.

Key words: Quartz, X-ray diffraction, SEM, FT-IR, DFT

1. Introduction

Quartz (low-temperature α-quartz) is one of the most abundant minerals and the most important silica mineral, occurring in rocks; therefore the knowledge of the properties is important for mineralogical investigations. a common and widely studied mineral. Moreover, the study of quartz as well as of other silica modifications has numerous practical applications: in mineral exploration, materials sciences and nuclear waste disposal, but also in anthropology and archaeometry. Silicon dioxide or silica is well known for its hardness and exists in various crystalline as well as amorphous forms. Most of its crystalline forms consists of tetrahedral SiO_2 units [1]. The crystal structures of the α (low) and α (high) phases were first deduced in the 1920s by Braggs and Gibbs. Since their pioneering work, many studies have been carried out to the structural models further using both neutron and x-ray single crystal diffraction [2]. From a technological point of view, silica is widely used in different fields such as microelectronic industry (for metal-oxide-semiconductor devices), optical fiber technologies, and nanoimprint lithograpy [3].

Both naturally and synthetic quartz SiO_2 have stimulated a long history of experimental and theoretical investigation [4]. We have studied three different types of natural quartz; a rock quartz crystal (Fig 1a), that originated from Altai soum of Khovd province and two smoky quartz crystals (Fig1b and Fig1c) that were sampled at the Terelj river – near Ulaanbaatar.

Figure 1: a/Rock, b/Smoky and c/Mixed crystal of natural quartz.

2. DFT (Density Functional Theory) calculation

The basis concepts of density functional theory (DFT) and the principles of its application to pseudo-potential plane wave calculations have been extensively studied; and DFT method is now well established and has been successfully applied to the study of a wide range of materials. We have employed established density functional theory (DFT) methods, which generally achieve a good balance between the accuracy and computational expense, to study the structure of different rock, smoky and mixed crystal of the trigonal SiO_2 phase. We have shown crystal structure of SiO2 in the Figure 4. The calculations on the pseudo-potential plane wave self - consistent field (PWscf) method were performed using the generalized gradient

approximation (GGA) by Perdew and Wang (PW91) [5] within the frame-work of DFT, as implemented in the QUANTUM ESPRESSO package. It employs ultra-soft pseudo-potentials for the effective interaction of the valence electrons with the atomic cores [6].

The following electronic states are treated as valence states: O($2s^2$,$2p^4$) and Si($3S^2$,$3P^2$). The wave functions are expressed as plane waves up to a kinetic energy cutoff of 20 Ry and the kinetic energy cutoff for charge density and potential is chosen by 150 Ry. Three dimensional Fast Fourier Transform (FFT) meshes for charge density, scf potential and wavefunction FFT and smooth part of charge density are chosen to be (70 x 70 x 70) grids. There might be need to use finer k – points meshes for a better evaluation of on - site occupations due the strong correlated system. The summation of charge densities is carried out using the special k - points restricted by the (2 x 2 x 2) grids of Monkhorst - Pack scheme due to the computer power ability. To obtain optimized atomic structures, ionic positions and lattice parameters are fully relaxed until the residual forces are less than 0.05 eV/°A for each atom. The occupation numbers of electrons are expressed Gaussian distribution function with an electronic temperature of kT = 0.02 Ry. The mixing mode of charge density is chosen to be local density dependent Tomas - Fermi (TF) screening for highly inhomogeneous systems. The generalized eigenvalue problem is solved by the iterative diagonalization using the conjugate gradient (CG) minimization technique, and the starting wave function is chosen from superposition of atomic orbitals plus a superimposed ”randomization” of atomic orbitals in all our calculation. By the static MFT we used the extended Hubbard based Hamiltonian including the effective magnetic exchange interaction parameter J_0 and the on - site Coulomb interaction is chosen to be U = 7.5eV using the simplified rotational invariant formulation based on the linear response method [7]. The Hubbard parameter, which is used to the perturbation to compute J_0 with the linear response method, is chosen to be 3eV. Atomic wave functions used 3 for GGA + U + J_0 projector are not orthogonalized. Then we calculated number of lattice parameter 9.2863 a.u, new unit cell volume 762.9417 $a.u^3$, density 2.648 g/cm^3, final energy 215.4716 Ry, total force 0.00149 and total energy -215.4716 Ry for natural rock crystal. The results for the smoky and mixed crystal are more less straightforward than for rock quartz crystal due to the higher structural adjustment of smoky and mixed crystals compared to the rock crystal.

The crystal structure of rock quartz was drawn using Vesta software. The Si (Silicon) atom is shown as blue and O(Oxygen) as red balls, respectively (Fig 2).

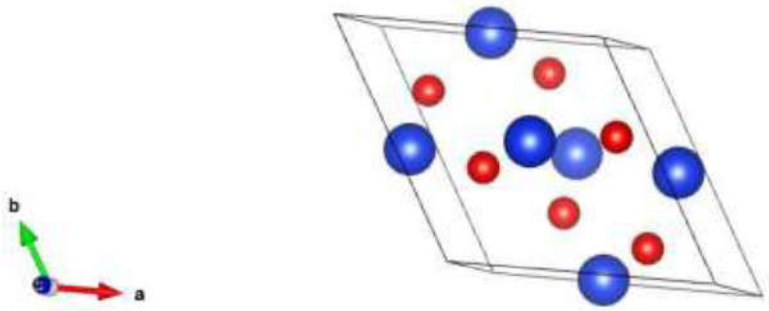

Figure 2: Crystal structure of Rock crystal.

3. XRD (X-Ray Diffractometer) calculation

We have performed crystal structure investigation by X-ray powder diffraction (Shimadzu (MAXima_X XRD-7000)) with $CuK\alpha(\lambda = 1.5406A^0)$ radiation in the diffraction angle of 2ϑ from 10 to 90^0at scan rate of $0.02s^{-1}$. In this work we used the Rietveldt method within the framework of X-ray diffraction as implemented in the Fullprof-suite package. This program is a powerfull tool to study the crystal structure and magnetic structure treatment of neutron and x-ray diffraction spectrum. The Rietveldt method refines user-selected parameters to minimize the difference between an experimental pattern (observed data) and a model based on the hypothesized crystal structure and instrumental parameters (calculated pattern).

$$S_y = \sum_i w_i (y_i - y_{ci})^2 \quad (1)$$

y_i- observed intensity at the i^{th} step, y_{ci}- calculated intensity at the i^{th} step

Table 1: Crystal structural parameters after treatment by Rietveldt method of rock crystal, smoky crystal and mixed crystal of natural.

		Rock crystal	Smoky crystal	Mixed crystal
Si	x/a	0.47029	0.4650	0.47188
	y/b	0.00000	0.0000	0.00000
	z/c	0.33333	0.3333	0.33330
O	x/a	0.41113	0.41174	0.39518
	y/b	0.26804	0.25843	0.28204
	z/c	0.22200	0.22374	0.20858
	α, β	90	90	90
	γ	120	120	120
	Occ(Si)	0.5	0.5	0.5
	Occ(O)	1	1	1
	Biso(Si)	0.46362	2.23176	6.70412
	Biso(O)	0.51360	3.30857	0.00000
Lattice	a, b[Å]	4.91244	4.91323	4.914104
const	c[Å]	5.404171	5.40439	5.405885

Table 2: R factors after treatment by Rietveldt method of rock crystal, smoky crystal and mixed crystal of natural.

	Rock crystal	Smoky crystal	Mixed crystal
R_p	14.0	18.3	24.1
R_{wp}	16.1	23.7	31.9
R_{exp}	5.4	5.65	4.95
RF	5.77	9.40	17.0
$Bragg - R$	6.24	9.18	14.8

XRD patterns of the natural rock quartz, smoky and mixed quartz crystals are shown in the Figures 3 to 5.

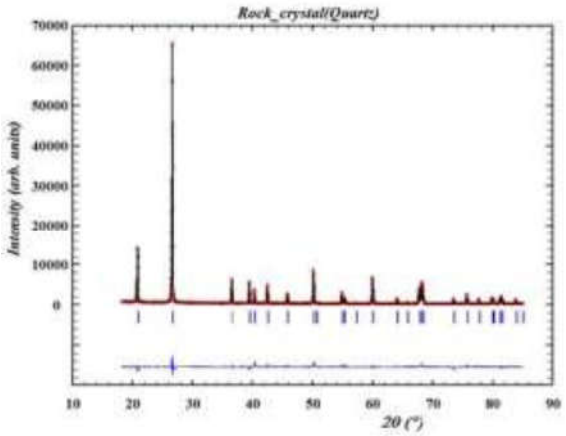

Figure 3: X-ray diffragtogramm of natural rock crystal.

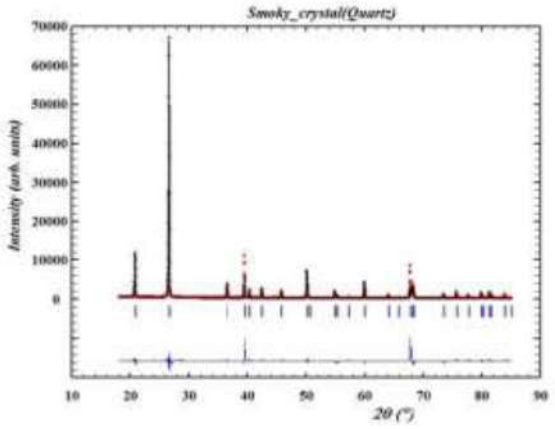

Figure 4: X-ray diffragtogramm of natural smoky crystal.

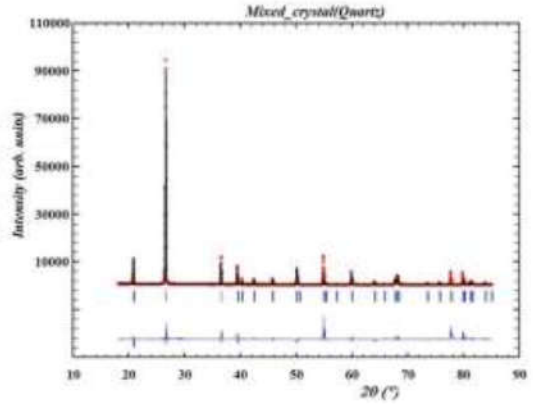

Figure 5: X-ray diffragtogramm of natural mixed crystal.

4. SEM-EDX measurement

SEM provides detailed high resolution images of the sample by rastering a focused electron beam across the surface and detecting secondary or backscattered electron signal.

The composition of elements carried out by SEM-EDX measurement for natural smoky quartz. Smoky quartz weight percentage ratio is 7.3% (Silicon) and 92.7% (Iron). The SEM image of natural smoky quartz shown in Fig 6. The detailed analysis of a spot in crystal showed the presence of iron see Fig 7.

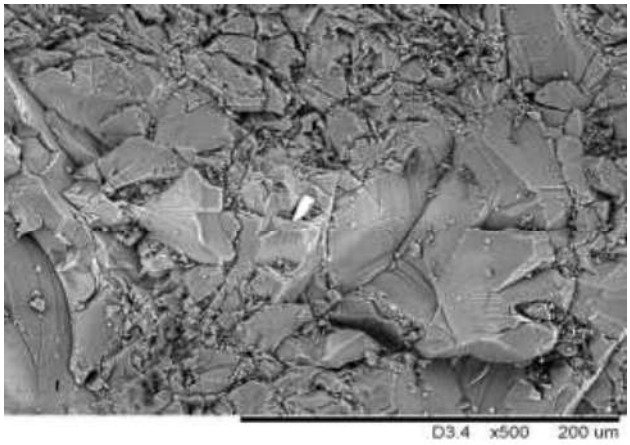

Figure 6: The SEM image of natural smoky quartz.

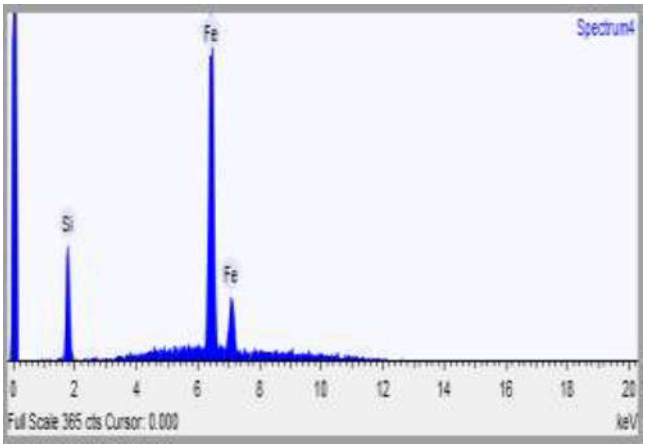

Figure 7: The detailed analysis of a spot in crystal showed the presence of iron.

5. FT-IR measurements

In this section demonstrates the Fourier Transform Infrared(FTIR)][8] spectroscopic characterization of natural rock, smoky and mixed quartzs. FT-IR spectra were recorded for all samples in range of 4000cm^{-1} to 500 cm^{-1} on Shimadzu IR-Prestige 21 spectrometer.

The absorption bands at 695.37, 778.31, 797.6 and 1080cm^{-1} are due quartz at 1609.67 and 3446.94 cm^{-1} due on deformation of water. The latter we observed only for smoky and mixed quartz (Fig 8).

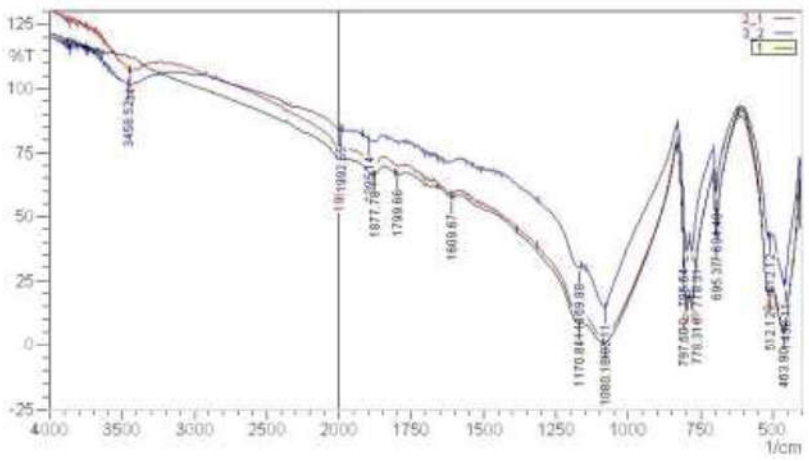

Figure 8: FT-IR spectra of natural rock, smoky and mixed quartzs.

6. Conclusion

DFT calculations have been employed to study the structures and resulted in the calculation of the lattice parameter and new unit cell volume calculation of natural rock crystal, respectively. However, due to the higher structural adjustment of smoky and mixed quartz crystals, the Density Functional Theory calculations were less straightforward.

Furthermore, the crystal structure parameters of natural rock quartz crystal, and smoky quartz crystals were determined by X-ray diffractometer. Our calculations show that the crystal structural parameters of smoky and mixed crystal are more different than those of rock crystal. This difference, between rock quartz and smoky quartz, provides additional evidence that the nature of the original crystals affects the formation of defects; one plausible explanation is the presence of water and the adsorption of water in the smoky quartz.

References

[1] S. Sharma, B.G. Pollet, Support materials for PEMFC and DMFC electrocatalysts, *Journal of Power Sources*, 208: 96-119, 2012.

[2] S. Coh, D. Vanderbilt, Structural stability and lattice dynamics of SiO_2 cristobalite, *Physics Review B*, 78: 054117, 2008.

[3] L.M. Samos, G. Bussi, A. Ruini et al., SiO_2 in Density Functional Theory and Beyond, *Bas. Sol. State Phys.* 248: 201-210, 2011.

[4] Y. Pan, M.J. Nilges, R.I. Mashkovtsev, Radiation-induced defects in quartz: a multifrequency EFR study and DFT modeling of new peroxy radicals, *Mineralog. Magaz.* 73: 519-535, 2009.

[5] J.P. Perdew, J.A. Chevary, S.H. Vosko et al., Electronic structure: wide-band and strongly correlated systems, *Phys. Rev. B* 46: 6671, 1992.

[6] D. Vanderbilt, Soft self-consistent pseudopotentials in a generalized eigenvalue formalism, *Phys. Rev*, 41: 7892, 1990.

[7] M. Cococcioni, S. Gironcoli, Linear response approach to the calculation of the effective interaction parameters in the LDA+U method, *Phys. Rev*, 71: 035105, 2005.

[8] F.B. Rieg, J.V.G. Adelatado, FTIR quantitative analysis of calcium carbonate(calcite) and silica(quartz) mixtures using the constant ratio method, Application to geological samples, *Talanta* 58: 811-821, 2002.

A STUDY OF CRYSTAL STRUCTURE AND PARTICLE SIZE OF PEROVSKITE TYPE $La_{1-x}Cu_xMnO_{3+\delta}$(x≤0.1) COMPOUNDS SUSPENDED IN WATER

G. Oyungerel[1]*, G. Batdemberel[2], D. Sangaa[3]

[1]School of Mathematics and Natural Sciences, Mongolian State University of Education, Ulaanbaatar, Mongolia
[2]School of Applied Sciences, Mongolian University of Science and Technology,
P.O.Box 46/520, Ulaanbaatar, Mongolia
[3]Institute of Physics and Technology, Mongolian Academy of Sciences
*Email: gerel0124@gmail.com

Abstract

Nanosized $La_{1-x}Cu_xMnO_{3+\delta}$ (x≤0.1) was synthesized at different temperatures by using heteronuclear complexing method. X-ray diffraction analysis show that sample consists of two phases: $La_{1-x}Cu_xMnO_{3+\delta}$ (x≤0.1) having $R\bar{3}c$ space group with rhombohedral symmetrical structure and $La_2Cu_2O_5$ having C2/c space group with monoclinic symmetrical structure. The results show the quantity of $La_{1-x}Cu_xMnO_{3+\delta}$ increase from 91.22 to 97.62%, while quantity of $La_2Cu_2O_5$ compound decrease from 8.78 to 2.37% with rising of calcination temperature from 500^0C to 900^0C. The Photon Cross Correlation Spectroscopy (PCCS) was used to measure size distribution. The results reveal that particle mean diameter increases from (276±4) to (455±5)nm, particle specific surface area (Sv) decreases from 21.84 to 13.29 m^2/sm^3, particle size distribution equals to 55-761nm and particle surface and volume mean diameter (SMD,VMD) increase from 247 to 459nm.

Keywords: Nanosized $La_{1-x}Cu_xMnO_{3+\delta}$; Perovskite oxide; Amorphous heteronuclear complex; Photon cross correlation spectroscopy (PCCS); Particle size.

1. Introduction

Perovskite type oxides ($La_{1-x}M_xMnO_3$, M-Ce, Sr, Pr, Eu, Nd) have been widely studied in various applications including catalysis [1-3], electrodes for fuel cells and superconductor [1-6]. In perovskite type oxides, substitution of A and/or B-site cations by foreign metal cations brings about modification of catalytic properties. Many recent studies have focused on the effects of A-site substitution on the catalytic properties [1, 7-11]. $La_{1-x}M_x\ MnO_3$ (M-Ce, Sr, Pr, Eu, Nd) compounds exhibit fairly good activity for CO, methane combustion and resistance SO_2 poisoning [12-15]. Based on the literature review the perovskite type oxides are mostly synthesized by ceramic [16], coprecipitation [17], spray drying [18], freeze drying [19] and amorphous citrate methods [20-21]. It is reported that the different preparation could cause the variations of the structured defects of perovskite, resulting in different performance of the catalysts. A good chemical homogeneity of perovskites can be obtained by the freeze drying and amorphous citrate methods. Among them, the amorphous complexing method is very important for synthesis of the perovskite catalysts, due to low formation temperature of perovskites and low cost of the preparation. In this work $La_{1-x}Cu_xMnO_{3+\delta}$ (x≤0.1) powder was synthesized by using an amorphous heteronuclear complexing method. X-ray phase analysis of samples was done. The main attention is paid to determination of size distribution of nano-sized $La_{1-x}Cu_xMnO_{3+\delta}$ (x≤0.1) perovskite oxide.

2. Experimental techniques

2.1. Preparation of La1-xCuxMnO3+δ (x≤0.1) powder

The $La_{1-x}Cu_xMnO_{3+\delta}$ (x≤0.1) oxides were obtained by decomposing the precursor in air. Initially, the temperature was raised to 500^0C at a slow heating rate (5-60^0C/min). The sample was then kept at this temperature for 90 min to promote the decomposition of organic components. Finally, the temperature increased to various pre-set (T=600, 700, 800 and 900^0C) temperatures and kept stable for definite period of time to allow for the formation of perovskite type oxides.

2.2. Preparation of La1-xCuxMnO3(x≤0.1) suspension

For the preparation of $La_{1-x}Cu_xMnO_3$ (x≤0.1) homogeneous suspension Ultrasonic Cell Disruptor KS-900F (voltage 230W/50Hz, impulse 30%, amplitude 50%) was used. An aqueous power solution was prepared by dissolving powder granulas (0.0207gr) in water (60ml) under continuous stirring. After dissolving powder a small amount of $Na_2P_2O_7$ solution was added to make a stable suspension. Then samples were sonicated for 10 min. Suspension was diluted again (20 ml of suspension +60ml of water). This dilution is suitable for trigger condition with a count rate in 1200kcps.

2.3. XRD measurement

XRD measurements were carried out at ambient conditions on a (Enraf Nonius Delft) powder diffractometer. A step size was 0.02^0, integration time was 3 s per step and scan range was $5\text{-}60^0$. Phase analysis was done by <<X'Pert HighScore Plus>> program [22]. X-ray spectra were refined using the program FULLPROF [23].

2.4. Particle size distribution analysis

Particle size and size distribution analysis of suspensions was done on Photon Correlation Spectroscopy PCCS (Sympatec GmbH, Germany). Samples are put into transparent cuvette (Eppendorf Uvette®, Sympatec Item No.NZ0020) with dimensions 12.5x12.5x3.6mm, volume of 50-2000µl. Then cuvette is placed in thermostat bath with filled clean water filtered by 022µm filter. It has to be orthogonal to the incoming laser beam with 632.8nm wavelength. The water level should be 3/4 of the bath height. The data was calculated by WINDOX 5. Windox 5 supports all Laser Diffraction, Image Analysis, Photon Cross-correlation and Ultrasonic Extinction sensors and peripherals for or off-line, at-line, on-line and in-line applications [24].

3. Results and discussion

The powder x-ray diffraction pattern of $La_{1-x}Cu_xMnO_{3+\delta}$ (x≤0.1) samples synthesized at different temperatures (T=500, 600, 700, 800 and 900^0C) is shown in fig. 1. <<X'Pert HighScore Plus>> program can provide evidence of x-ray phase analysis. As a result of this analysis the sample consists of following two phases: $La_{1-x}Cu_xMnO_{3+\delta}$ (x≤0.1) having $R\bar{3}c$ space group with rhombohedral symmetrical structure and $La_2Cu_2O_5$ having C2/c space group with monoclinic symmetrical structure.

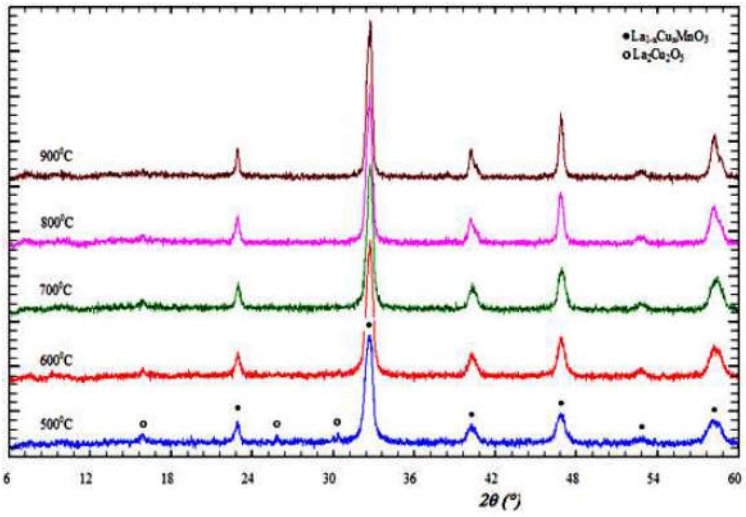

Figure 1. X-ray patterns of $La_{1-x}Cu_xMnO_{3+\delta}$(x≤0.1) synthesized at different temperatures.

Quantity of samples was calculated by FULLPROF program [23] based on Rietveld method (table 1).

Table 1

Sample	$La_{1-x}Cu_xMnO_3$, at. %	$La_2Cu_2O_5$, at. %
500^0C	91.22	8.78
600^0C	96.97	3.03
700^0C	97.19	2.81
800^0C	97.52	2.47
900^0C	97.62	2.37

The quantity of $La_{1-x}Cu_xMnO_{3+\delta}$($x\leq0.1$) increase from 91.22 to 97.62%, but quantity of $La_2Cu_2O_5$ compound decrease from 8.78 to 2.37% with rising of calcination temperature from 500^0C to 900^0C. Particle size and cumulative distribution values of samples are listed in table 2.

Table 2

sample→	1#	2#	3#	4#	5#
x_0,nm ↓	Q_3/%	Q_3/%	Q_3/%	Q_3/%	Q_3/%
55.98	0.01				
60.19	0.01	0.01			
64.72	0.01	0.01			
69.59	0.01	0.01			
74.82	0.01	0.01			
80.45	0.01	0.01			
86.50	0.02	0.01			
93.00	0.02	0.02			
100.00	0.02	0.02			
107.52	0.03	0.02			
115.61	0.03	0.02			
124.30	0.04	0.03			
133.65	0.04	0.03			
143.71	0.05	0.04			
154.52	0.05	0.04			
166.14	0.06	0.05			
178.64	0.06	0.05			
192.07	0.06	0.06			
206.52	0.31	0.06			
222.05	2.24	0.06			
238.76	9.27	0.12			
256.71	25.28	1.16			
276.02	49.37	6.02			
296.78	73.71	19.08	0.62		0.01
319.11	90.22	41.67	4.61	0.47	0.30
343.11	97.64	67.42	16.94	3.72	1.69
368.92	99.72	86.88	39.91	14.10	5.97
396.67	100.00	96.52	67.00	34.60	15.55
426.50		100.00	87.36	60.88	31.63
458.58			96.99	82.97	52.15
493.08			100.00	95.08	72.10
530.16				99.25	86.90
570.04				100.00	95.22
612.92					98.72
659.02					99.78
708.59					99.99
761.89					100.00

Note: x_0-particle diameter, Q_3/%-quantity of volume percent

Particle size and cumulative distribution of nanosized $La_{1-x}Cu_xMnO_{3+\delta}$ ($x\leq0.1$) synthesized at different temperatures are depicted in fig. 2.

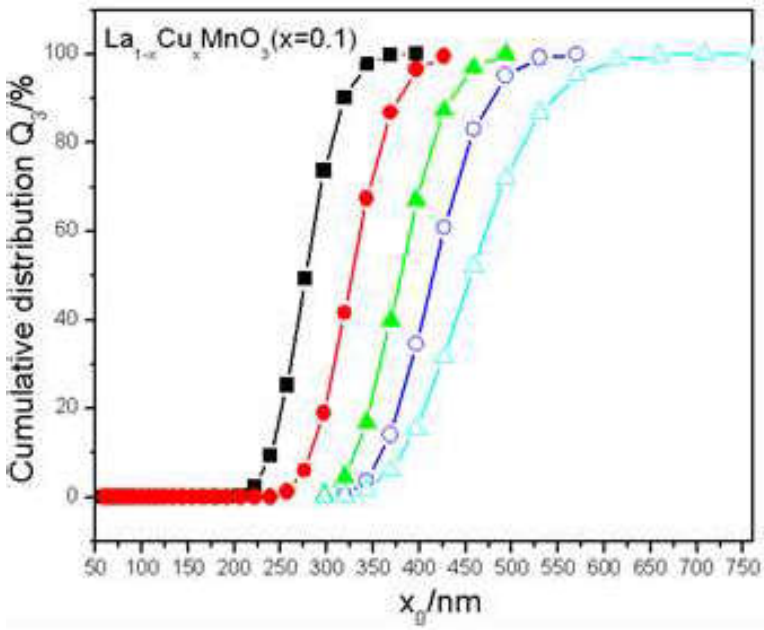

Figure 2. Particle size and cumulative distribution of $La_{1-x}Cu_xMnO_{3+\delta}$ ($x \leq 0.1$) synthesized at different temperatures.

Density distribution of samples measured by NANOPHOX (PCCS) is shown in table 3.

Table 3

sample→	**1#**	**2#**	**3#**	**4#**	**5#**
x_0, nm↓	**$q_3$lg**	**$q_3$lg**	**$q_3$lg**	**$q_3$lg**	**$q_3$lg**
199.16	0.08				
214.15	0.61				
230.25	2.23	0.02			
247.57	5.08	0.33			
266.19	7.65	1.54			
286.22	7.73	4.15	0.20		
307.74	5.24	7.17	1.27	0.15	
330.89	2.35	8.18	3.91	1.03	0.44
355.78	0.66	6.18	7.29	3.30	1.36
382.54	0.09	3.06	8.60	6.51	3.04
411.31		0.95	6.46	8.34	5.11
442.25		0.15	3.06	7.01	6.51
475.52			0.86	3.85	6.34
511.28			0.10	1.32	4.70
549.74				0.24	2.64
591.09					1.11
635.55					0.34
683.35					0.07

Note: x_m-particle diameter, $q_3$lg-density of particle

Dependence of particle size on density distribution is deplicted in Fig. 3.

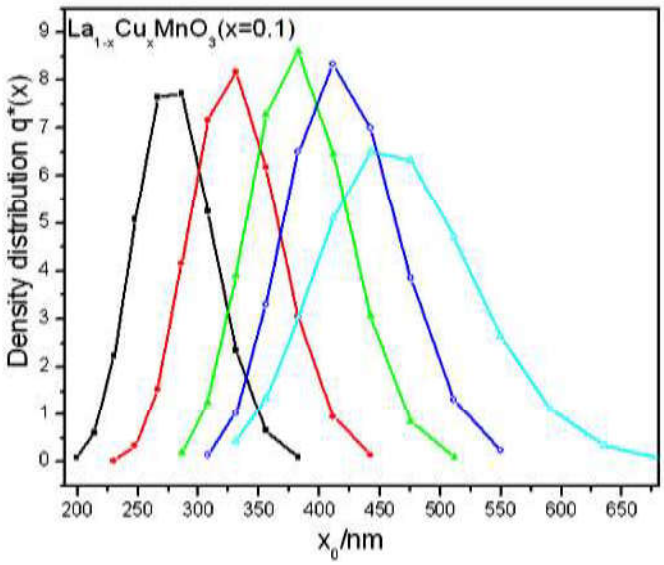

Figure 3. Particle size and density distributions of $La_{1-x}Cu_xMnO_3$ ($x \leq 0.1$) synthesized at different temperatures.

As can be seen, particle mean diameter increases from (276±4) to (455±5)nm, particle specific surface area (Sv) decreases from 21.84 to 13.29m^2/sm^3, particle size distribution equals to 55-761 nm and particle surface and volume mean diameter (SMD,VMD) increases from 247 to 459 nm. Particle mean diameter, particle size distribution, sauter mean diameter (SMD), volume mean diameter (VMD) and specific surface area (Sv) and particle density were measured (table 4).

Table 4

Sample	Particle mean diameter, x_{50}, nm	Particle size distribution, nm	Specific Surface Area, S_V, m^2/cm^3	SMD, nm	VMD, nm	Particle density, $q_3$lg
500^{0}C	276 ± 4	55÷396	21.84	274	278	7.73
600^{0}C	326 ± 3	60÷458	18.49	324	328	8.18
700^{0}C	379 ± 4	296÷530	15.91	377	381	8.60
800^{0}C	414 ± 5	319÷570	14.57	411	416	8.34
900^{0}C	455 ± 5	296÷761	13.29	451	459	6.51

It can be noted that, particle mean diameter and its size distribution were increased with rising of calcinations temperature. On the other hand, there is a decrease of Sv and increase of SMD, VMD. As can be noticed (fig. 2.), particles distribution is Gaussian with density from 0.02 to 8.60 ($q_3$lg) in the range of 199÷307nm. In addition, particle density enhanced up to 700^{0}C, but, decreased at higher temperatures.

4. Conclusions

The aim of this work was to synthesize nanosized $La_{1-x}Cu_xMnO_{3+\delta}$ ($x \leq 0.1$) at different temperatures by using amorphous heteronuclear complexing method. XRD analysis and PCCS measurement were carried out. As a result, it can be concluded that

1. Nanosized $La_{1-x}Cu_xMnO_{3+\delta}$ ($x \leq 0.1$) consists of two phases; $La_{1-x}Cu_xMnO_{3+\delta}$ ($x \leq 0.1$) having $R\bar{3}c$ space group with rhombohedral symmetrical structure and $La_2Cu_2O_5$ having C2/c space group with monoclinic symmetrical structure. It was found that the quantity of $La_{1-x}Cu_xMnO_3$ raise from 91.22 to 97.62%, while quantity of $La_2Cu_2O_5$ compound decrease from 8.78 to 2.37% with increasing of calcination temperature from 500°C to 900°C.
2. Particle mean diameter and its size distribution, SMD as well as VMD were increased, whereas S_V decreased with rising of calcinations temperature.
3. Density distribution is Gaussian. Moreover particle density enhanced at 500-700^{0}C, but, decreased at 700-900^{0}C.

Acknowledgement

The authors are grateful to the Science and Technology Foundation of Mongolia for providing the financial support covering the research work "Investigation of natural and technological nanoparticles by The Photon Cross Correlation Spectroscopy (NANOPHOX)".

References

[1] D.B. Meadowcroft, Low-cost Oxygen Electrode Material, *Nature* 226: 847-848, 1970.
[2] R.J.H. Voorhoeve, J.P. Remeika, P.E. Freeland et al., Rare-Earth Oxides of Manganese and Cobalt Rival Platinum for the Treatment of Carbon Monoxide in Auto Exhaust, *Science* 177: 353-354, 1972.
[3] T. Shimizu, Partial Oxidation of Hydrocarbons and Oxygenated Compounds on Perovskite Oxides, *Catal.Rev.Sc.Eng*. 34: 355-371, 1992.
[4] J.E.H. Sansom, H.A. Rudge-Pickard, G. Smith et al., Perovskite related cuprate phases as potential cathode materials for solid oxide fuel cells, *Solid State Ionics* 175: 99-102, 2004.
[5] I.A. Raj, F. Tietz, A. Gupta, et al., High-temperature superconductor materials for contact layers in solid oxide fuel cells: II. Chemical properties at operating temperatures, *Acta Mater.* 49: 1987-1992, 2001.
[6] J.L. Routbort, K.C. Goretta, R.E. Cook et al., Deformation of perovskite electronic ceramics - a review, *Solid State Ionics* 129: 53-62, 2000.
[7] N. Yamazoe, Y. Teraoka, Oxidation catalysis of perovskites - relationships to bulk structure and composition (valency, defect, etc.), *Catal. Today* 8: 175-199, 1990.
[8] H. Arai, T. Yamada, K. Eguchi et al., Catalytic combustion of methane over various perovskite-type oxides, *Appl. Catal*. 26: 265-276, 1986.
[9] H.M. Zhang, Y.Shimizu, Y. Teraoka et al., Oxygen sorption and catalytic properties of $La_{1-x}Sr_xCo_{1-y}Fe_yO_3$ Perovskite-type oxides, *J. Catal*. 121: 432-440, 1990.
[10] Y.Y. Yao, The oxidation of hydrocarbons and CO over metal oxides: IV. Perovskite-type oxides, *J. Catal*. 36: 266-275, 1975.
[11] T. Nitadori, S. Kurihara, M. Misono, Catalytic properties of $La_{1-x}A'_xMnO_3$ (A′ = Sr, Ce, Hf), *J. Catal.* 98: 221-228, 1986.
[12] T. Nitadori, M. Misono, Catalytic properties of $La_{1-x}A'_xFeO_3$ (A′ = Sr,Ce) and $La_{1-x}Ce_xCoO_3$, *J. Catal*. 93: 459-466, 1985.
[13] K.S. Chan, J. Ma, S. Jaenicke et al., Catalytic carbon monoxide oxidation over strontium, cerium and copper-substituted lanthanum manganates and cobaltates, *Appl. Catal*. *A*. 107: 201-227, 1994.
[14] M. Alifanti, R. Auer, J. Kirchnerova et al., Activity in methane combustion and sensitivity to sulfur poisoning of $La_{1-x}Ce_xMn_{1-y}Co_yO_3$ perovskite oxides, *Appl. Catal*. *B*. 41: 71-81, 2003.
[15] Davide Ferri and Lucio Forni. Methane combustion on some perovskite-like mixed oxides, *Appl. Catal*. *B*. 16: 119-126, 1998.
[16] R.J.H. Voorhoeve, J.P. Remeika, L.E. Trimble, Defect chemistry and catalysis in oxidation and reduction over perovskite-type oxides, *Annals of the New York Academy Sciences* 272: 3-21, 1976.
[17] Y. Zhang-Steenwinkel, J. Beckers, A. Bliek, Surface properties and catalytic performance in CO oxidation of cerium substituted lanthanum–manganese oxides, *Appl. Catal*. A 235: 79-92, 2002.
[18] H. Imai, K. Takami, M. Naito, Preparation of CoLaO3 catalyst fine particles by mist decomposition method II effect of additives for the increase of surface area, *Mat.Res.Bull*. 19: 1293-1300, 1984.
[19] J. Kirchnerova, D. Klvana, J. Vaillancourt, et al., Evaluation of some cobalt and nickel based perovskites prepared by freeze-drying as combustion catalysts, *Catal. Lett*. 21: 77-87, 1993.
[20] M.S.G. Bayathoun, F.R. Sale, Production of strontium-substituted lanthanum manganite perovskite powder by the amorphous citrate process, *J.Mat.Sci*. 17: 2757-2769, 1982.
[21] R.Ganguly, I.K.Gopalakrishnan and J.V. Yakhmi, Does the LaMnO3 phase accept Ce-doping?, *J.Phys.: Condens. Matter* 12: L719-722, 2000.
[22] *X'Pert High Score Plus*. Version 2.0a, PANalytical B, 2003.
[23] *FULLPROF, Rietveld, Profile Matching and Integrated Intensities Refinement of X-ray and /or Neutron Data (powder and /or single-crystal).* Version 3.5d, Laboratories Leon Brillouin (CEA-CNRS), 1998.
[24] *Nanophox Operating Instructions*., Sympatec GmbH, System-Partikel-Technik, Deutschland, 2008.